AD-A138 487 DETERMINATION OF THE EFFECT OF COMPOSITION STRUCTURE AND ELECTROCHEMICAL.. (U) ELECTROCEEMICAL TECHNOLOGY CORP SEATTLE WA T R BECK ET AL. DEC 83 ETC-81-50 1/2

UNCLASSIFIED N00014-82-C-0052 F/G 11/3 NL

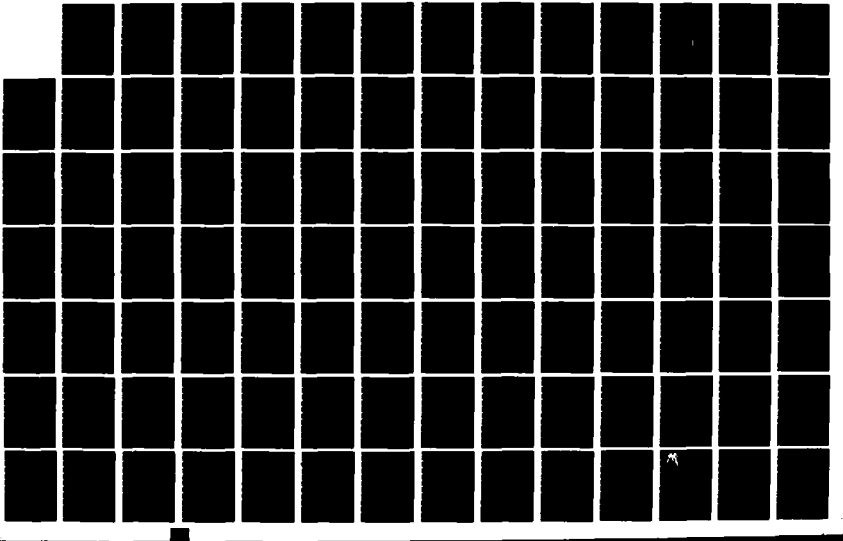

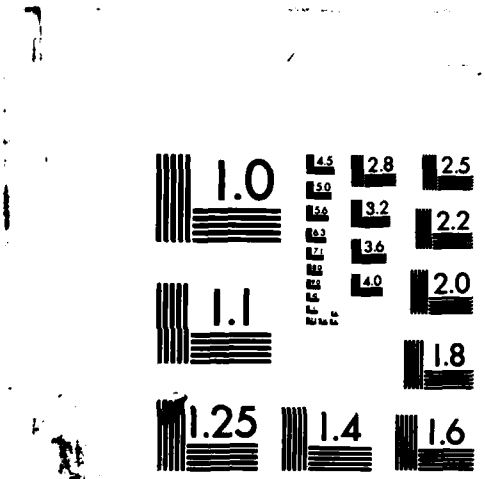

SECURITY CLASSIFICATION OF THIS PAGE (When Data Entered)

(12)

REPORT DOCUMENTATION PAGE

READ INSTRUCTIONS BEFORE COMPLETING FORM

1. REPORT NUMBER	2. GOVT ACCESSION NO.	3. RECIPIENT'S CATALOG NUMBER

4. TITLE (and Subtitle)
Determination of the Effect of Composition, Structure, and Electrochemical Mass Transport Properties on Adhesion and Corrosion Inhibition of Paint Films

5. TYPE OF REPORT & PERIOD COVERED
Final Report
1 Nov. 1981 - 31 Dec. 1983

6. PERFORMING ORG. REPORT NUMBER
ETC 81-50

7. AUTHOR(s)
Theodore R. Beck, Principal Investigator
Robert T. Ruggeri

8. CONTRACT OR GRANT NUMBER(s)
N00014-82-C-0052

9. PERFORMING ORGANIZATION NAME AND ADDRESS
Electrochemical Technology Corp.
3935 Leary Way N.W.
Seattle, WA 98107

10. PROGRAM ELEMENT, PROJECT, TASK AREA & WORK UNIT NUMBERS

11. CONTROLLING OFFICE NAME AND ADDRESS
Office of Naval Research
Department of the Navy
800 North Quincy St., Arlington, VA 22217

12. REPORT DATE
December 1983

13. NUMBER OF PAGES
105

14. MONITORING AGENCY NAME & ADDRESS(if different from Controlling Office)

15. SECURITY CLASS. (of this report)
UNCLASSIFIED

15a. DECLASSIFICATION/DOWNGRADING SCHEDULE

16. DISTRIBUTION STATEMENT (of this Report)

Reproduction in whole or in part is permitted for any purpose of the United States Government.

17. DISTRIBUTION STATEMENT (of the abstract entered in Block 20, if different from Report)

18. SUPPLEMENTARY NOTES

None

19. KEY WORDS (Continue on reverse side if necessary and identify by block number)

Corrosion, diffusion, electrical conductivity, filiform corrosion, mass transport, mathematical model, paint, sodium chloride, transference, water

20. ABSTRACT (Continue on reverse side if necessary and identify by block number)

The transport of sodium and chloride ions and water through six unpigmented paints has been investigated experimentally using a radiotracer method. A previously proposed mass transport model of paints was inadequate to explain the experimental observations. A new mass transport model is proposed and tested. Qualitative agreement between the new model and the experiments is achieved when the effective dielectric constant of the paint is increased above the observed value. A gravametric microbalance technique was used to determine the sorption of water by four types of paint. Both steady state and

DD FORM 1 JAN 73 1473

UNCLASSIFIED
SECURITY CLASSIFICATION OF THIS PAGE (When Data Entered)

20.

transient conditions have been investigated. These experiments show that both the solubility and diffusivity depend on the specimen thickness. The results are interpreted in terms of a two-phase paint layer which preferentially absorbs water near the paint-metal interface.

Contract No. N00014-82-C-0052

DETERMINATION OF THE EFFECT OF COMPOSITION, STRUCTURE, AND ELECTROCHEMICAL MASS TRANSPORT PROPERTIES ON ADHESION AND CORROSION INHIBITION OF PAINT FILMS

FINAL REPORT

Prepared for:

Office of Naval Research
Department of the Navy
800 North Quincy Street
Arlington, VA 22217

By: Theodore R. Beck, Principal Investigator
Robert T. Ruggeri

Electrochemical Technology Corp.
3935 Leary Way N.W.
Seattle, WA 98107

December 1983

TABLE OF CONTENTS

Determination of the Effect of Composition, Structure, and Electrochemical Mass Transport Properties on Adhesion and Corrosion Inhibition of Paint Films

SUMMARY

The primary objective of this work was to develop a better understanding of the fundamentals of ionic and molecular transport in paint films. A second objective was to quantitatively model the mass transport in paints and to use this model to gain insight into the initiation of corrosion of painted metals.

This work represents a continuation of an investigation initiated under a previous contract with the Navy. Table 1 is a summary of the experimental work completed under both contracts. Hittorf experiments were conducted to determine ion and water permeability coefficients, transference numbers, and electrical conductivity. Hittorf experiments were attempted with all eight of the paints under study, but successful experiments could not be conducted with four of the paints. The epoxies were brittle and cracked when they were clamped into the Hittorf apparatus. The vinyl resin which failed (VR 2) was difficult to form into a uniform film unattached to any substrate, and the specimens which were tested cracked a short time after being mounted in the Hittorf apparatus. No experiments were conducted with the epoxies in the quartz oscillator apparatus because the results could not be compared with those obtained from Hittorf experiments, and because no meaningful model calculations could be performed without Hittorf data. High pressure reverse osmosis experiments were not required for the mathematical

Table 1

Matrix of Paints and Properties, Measurements and Operations

Properties, Measurements or Operations	Paint System							
	O PUR	N PUR	VR 2	VR 3	VR 4	E Epoxy	A Epoxy	K Epoxy
Formula and molecular weights	A*	✓	✓	✓	✓	A*	✓	✓
IR and UV spectra	✓	✓	✓	✓	✓	✓	✓	✓
Dynamic mechanical properties	✓	✓	✓	✓	✓	✓	✓	✓
Transference No., Na^+,Cl^-	✓	✓	B*	✓	✓	B*	B*	B*
Conductivity	✓	✓	B*	✓	✓	B*	B*	B*
Ion Solubility	✓	✓	✓	✓	✓	C*	C*	C*
Diffusivity of water								
ASTM vs. temp.	✓	✓	✓	✓	✓	B*	✓	✓
Quartz oscillator	✓	✓	✓	✓	✓			
Permeability of Na^+,Cl^-	✓	✓	B*	✓	✓	B*	B*	B*
Permeability of water	✓	✓	B*	✓	✓	B*	B*	B*
High pressure reverse osmosis permeability	✓	✓	✓	✓	✓			
Adhesion force	✓	✓	✓	✓	✓	✓		✓
Computer model cal.								
IE model	✓							
IA model	✓							

*A Proprietary formula
B Physical properties prevented successful completion of experiments
C No significant radiotracer counts

model and were therefore not conducted under this contract. Model calculations were conducted for the O PUR system. The ion exchange (IE) model proved to be inadequate to describe the experimental results, and for this reason other systems were not tested. A second, ion association (IA) model was formulated which simulated the behavior of O PUR only qualitatively. IA model calculations were not conducted for the other paints because fewer data were available for these paints, and the model was not quantitative.

An attempt was made to determine if hydrogen or hydroxyl ions had high transference numbers in paints. Prior to and following each Hittorf experiment the pH of the aqueous solutions was determined. The pH fluctuated erratically. The cause could not be determined, and no conclusions were drawn.

Three tasks were not performed because the transport mechanism in paint was more complicated than originally expected, and no quantitative transport model was found. These tasks include: correlating the transport behavior with paint composition and chemical structure, measuring paint adhesion to determine the time required to initiate corrosion on steel, and correlating the service performance of the paints with the results of the transport model.

The results of this work are not what was originally envisioned, but significant contributions have been made toward achievement of the primary objective. Experimental results have demonstrated that sodium and chloride ions do not carry all the current through some paints immersed in NaCl solution. This fact is contrary to an assumption almost universally accepted by paint researchers, and may have a significant effect on the corrosion retarding ability of some paints. New quantitative data have been obtained on the permeability of these paints to ions and water. The hypothesis that ion association occurs in paints has been presented. Although ion association is known to occur in liquids with low dielectric constants, to the author's knowledge, it has not been previously proposed as part of the mass transport mechanism for paints.

INTRODUCTION

Corrosion of metals is a costly and continuing problem. One of the most common methods of reducing the rate of corrosion is to paint metal surfaces. Although paints have been employed for this purpose for many years, knowledge of how paints reduce corrosion is incomplete. This work was begun under a contract from the Naval Ocean Research and Development Activity (1, 2, 3) and has continued under the present contract. The purpose of this work was to characterize the primary physical and mass transport properties of paints and to attempt to relate these properties to the initiation of corrosion through mass transport models of the paints.

In general the understanding of the corrosion process for bare metals is advanced beyond that for painted metals. This situation is largely due to our inability to determine the electrolyte concentrations at the corrosion site, the paint-metal interface. The transport properties of paints are by their nature different from aqueous electrolytes; therefore, the electrolyte concentrations at the paint-metal interface will depend on the transport properties of the paint and the transport properties and composition of the external electrolyte. If it is assumed that the paint functions only as a barrier to mass transport, the corrosion of painted metal will be controlled by the local conditions at the paint-metal interface, and if conditions at the metal surface are known, the corrosion process will proceed as it would for bare metal in the same environment. It is the intent of this work to determine and model the transport properties of paint in order to allow the local conditions at the paint-metal interface to be calculated.

It is well known that polymers exhibit a number of different types of transport behavior (4). These behaviors may be broadly categorized as diffusion in glassy solids, heterogeneous media, and ion-exchange polymers. Previous studies of paints have suggested that many paints behave as ion-exchange materials (5). Thus, the first model developed in this laboratory considered paint as a strong ion-exchange polymer with small ion-exchange capacity (6). The phenomenological transport equations discussed by Newman (7) were used as the foundation of this early paint model because conventional ion-exchange membranes are often described with these equations.

An experimental program was conducted in conjunction with development of the first mathematical model. The experiments showed that the IE model was inadequate, and the phenomenological transport equations were unnecessary for the paints which were examined. This discovery led to the development of the second mathematical model of paint which incorporates the concepts of ion association and employs dilute solution transport equations.

APPARATUS AND PROCEDURE

Paints

Five different paint formulations have been extensively studied in this work. The paints consisted of two similar polyurethane formulations designated O PUR and N PUR and three vinyl resin formulations: XYHL designated VR 2, VAGH designated VR 3, and VYHH designated VR 4. More detailed information on the structure and composition of the paints is provided in Appendix B.

Industrial grade chemicals were used to make up the vinyl resins. The two polyurethanes were obtained from commercial sources and were mixed according to the manufacturers specifications. Pigments were not used in this work. Paint solvents were prepared from ACS reagent grade chemicals.

Hittorf Experiments

Both membrane-potential and Hittorf experiments were conducted in the same apparatus. Figure 1 illustrates the experimental cell which was made of Plexiglas. The cell was composed of two cylindrical compartments separated by a paint membrane. The two compartments were aligned vertically. Both compartments were equipped with sampling ports and overflow tubes. The sampling ports were sealed with rubber septums, but the overflow tubes were open to the air. The overflow tubes were made of capillary tubing with one end drawn down to a small diameter. This construction reduced water evaporation to a negligible level. The overflow tubes from both the top and bottom compartments were bent above the cell so that they were in the same horizontal plane. In this way the hydrostatic pressure difference across the membrane was minimized.

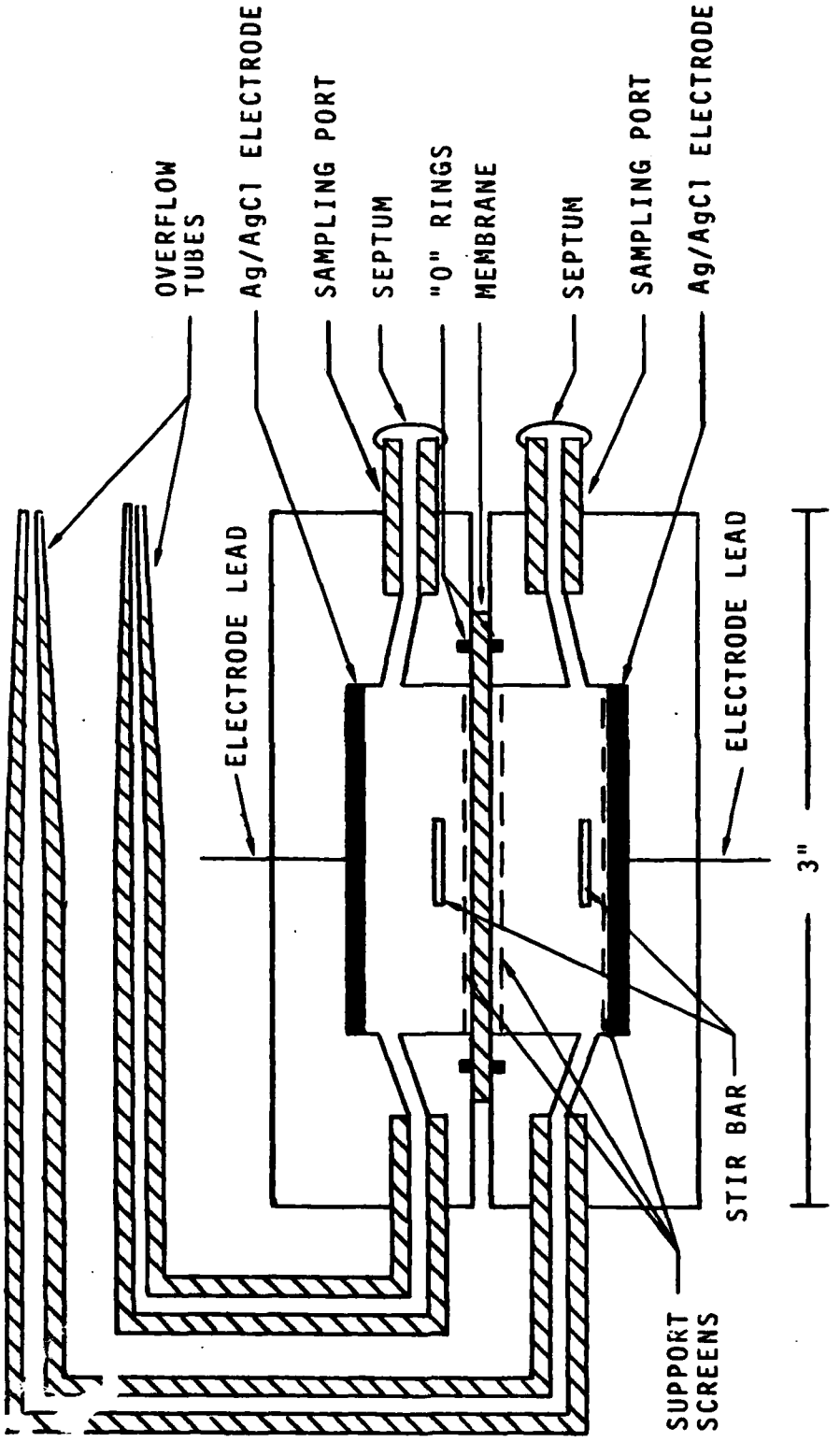

Fig. 1. Hittorf Cell

Internally, each cell compartment was identical, but the external connections (sampling ports, overflow tubes, etc.) were in different positions in each half-cell. The paint membrane was clamped between the two half-cells which were held together by four bolts. Viton O-ring gaskets were used to prevent the chambers from leaking between the paint and the Plexiglas.

Each compartment was equipped with a silver-silver chloride electrode. The electrodes were glued to the Plexiglas with epoxy. The electrode diameter was the same as the "active" diameter of the membrane, and both electrodes were parallel to, and equidistant from, the membrane.

A small Teflon-coated magnetic stir bar was used to stir the solution in each compartment. The stir bar in the bottom compartment was held above the electrode surface by a circular disc of plastic window screen. Similar screens were clamped on each side of the paint membrane as physical supports. The stir bar in the top compartment rested directly on the upper support screen. Stirring speeds of approximately 100 rpm were achieved with a magnetic stir plate.

The assembled Hittorf cell was placed in a Faraday cage during experiments. A battery was used to control the cell potential between the two electrodes. The applied voltage and electrode current were measured with Keithley model 610 electrometers. Figure 2 is a schematic diagram of the electrical connections. The electrometers contain retransmitting amplifiers with low output impedance. The output of these amplifiers was recorded on an Esterline Angus model E1124E strip chart recorder. The output of the electrometer recording the current was integrated with an Acromag model 1752-K1-1 integrator. The total charge passed in the course of an experiment was obtained from the integrator. This instrumentation provided a permanent record of the voltage, current, and total charge for each experiment.

The experimental temperature was controlled with an air thermostat. A modified on-off household thermostat was used. Temperatures adjacent to the cell were measured with National Semiconductor LX5600 temperature transducers. The transducers were purchased in TO-5 packages, and were equipped with radial-finned clip-on heat sinks. The cell temperatures were also recorded on the strip chart. A peak-to-peak temperature excursion of 1°C was observed with this apparatus.

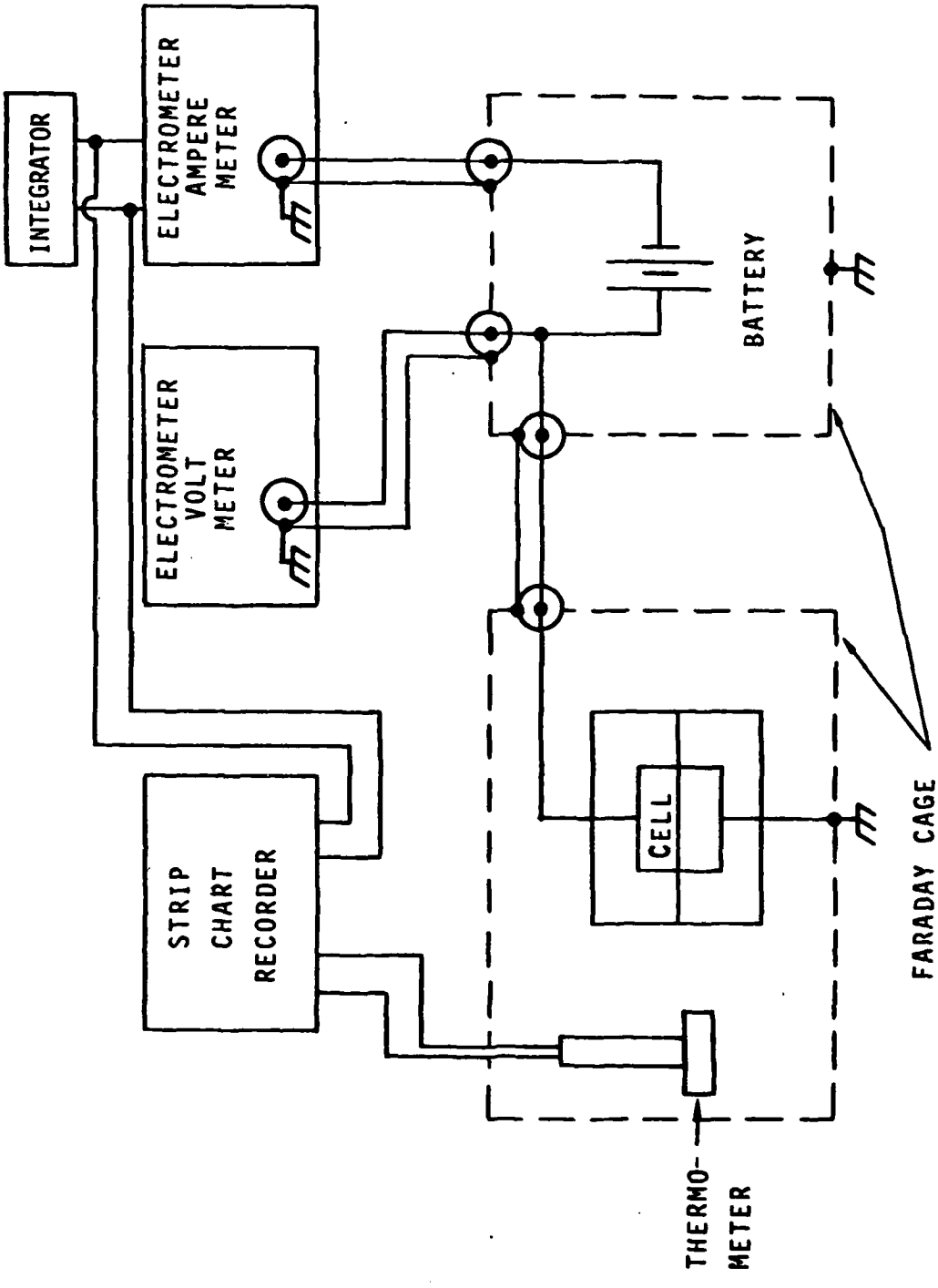

Fig. 2. Electrical schematic and instrumentation for a Hittorf experiment.

All salts and solvents were ACS reagent grade, and the water was distilled. The paint formulations are included in Appendix B. Radioactive hydrogen (H^3), sodium (Na^{22}), and chloride (Cl^{36}) were purchased in carrier-free form from commercial sources. Radiotracer standards, traceable to the National Bureau of Standards, were purchased and used to make reference solutions. The radiotracer content of samples was measured with a Packard model 2022 scintillation counter at the University of Washington.

In order to perform a Hittorf experiment, paint membranes unattached to any substrate were first prepared. Paints were first mixed according to the supplier's intstructions. In the case of the polyurethane which was investigated most (O PUR, System VIII), equal parts of catalyst and base were mixed. The paint was then spray applied to sheets of decal paper and allowed to dry. Drying took place in the ambient laboratory air at about 60% relative humidity and 23°C. The paint was protected from dust in a fume hood for about 24 hours. The coated pieces of decal paper were then placed in paper envelopes and stored in a wooden cabinet until needed. Storage times varied from two weeks to two years.

Immediately prior to use, specimens of paint were cut from the large sheets of coated decal paper. The decal paper was soaked in water for a few minutes until the paint could be easily removed. The free paint film was then washed in tap water till no mucilage could be detected by touch. Then the paint was rinsed in distilled water for a few seconds and dried with a paper towel. The dry paint film was allowed to stand in laboratory air for about 15 minutes before the thickness was measured with a micrometer. Twelve to 15 thickness measurements were made in the test area of the sample. The average coating thickness and standard deviations were then calculated. Free films with nonuniform thickness or high standard deviations were rejected. The membrane was next checked optically for defects: holes, dirt or dust particles, etc. Membranes which did not appear to be smooth and free of defects were rejected. The final pre-experiment check was a conductivity measurement. The membrane was mounted in a Hittorf cell and its dc conductivity was determined. If the conductivity differed more than a factor of about three from the average conductivity of similar membranes it was rejected. After a specimen passed all the pre-experiment tests it was ready for mounting in a Hittorf cell.

Prior to an experiment, the Hittorf-cell electrodes were checked. Solutions of differing salt concentration were placed in each half-cell, and the electrode potentials were measured relative to a standard reference electrode. If the "Nernst slope" for the Hittorf electrode exceeded 55 mV/decade, the electrode was considered acceptable. If the electrode failed this test, the silver chloride layer was removed and the silver was abraded, cleaned, and reanodized. Also, prior to the experiment the Plexiglas was inspected for scratches. If scratches were found, they were removed by polishing.

After the cell had been polished and the electrodes had passed inspection, both halves of the cell were rinsed in distilled water and then in methanol. The cell was then dried by blowing air through the injection ports and the overflow tubes. When the cell was completely dry, it was ready for assembly.

The cell was assembled in steps proceeding vertically from the bottom to the top. A screen was first placed in the bottom compartment over the silver-silver chloride electrode. A magnetic stir bar was then placed on the screen. Next, a second screen was placed over the mouth of the bottom compartment. The diameter of the second screen was greater than the compartment diameter. This screen supported the membrane. Next, the O-ring was coated with a thin layer of silicone stopcock grease and placed in its groove around the screen. Then the paint film was placed over the O-ring and the support screen. In standard procedure the air-side of the paint film was placed down; the decal-paper side was up. Next, a second support screen was placed on top of the paint, and another stir bar was placed on this second screen. Finally, the top half of the cell was placed on, and the entire assembly was bolted together. After the cell was assembled, a visual inspection was made. The inspection included checking the O-ring seals, the support screens, and the stir bars. If the inspection reveals no defects, the assembly was completed by placing rubber septums over the open ends of the injection ports.

Prior to filling the cell it was weighed. The assembled cell was then filled with electrolyte using a hypodermic syringe. The volume of electrolyte added to each compartment was measured with the syringe.

The weight of the cell was also measured after each compartment was filled. This procedure provided two independent measures of the fluid volume in each compartment. The volume of fluid in the overflow tube was determined by the position of the liquid meniscus. Another visual inspection was performed after filling the cell. If bubbles with diameters greater than about 3mm (≈10% of the diameter of the compartments) were observed, the filling procedure was repeated. If the bubbles could not be removed, the compartments were emptied and the cell reassembled.

Electrolyte solutions were mixed just prior to assembling the cell. Various sodium chloride concentrations from 0.01 N to 3 N were employed. Radiotracers were added just prior to filling the cell. The solution containing the radiotracers was always placed in the bottom compartment. Solutions in both compartments were of the same salt concentration, but no radiotracers were used in the top compartment. The bottom compartment always contained two radiotracers: tritium (H^3) and either sodium or chloride. In this way the water flux and one of the ion fluxes could be obtained.

After the cell had been filled, 10 µl samples were taken from each compartment. The cell was placed on a stir plate inside a thermostatically controlled glovebox. The cell was then connected to the battery and the electronic monitoring equipment. The cell was always connected to the battery with the polarity such that the radiotracer (Na^{22} or Cl^{36}) was forced across the membrane. Experiments were conducted for various periods of time up to three months. The cell voltage, current, and temperature were recorded. Radiotracer samples (10 µl) were periodically withdrawn with Hamilton micro-syringes through the rubber septums. The top compartment was sampled about every three days. The bottom compartment was sampled at two-week intervals. At the end of the experiment three samples were withdrawn from each compartment.

During the course of an experiment the positions of the menisci in the overflow tubes were periodically recorded. By comparing the relative positions of the two menisci, leaks could be detected. Experiments were terminated when leaks developed. At the conclusion of an experiment, the cell was dismantled and each half cell was leached for two weeks in separate distilled water baths.

The radiotracer samples were analyzed by liquid scintillation counting. The scintillation counter was capable of counting two radioisotopes simultaneously. The different isotopes were distinguished by the different energies of their β emissions. Chloride-36 could not be distinguished from sodium-22 because both radionuclides have similar β-energy spectra. Therefore, tritium and either sodium or chloride were used in each experiment, and sodium and chloride fluxes were determined in separate experiments.

Approximately five standard samples were used to calibrate the scintillation counter during each counting session. The activities of the standards varied, covering a range approximately equal to that expected for the experimental samples. A least-squares matrix inversion method was used to determine counting efficiencies and cross-channel interference coefficients from the calibration data. The accuracy of each calibration matrix was also checked by counting mixtures of known composition. No quenching was observed with the small sample volumes (10 μl) used.

Transference numbers for sodium and chloride were calculated in the following way. First, the activity of the radiotracer (sodium or chloride) in the top compartment was obtained. These data were converted to equivalents of carrier (n_c) per ml by assuming a specific molar activity equal to that in the bottom cell. Then, the data were plotted as n_c versus charge passed (Figure 9). Different least-squares straight lines were then constructed through the data collected at each cell potential. Finally, the transference numbers were set equal to the slopes of the lines. This method was considered appropriate as long as two conditions were met. The radiotracer flux at zero applied voltage was negligible, and the fraction of radiotracer transported across the membrane was small. Both conditions were always satisfied in these experiments.

The diffusivity of water was calculated from measurements of the tritium concentration. It was assumed that tritium only passed through the membrane as water. This assumption cannot be easily verified. Other assumptions were the same as for sodium and chloride transport except that the fraction of tritium transported was usually large. In order to account for this fact, a differential mass balance was derived for the top compartment.

The equation was solved to yield the tritium activity in the top compartment as a function of the water diffusivity and time. Experimental results were then used with the calculated solution, and a diffusivity was obtained for each of n experimental data points. These individual diffusivities were averaged to obtain the tabulated values.

Humidity Chamber

The "humidity chamber" apparatus was designed to subject a paint specimen to an isothermal step-change in relative humidity. A small quantity of paint was placed on one side of a gold coated quartz crystal which controlled the frequency of an electronic oscillator. The crystal and the oscillator were suspended inside a metal chamber mounted inside a Plexiglas box. The relative humidity in the chamber was different than that in the Plexiglas box. The crystal was first allowed to equilibriate with the atmosphere inside the inner (metal) chamber. Then the inner chamber was opened and the crystal was exposed to the atmosphere in the Plexiglas box. A good step-change in relative humidity was reproducibly produced using this technique.

The humidity chamber apparatus is illustrated in Fig. 3. The outer chamber was constructed of 6.35 mm thick Plexiglas and was insulated with 2 cm thick styrofoam. The volume of the outer chamber was 15 liters. The temperature in the box was controlled with a VWR #14370-030 proportional controller. The main constant-temperature bath was located outside the box and water was circulated from the bath through a finned-tube heat exchanger inside the box. The air inside the box was circulated with a fan. Three copper-constantan thermocouples were used to measure the temperature at different locations in the box. The maximum temperature difference between the different locations was 0.1°C, and a long-term temperature fluctuation of 0.5°C was observed.

The inner chamber was composed of two parts: a movable "cup," and a stationary "lid." The lid was attached to the Plexiglas box with a metal bracket. The cup could be raised and sealed against the lid to form the inner chamber, or lowered to open the chamber. The cup was aligned with the lid by a Plexiglas tube attached to the box. Both the alignment tube and the bracket supporting the lid were perforated with holes

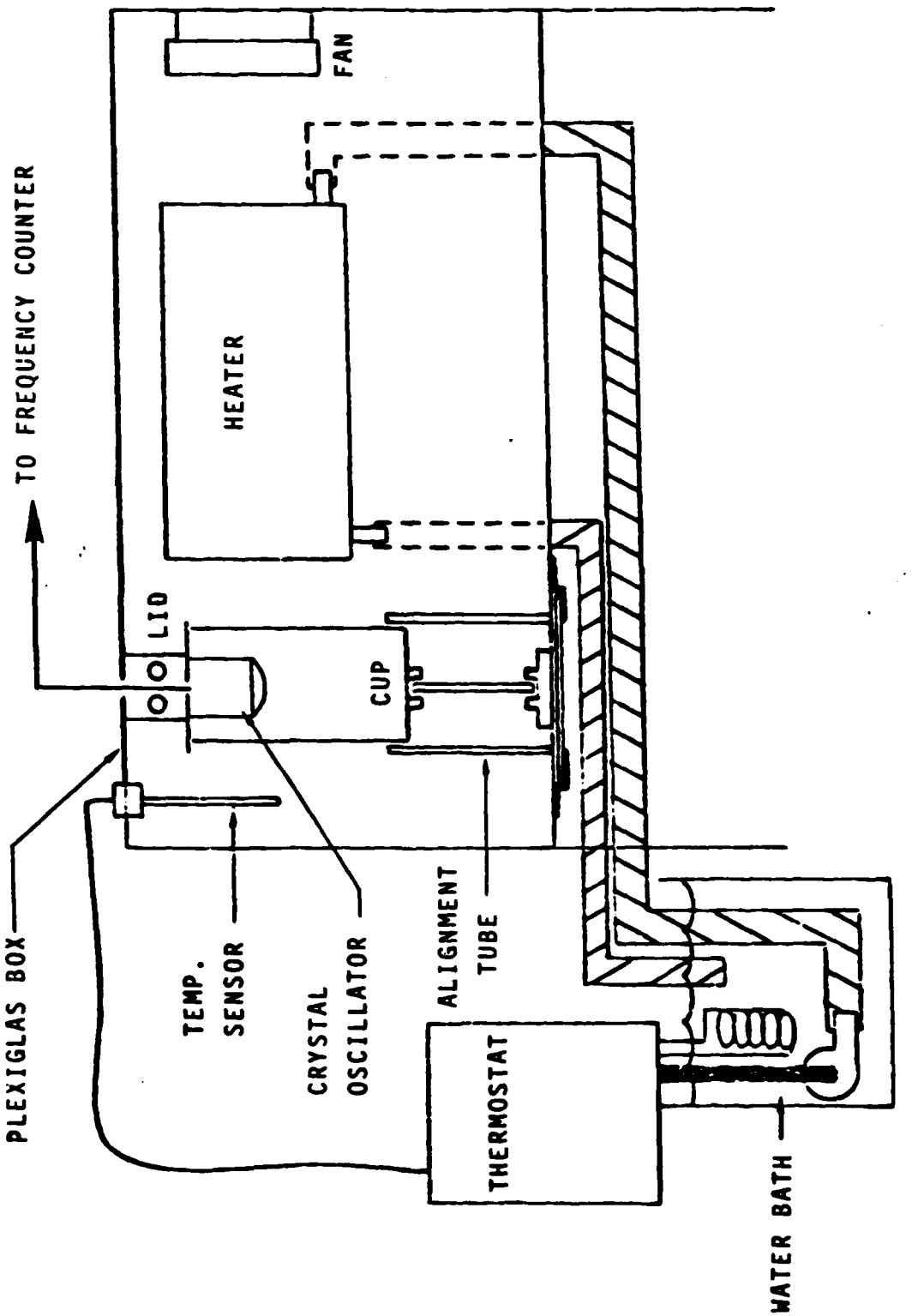

Fig. 3. Humidity chamber and crystal oscillator.

(approx. 10 mm diam.) to allow air to circulate completely around the inner chamber. In the raised position, the cup was supported by a Plexiglas column resting on a closed trapdoor. When the door was opened the entire cup-column assembly could be removed from the box. The cup and lid were both constructed of 1 mm thick sheet metal. The cup was 92 mm high and 55 mm in diameter, with a volume of 219 ml.

The oscillator and crystal holder comprised a single unit which was mounted on the inside surface of the lid. The oscillator was a "Digital Sensor Head" #900010 Sloan Technology Corp., Santa Barbara, Calif. The oscillator was powered by a 6 V regulated power supply (Acopian model 6E20D). The oscillator frequency was measured with a General Radio model 1191 frequency counter and automatically recorded on paper tape with a Datil model DPP-Q7 thermal printer. Only the "Digital Sensor Head" was inside the Plexiglas box. The circuit diagram of the electrical connections between the power supply, the oscillator, and the frequency counter is shown in Fig. 4. A low-pass filter (Fig. 4) was used between the oscillator and the frequency counter. The filter was not a necessary part of the circuit, but it reduced the effects of stray capacitance.

The crystals for the oscillator were purchased from Sloan Technology Corp. They were AT-cut quartz discs 12.5 mm in diameter and approximately 0.33 mm thick. The nominal frequency was 5.0 MHz. The as-received crystals had been coated on both sides with a thin layer of metal. The metal provided electrical contact with the crystal as it rested in the holder. Crystals with either gold or silver coatings were used. Only part of one surface of the crystal was exposed to air when it was mounted in the holder. The exposed surface was visible through an 8.0 mm diameter hole in the crystal holder.

The first step in the procedure was to record the base frequency (f_q) of the uncoated crystal in "dry" air at 30°C. Calcium sulfate (Drierite) desiccant was used to maintain dry conditions. Several of the crystals were also weighed on a Cahn model gram-1501 electrobalance, with a reproducibility of ±10 μg. The base frequencies (f_q) and base weights (w_q) were measured at least three times for each crystal.

After the base data had been obtained, the crystals were prepared for painting. The crystals were flat only on one face. The other face was

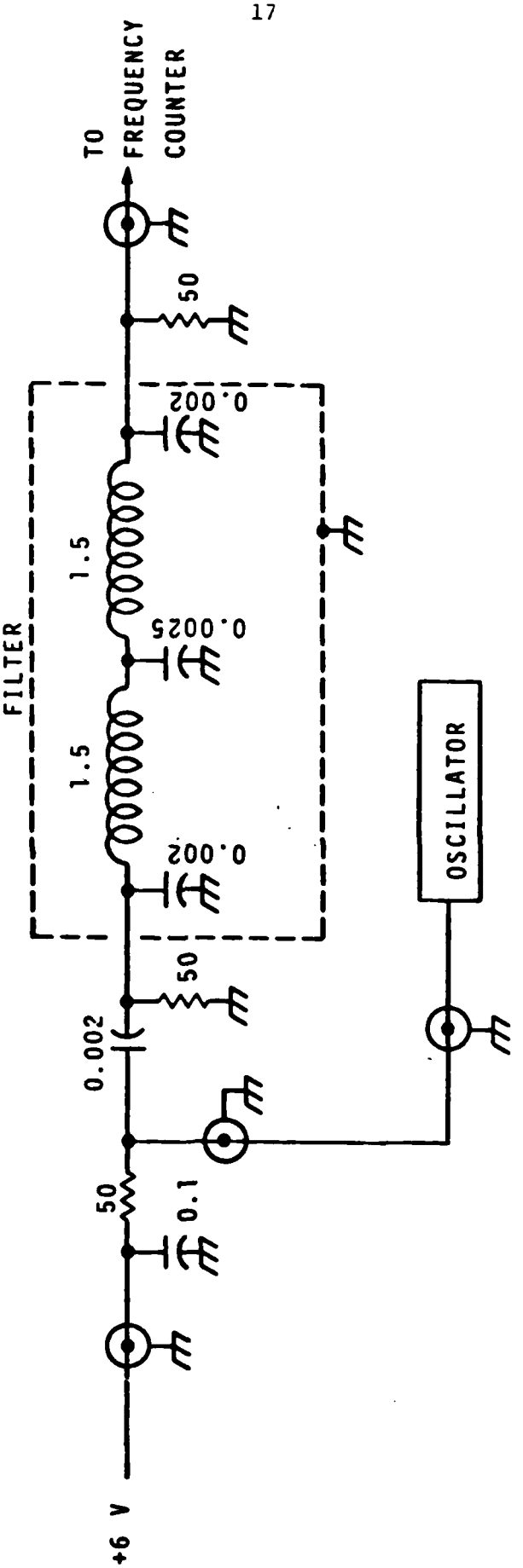

Fig. 4. Crystal oscillator circuit diagram. Resistance values are ohms. Capacitance values are μF. Inductance values are μH.

slightly convex. Lu and Lewis (8) used similar crystals to confirm the acoustic resonator theory (Appendix A). Tests showed that the crystal oscillator would cease to function if too great a mass of paint was applied to the crystal. A larger mass could be applied to the flat side than to the convex side while maintaining oscillation. Masks were used to produce uniform-diameter paint spots which were centered on the flat side of the crystal. The masks were cut from plastic electricians tape with a cork bore. Various spot diameters were tested, but 5.8 mm was standard. The individual spot diameters were determined by averaging at least six measurements of the diameter (±0.3 mm) made with a metal rule. The paint was applied to the crystals with a 1 $\mu\ell$ pipette. Different coating thicknesses were achieved by diluting the paint with an appropriate solvent prior to application. The coatings were allowed to dry for several days at ambient conditions. The average laboratory temperature was 23°C and the average relative humidity about 60%. After the coating had dried the mask was removed by soaking the crystal in an organic solvent. Several solvents have been used but hexane was one of the best. It dissolved the sticky side of the tape and had no apparent effect on the coatings. The crystals were soaked in hexane for ten to fifteen minutes; then the mask was lifted off with a pair of tweezers. The mask was inspected for visible traces of metal. If metal flecks were found the crystal was not used. Crystals were also not used if any trace of the mask remained imbedded in the paint, or if any part of the paint became detached from the crystal.

After the masks had been removed, the crystals were rinsed with hexane and dried in laboratory air for several hours. The frequency (f_d) was then measured after equilibrating the crystals with a dry atmosphere. The crystals were also weighed (w_d) while being desiccated.

At this stage a painted crystal was ready to be used in a diffusion experiment. The crystal was placed in the holder with the paint spot visible through the hole. The holder was then attached to the rest of the oscillator assembly, and oscillation was confirmed with the frequency counter or an oscilloscope. A saturated salt solution was placed inside the cup, and the cup was raised to seal the inner chamber. Desiccant, or a second salt solution, was placed in the outer chamber which was then sealed. Thermocouples

were used to determine the temperatures in both the inner and outer chambers. When all thermocouples and the frequency had attained a steady state the printer was turned on and the frequency counter was adjusted to update the frequency once each second. A stopwatch was started and the cup was dropped at a well-specified time. The frequency (f) was automatically recorded every second for approximately 100 seconds. Thereafter the frequency was recorded every ten seconds. Frequency measurements were continued in this manner until a total elapsed time greater than 300 seconds had passed. Most experiments had reached a "steady state" in 300 seconds, but some were extended up to 2 h total time.

Each crystal was tested at least twice for each step change in relative humidity. The standard procedure was to allow the "closed-cup" system 16 h to reach steady state. The first experiment was then conducted. When this experiment was complete the cup was raised and the system was allowed to stand for about 7 h. A second experiment was then conducted as before. The frequencies obtained from the two experiments were compared at each time interval. If both experiments were in satisfactory agreement, the results of the first run were used to calculate the water diffusivity. If the experiments did not agree the sequence was repeated. The results were analyzed according to the theory of one dimensional diffusion into a plane sheet (9)(Appendix A).

Solubility Experiments

No special apparatus was used in these experiments. Solution and counting apparatus were as described in the section on Hittorf experiments.

A known mass (approximately 0.2 g) of each paint was placed in a 10 mL scintillation-counting vial. Two milliliters of aqueous sodium chloride solution containing a known quantity of radiotracer were added to each vial with a pipette. The vials were sealed and allowed to equilibrate for about 30 days. Each vial was shaken daily and 10 μL samples of the solution were withdrawn weekly for radiotracer analysis. At the end of this first equilibration period the paint was withdrawn, dipped once in each of three 100 mL volumes of distilled water, and placed in two milliliters of a second solution. The second sodium chloride solution was of the same concentration as the first

solution, but it contained no radiotracers. Ten-microliter samples were withdrawn from the second solution at approximately two-day intervals for about 30 days. Liquid scintillation was used to determine the radiotracer content of the fluid as a function of equilibration time. The samples generally reached equilibrium in approximately two weeks. The temperature was recorded daily during both equilibration periods. The solubility of the tracer species (sodium or chlorine) was determined by the formula:

$$C_p = \frac{V_s \, C_{NaCl}}{M_p\left(\frac{A_o}{A_f} - 1\right)} \qquad (1)$$

where V_s = solution volume

C_p = concentration of the tracer species in paint

C_{NaCl} = concentration of sodium chloride in the equilibrating solutions

M_p = mass of paint

A_o = activity of radiotracer in the first solution after equilibration

A_f = activity of radiotracer in the final solution after equilibration

RESULTS AND DISCUSSION

Transference Numbers

The transference numbers obtained in the Hittorf experiments are summarized in Tables 1A-1D. For O PUR membranes immersed in 0.1 N NaCl solution the transference number for sodium (t_+) is 0.41 ± 0.07, and the transference number for chloride (t_-) is 0.31 ± 0.05. The error limits represent one standard deviation from the mean. The striking feature of these results is that the sum of the transference numbers is not one. How significant is the discrepancy? The experiments in 0.1 N NaCl solution were obtained with two specimens of O PUR. These two specimens originally occupied adjacent positions on a single sheet of O PUR paint. One of the specimens was used in the series of experiments 5A through 5F. The other specimen was used for 6A through 6F. A comparison of how the sum of the sodium and chloride transference numbers ($t_+ + t_-$) varied with time was obtained by pairwise matching of the results of the two series of experiments. The transference number obtained in 5A was matched with that obtained in 6A and so on. The average sum $t_+ + t_- = 0.727 \pm 0.100$. A statistical t test

Table 1A

Transference Numbers of Sodium
and Chloride Ions in 0 PUR at 25°C

NaCl Conc. (N)	t_+	t_-	Applied Potential (V)	Specimen	Thickness (μm)	Age in Soln. at End of Exper. (days)
0.009	0.021		9.3	A	38.7	13
0.023		0.268	4.4	B	37.9	
		0.254	9.4	B		
		0.286	19.5	B		
		0.222	13.7	B		63
0.023	0.022		3.0	B	37.9	105
0.023	0.366		6.0	B	37.9	
	0.498		6.1	B		
	0.493		9.3	B		
	0.517		12.5	B		
	0.568		6.1	B		
	0.504		9.2	B		202
0.025	0.021		4.0	C	34.5	
	0.105		9.9	C		
	0.009		19.0	C		51
0.037		0.362	9.5	D	57.6	14
0.100	0.514		9.3	E	80.9	13
		0.261	9.3	E		27
	0.384		13.6	E		47
		0.307	13.4	E		71
	0.437		16.4	E		99
		0.271	16.6	E		120
0.100		0.381	8.8	F	64.1	11
	0.334		8.8	F		26
		0.374	13.4	F		46
	0.360		13.4	F		68
		0.287	16.3	F		96
	0.453		16.2	F		117
0.300		0.317	6.25	G	128.0	
		0.450	12.5	G		
		0.400	9.5	G		
		0.370	6.3	G		70

Table 1A (Con't)

NaCl Conc. (N)	t_+	t_-	Applied Potential (V)	Specimen	Thickness (μm)	Age in Soln. at End of Exper. (days)
0.302	0.277		6.1	H	61.6	
	0.315		9.3	H		
	0.150		9.3	H		
	0.256		23.5	H		61
1.00		0.407	6.2	I	76.5	55
0.128*		0.03	2.9	Q	85.1	
		0.11	4.4	Q		
		0.18	5.8	Q		
		0.16	2.9	Q		64

*Experimental Temperature = 32°C

Table 1B

Transference Numbers of Sodium and Chloride Ions in N PUR at 25°C

NaCl Conc. (N)	t_+	t_-	Applied Potential (V)	Specimen	Thickness (μm)	Age in Soln. at End of Exper. (days)
0.094	0.38		6.0	J	30.5	
	0.36		1.5	J		
	0.16		0.7	J		
	0.36		1.55	J		
	0.86		3.0	J		57
0.111		0.25	3.1	K	31.1	
		0.20	1.55	K		
		0.17	0.7	K		
		0.18	2.9	K		51

Table 1C
Transference Numbers of Sodium
and Chloride Ions in VR 3 at 25°C

NaCl Conc. (N)	t_+	t_-	Applied Potential (V)	Specimen	Thickness (μm)	Age in Soln. at End of Exper. (days)
0.107	0.50		6.0	M	50.6	
	0.48		9.2	M		
	0.47		14.0	M		56
0.113		0.32	6.3	N	37.7	41

Table 1D

Transference Numbers of Sodium
and Chloride Ions in VR 4 at 25°C

NaCl Conc. (N)	t_+	t_-	Applied Potential (V)	Specimen	Thickness (μm)	Age in Soln. at End of Exper. (days)
0.107	0.68		3.1	O	86.5	
	0.34		9.3	O		
	0.52		6.15	O		
	0.79		14.0	O		41
0.116		0.342	3.1	P	39.8	
		0.292	9.3	P		
		0.290	6.3	P		41

applied to these results indicates that the sum of the sodium and chloride transference numbers are significantly different from one at the 99.9% confidence level. Similar results were obtained when the t test was applied to all the results obtained with O PUR regardless of the concentration of the bathing solution.

These transference-number results are strong evidence that sodium and chloride ions do not carry all the current through sheets of O PUR immersed in aqueous sodium chloride solution; however, the statistical arguments presented above would be invalid if a systematic error in the experiments or data analysis were present. In order to check the experimental and theoretical method, experiments were performed with a commercial cation exchange membrane (Nafion 7-1100). The apparatus used to determine transference numbers in Nafion was different from that used with paints, but the same type of experiments were perforemd with both materials. Pintauro (10) had previously examined specimens of Nafion cut from the same sheet as the specimens tested in these experiments. He determined the cation transference number (t_+) to be 0.96. He employed conventional gravametric and titration methods in his determination. The experiments with radiotracers which were conducted in this laboratory indicated that t_+ = 0.99 with a maximum error band of about 0.06. It is therefore concluded that the experimental method and theoretical analysis employed in these experiments provides an accurate method of determining transference numbers, and that the sum of the sodium and chloride transference numbers in O PUR is significantly less than one.

Of the other paints on which Hittorf experiments were performed, only in VR 4 did the sum of the sodium and chloride transference numbers approach one ($t_+ + t_- = 0.89 \pm 0.2$). The experiments with N PUR and VR 3 both produced low values of the sum ($t_+ + t_-$). Not as many experiments were performed with the three other paints as were performed with O PUR. Nevertheless, the results indicate that some species other than sodium and chloride ions often carry current through unpigmented paint films immersed in sodium chloride solution. It also appears that some paints may behave in the more conventional manner with migration of sodium and chloride ions constituting the primary current carrying species.

Generally it was observed that the transference numbers of sodium and chloride were independent of the applied membrane voltage. The results illustrated in Table 1 show that the transference numbers did not change when the voltage applied across a paint film varied. Some variation of transference numbers was observed when different paint specimens were tested, but overall the transference numbers appear to be independent of applied voltage.

Transference numbers were also observed to be relatively independent of membrane age. Paint specimens which had been in salt solution for up to four months were used in some Hittorf experiments. Although some characteristics of the paints changed dramatically in this time period the transference numbers appeared to exhibit only small, random variations.

Transference numbers also appeared to be relatively independent of the salt concentration in the external solutions. The scatter in t_+ appeared to increase as the salt concentration decreased, but the variations between paint specimens were generally more than the variations produced by concentration changes. In fact the variations between specimens appeared to be the major variability encountered in these experiments. One experiment (#4) was conducted at a temperature of 32°C. In this experiment, the transference number for chloride was reduced relative to the values obtained at 25°C, but conclusions cannot be drawn from the results of one experiment.

Electrical Conductivity and Ion Permeability Coefficients

The electrical conductivity and ion permeability coefficients obtained in Hittorf experiments are summarized in Tables 2A-2D. From the tabulated results it is clear that the conductivities of these coatings exhibit great variability. Table 2 shows how the time-averaged conductivity varied for different paint specimens. The table also shows how the conductivity of single specimens of O PUR varied with time. The variability of the conductivity with time was the same order of magnitude as the variability between specimens. Changes in the salt concentration of the bathing solution also affected the conductivity but in a manner not illustrated by the data in Table 2.

Fig. 5 shows the conductivity of O PUR as a function of the salt concentration in the bathing solution. The points are normalized conductivities

Table 2A

Electrical Conductivity and

Ion Permeability Coefficients for O PUR at 25°C

NaCl Conc. (N)	Mean Conductivity (S/m)	Permeability Coefficient (m^2/s)		Applied Potential (V)	Specimen No.
		Na^+	Cl^-		
0.009	1×10^{-8}	8.0×10^{-18}		9.3	A
0.023	3.5×10^{-10}		1.0×10^{-18}	4.4	B
			1.1×10^{-18}	9.4	B
			1.7×10^{-18}	19.5	B
			8.3×10^{-19}	13.7	B
0.023	5×10^{-9}	1.68×10^{-18}		3.0	B
0.023	1×10^{-9}	3.32×10^{-18}		3.0	B
		6.31×10^{-18}		6.1	B
		5.97×10^{-18}		9.3	B
		6.45×10^{-18}		12.5	B
		6.83×10^{-18}		6.1	B
		5.23×10^{-18}		9.2	B
0.025	5×10^{-9}	2.7×10^{-18}		4.0	C
		4.9×10^{-18}		9.9	C
		7.3×10^{-18}		19.0	C
0.037	1×10^{-8}	8.0×10^{-18}		9.3	D
0.100	4.1×10^{-8}	4.8×10^{-18}		9.3	E
0.100	3.8×10^{-8}		3.0×10^{-18}	9.3	E
0.100	2.6×10^{-8}	1.7×10^{-18}		13.6	E
0.100	8.8×10^{-8}		5.9×10^{-18}	13.4	E
0.100	6.3×10^{-8}	6.7×10^{-18}		16.4	E
0.100	1.3×10^{-10}		7.3×10^{-20}	16.6	E

Table 2A (Con't)

NaCl Conc. (N)	Mean Conductivity (S/m)	Permeability Coefficient (m^2/s)		Applied Potential (V)	Specimen No.
		Na^+	Cl^-		
0.100	2.0×10^{-9}		1.2×10^{-18}	8.8	F
0.100	8.9×10^{-10}	1.3×10^{-18}		8.8	F
0.100	7.6×10^{-10}		1.2×10^{-18}	13.4	F
0.100	4.8×10^{-10}	5.8×10^{-19}		13.4	F
0.100	8.1×10^{-10}		2.6×10^{-19}	16.3	F
0.100	1.4×10^{-9}	1.4×10^{-18}		16.2	F
0.300	3×10^{-9}			3.0	G
			8.0×10^{-19}	6.25	G
			1.05×10^{-18}	12.5	G
			1.47×10^{-18}	9.5	G
			2.31×10^{-18}	6.3	G
0.302	1×10^{-10}	7.9×10^{-19}		6.1	H
		9.9×10^{-20}		9.3	H
		1.0×10^{-20}		9.3	H
		1.2×10^{-20}		23.5	H
1.00	1×10^{-10}		6.16×10^{-19}	6.2	I
0.128*	1.5×10^{-9}		6.6×10^{-20}	2.9	Q
			3.1×10^{-19}	4.4	Q
			6.6×10^{-20}	5.8	Q
			1.0×10^{-18}	2.9	Q

* Experimental Temperature = 32°C

Table 2B

Electrical Conductivity and

Ion Permeability Coefficients for N PUR at 25°C

NaCl Conc. (N)	Mean Conductivity (S/m)	Permeability Coefficient (m^2/s)		Applied Potential (V)	Specimen No.
		Na^+	Cl^-		
.094	2.5×10^{-8}	1.6×10^{-16}		6.0	J
		1.1×10^{-16}		1.5	J
		9.8×10^{-17}		.73	J
		5.5×10^{-17}		1.55	J
		1.4×10^{-17}		3.0	J
.111	6×10^{-8}		5.6×10^{-17}	3.1	K
			3.0×10^{-17}	1.55	K
			2.4×10^{-17}	0.7	K
			2.7×10^{-17}	2.9	K
.113	4.5×10^{-11}			3.2 - 9.4	L

Table 2C

Electrical Conductivity and

Ion Permeability Coefficients for VR 3 at 25°C

NaCl Conc. (N)	Mean Conductivity (S/m)	Permeability Coefficient (m^2/s)		Applied Potential (V)	Specimen No.
		Na^+	Cl^-		
.107	1×10^{-9}	4.3×10^{-17}		6.0	M
		2.1×10^{-17}		9.2	M
		1.3×10^{-17}		14.0	M
.113	3×10^{-9}		5.9×10^{-17}	6.3	N

Table 2D

Electrical Conductivity and

Ion Permeability Coefficients for VR 4 at 25°C

NaCl Conc. (N)	Mean Conductivity (S/m)	Permeability Coefficient (m^2/s)		Applied Potential (V)	Specimen No.
		Na^+	Cl^-		
0.099	1×10^{-11}			1.55	R
0.104	5×10^{-11}			1.52	S
0.107	9×10^{-9}	2.3×10^{-17}		3.1	O
		8.0×10^{-18}		9.3	O
		1.3×10^{-17}		6.15	O
		9.1×10^{-18}		14.0	O
0.116	5×10^{-9}		1.7×10^{-17}	3.1	P
			2.2×10^{-18}	9.3	P
			3.1×10^{-18}	6.3	P

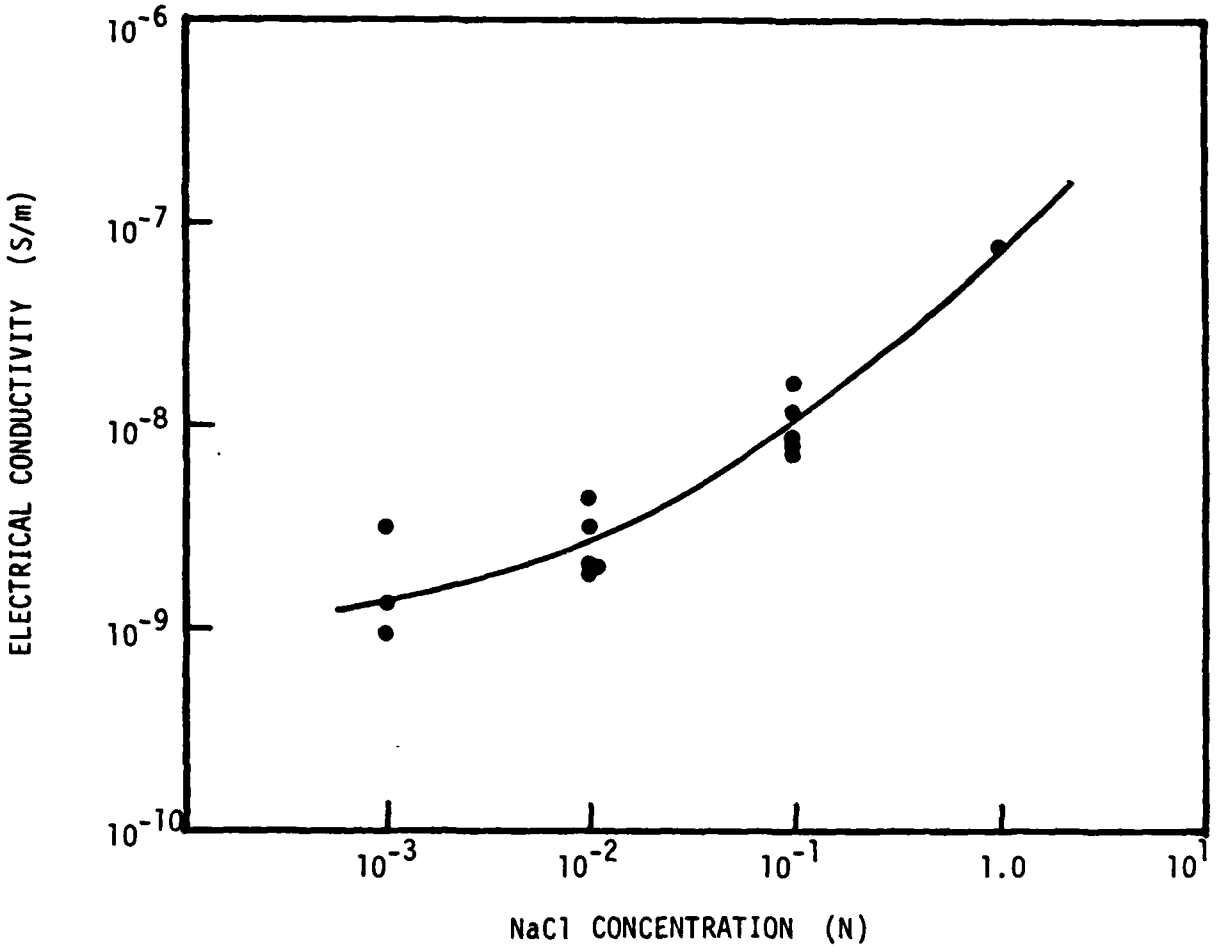

Fig. 5. Electrical conductivity of O PUR as a function of sodium chloride concentration in the external bath at 25°C.

obtained from a number of different paint films. Each paint film exhibited a different conductivity at any given NaCl concentration, but the curvature in the conductivity versus concentration plot was about the same for each different paint film. In Fig. 5 the data for each paint specimen have been normalized to pass through a single value of the conductivity when the salt concentration was 1.0 N. This procedure eliminates the scatter caused by testing different specimens and illustrates the concentration dependence of the conductivity. The curves pass through the point (8×10^{-8}, 1.0) because the average absolute conductivity in 1.0 N NaCl is about 8×10^{-8} S/m.

The ion permeability coefficients determined from Hittorf experiments are also provided in Table 2. The ion permeability coefficients vary over 2 to 3 orders of magnitude, and roughly parallel the conductivity. This suggests that when the conductivity increases the permeability coefficients of both sodium and chloride rise. This mechanism is consistent with the observation that both sodium and chloride transference numbers, which are closely related to the ratio of permeability coefficients, are relatively constant.

An example of typical data illustrates the relationship between membrane conductivity, ion permeability coefficient, and transference number. Figure 6 shows how the activity of chloride-36 changes with time. The applied membrane voltages are also shown in the figure. Figure 7 illustrates how the membrane conductivity varied with time. The points in Fig. 7 represent values calculated from instantaneous observations of membrane voltage and current. The curve is an "average" conductivity drawn "by eye" through the points. Figure 8 shows how the total charge varied with time. The total charge was obtained by electronically integrating the current passing through the paint film. Figure 9 illustrates that the chloride ion transference number was constant during this experiment. Figure 9 shows how the Coulomb equivalents of chloride vary with total charge. It is clear that these data are well represented by a single straight line regardless of the applied voltage. The chloride ion transference number is equal to the slope of the line. Figure 10 illustrates how the chloride-ion permeability coefficient depends on conductivity. Permeability coefficients were calculated for each time interval when the applied voltage was constant. Average conductivities were

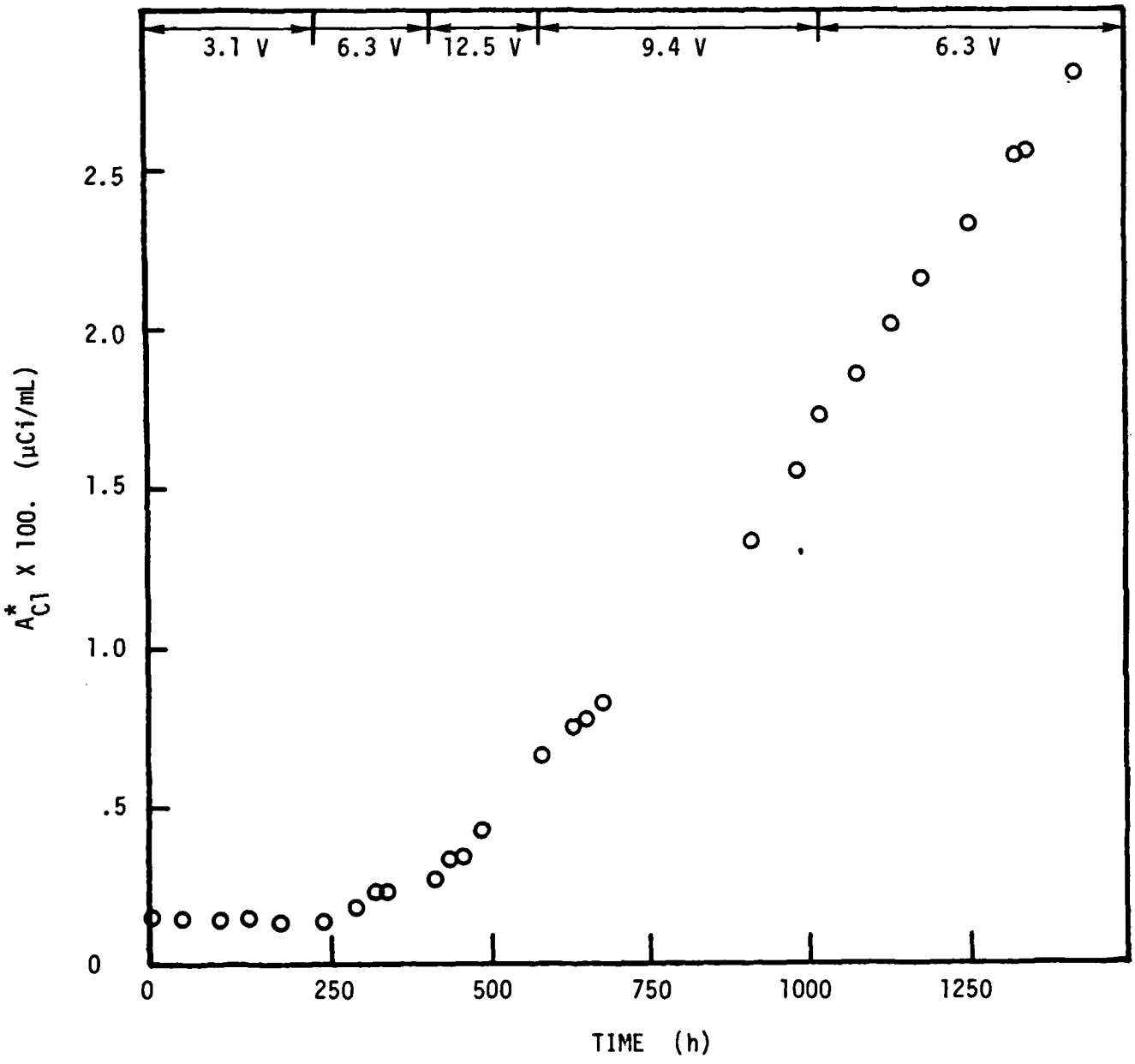

Fig. 6. Radioactive activity of chloride-36 in the top cell of Hittorf experiment A employing O PUR.

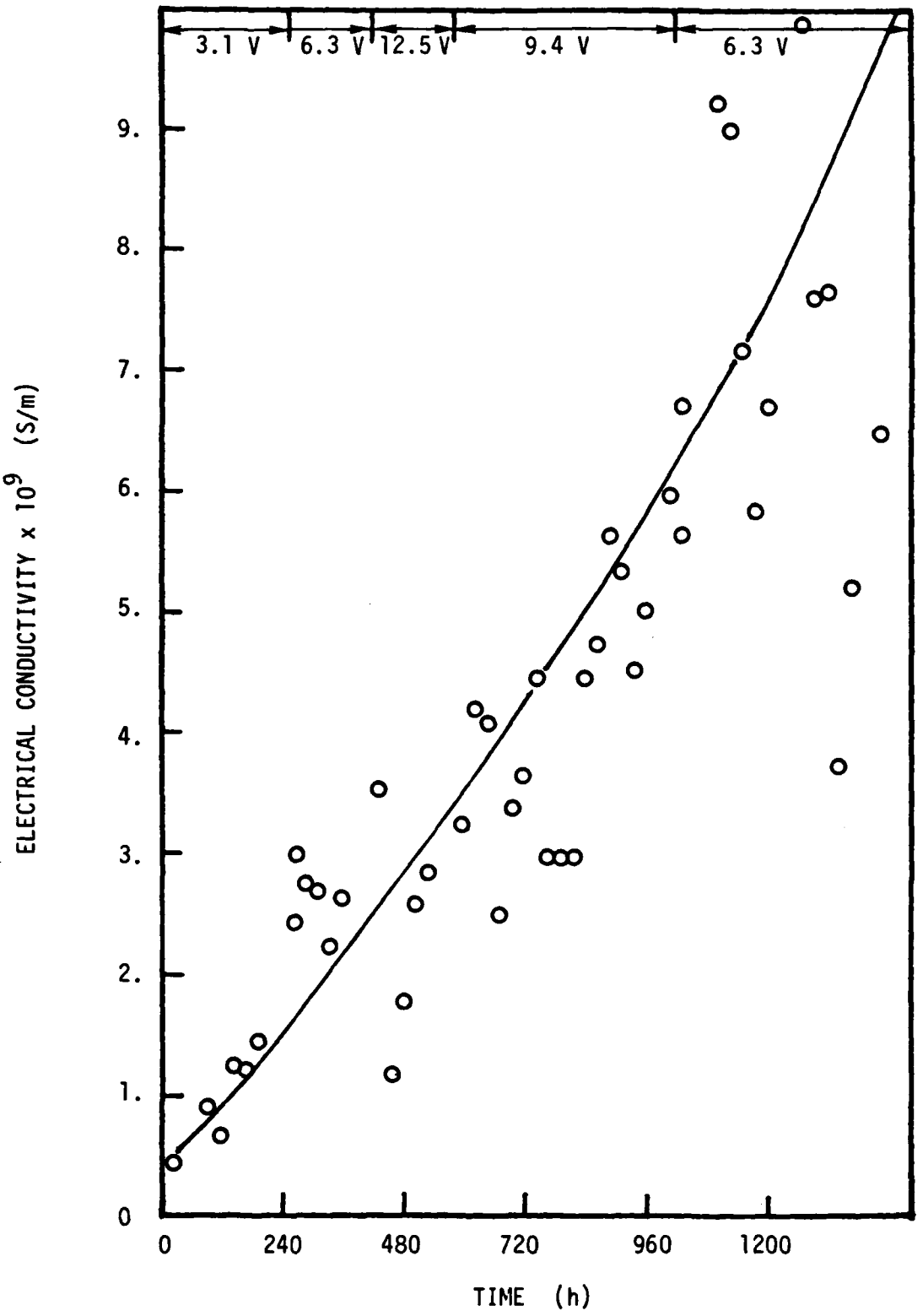

Fig. 7. Electrical conductivity versus time in Hittorf experiment A employing O PUR.

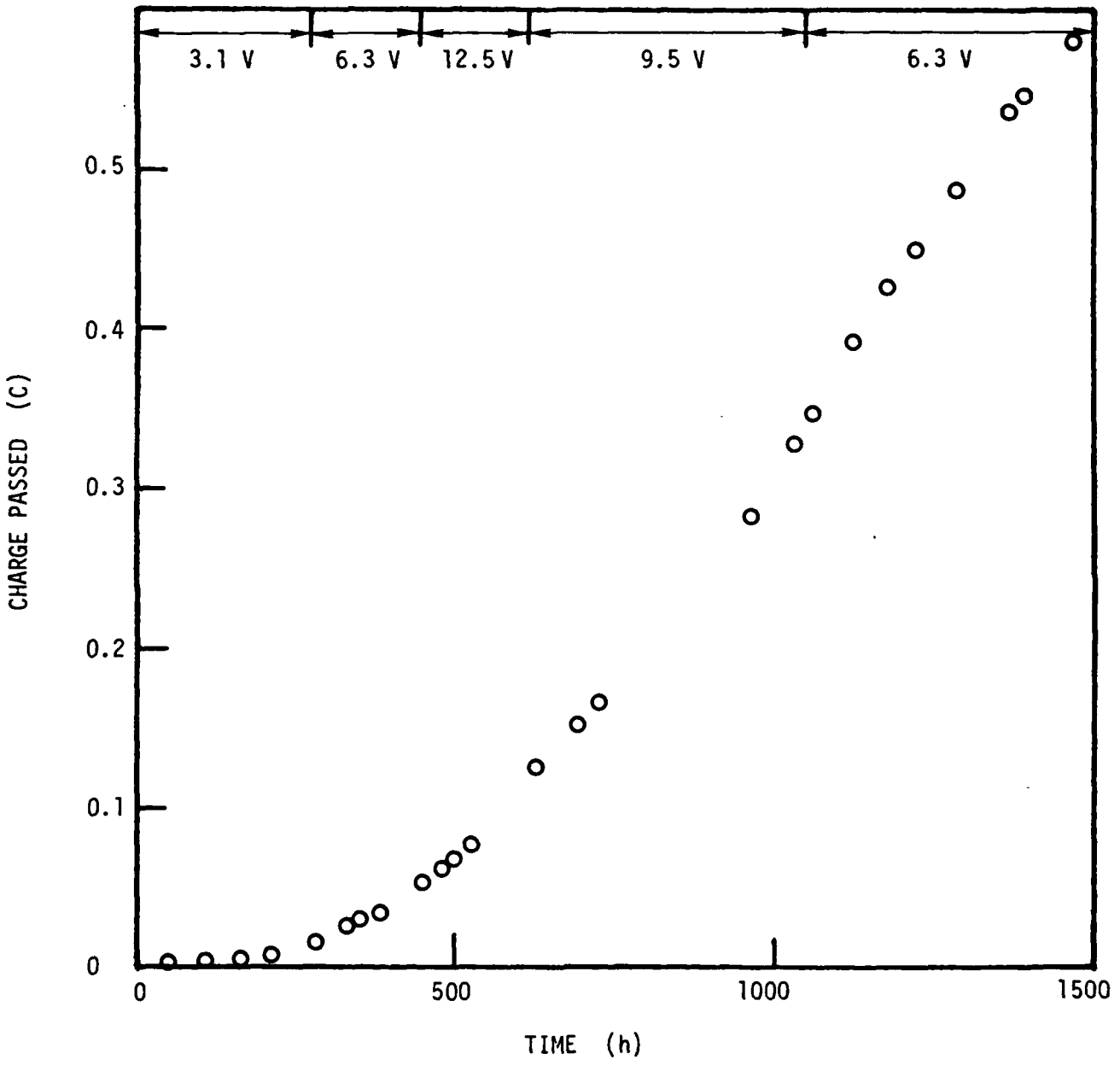

Fig. 8. Charge passed through O PUR paint in Hittorf experiment A.

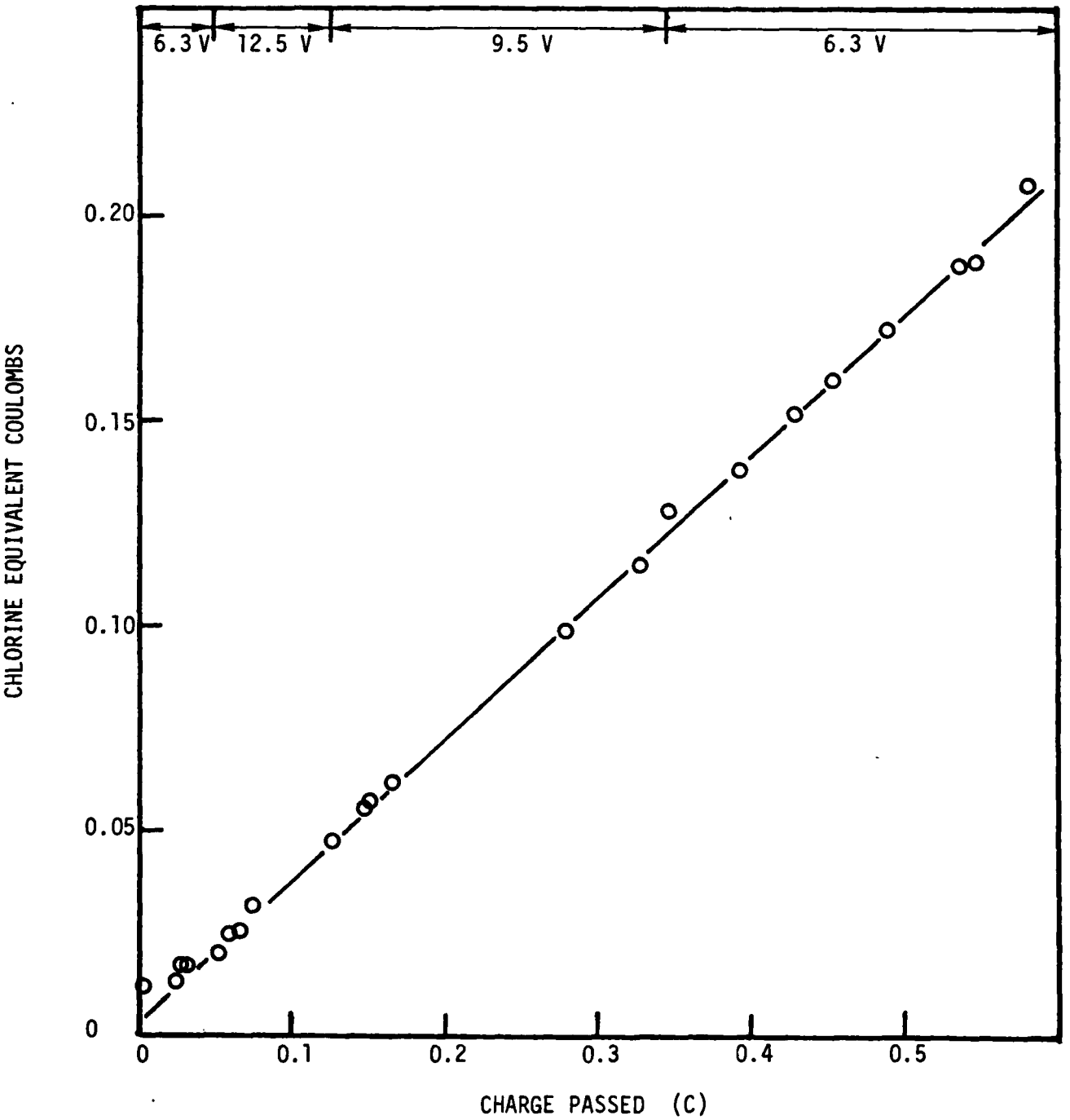

Fig. 9. Chlorine equivalent coulombs versus charge for Hittorf experiment A employing O PUR. Least squares straight line; slope = 0.399, R = 0.9995.

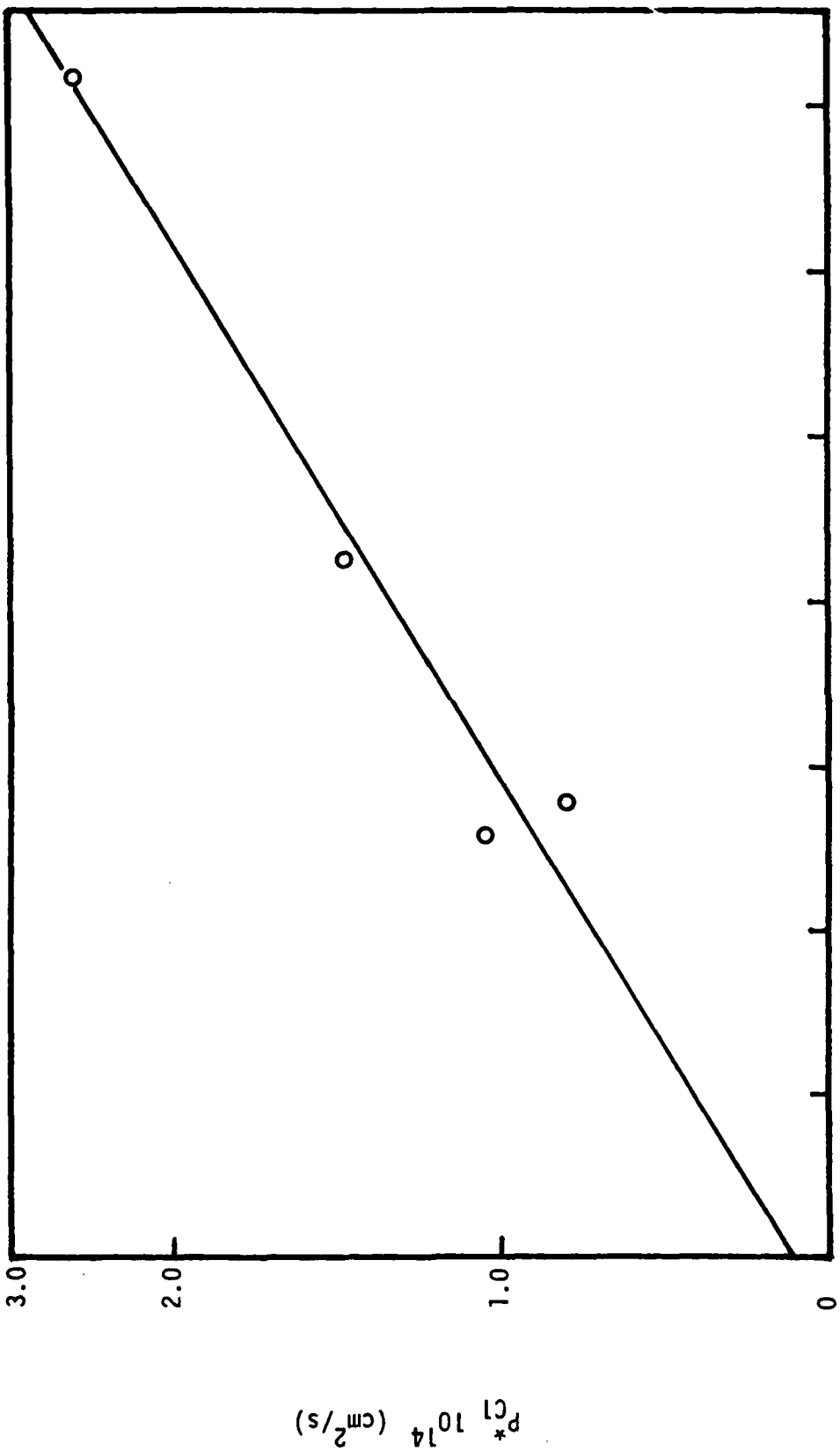

Fig. 10. Chloride ion permeability coefficient versus electrical conductivity for Hittorf experiment A employing O PUR. The line is a least squares fit of the data.

calculated from values of the applied voltage and average current. The average current was obtained from the net total charge for the period divided by the elapsed time. Figure 10 shows that the permeability coefficient is a linear function of the membrane conductivity. A similar relationship has been obtained in other experiments in which both the conductivity and permeability coefficient varied as much as two orders of magnitude.

Water Transport

Radiotracer Results

The transport of tritium through paints was determined in the Hittorf experiments. The tritium was assumed to be transported only as a component of the water molecule. Table 3 lists the permeability coefficients obtained from Hittorf experiments. The most striking contrast between the permeability coefficients of water and of ions is the difference in variability. The permeability coefficients of water showed no significant variation with time in the course of any single experiment whereas the permeability coefficients of ions sometimes showed variations of more than two orders of magnitude. The variability between experiments and between paint specimens was also much less for water permeabilities than for those of ion. Table 3 also shows average permeability coefficients and the corresponding standard deviations for four different paints.

Crystal Oscillator Results

Water transport in paints was also studied using the humidity chamber apparatus. Both steady-state and transient data have been obtained with this equipment. Figure 11 shows typical steady state results obtained from a single painted crystal. Figure 11 represents mass change versus the partial pressure of water in the atmosphere surrounding the crystal. The points represent experimental data, and the straight line is a least-squares fit of the data. These data constitute an absorption isotherm for a single paint specimen. The slope of the straight line is closely related to the Henrys law constant for water in 0 PUR.

Five types of paint were studied with the crystal oscillator apparatus. The most extensive data were obtained with 0 PUR. Table 4 summarizes the absorption isotherm data for 0 PUR, and Table 5 shows results obtained with the other paints.

Table 3

Permeability Coefficient of Water in Paints at 25°C

$10^{10} \times P_w$ (cm^2/s)

NaCl Conc. (N)	Specimen	O PUR	N PUR	VR 3	VR 4
0.009	A	5.6			
0.023	B	7.5			
0.025	C	4.4			
0.037	D	6.1			
0.100	E	5.9			
	E	5.8			
	E	4.4			
	E	4.6			
	E	5.3			
	E	4.1			
0.100	F	5.5			
	F	6.2			
	F	4.8			
	F	4.6			
	F	5.1			
	F	4.1			
0.30	G	5.4			
0.302	H	4.2			
1.0	I	4.4			
0.094	J		1.8		
0.111	K		2.4		
0.113	P		5.6		
0.107	L			2.1	
0.113	M			1.9	
0.099	Q				2.1
0.104	R				1.6
0.107	N				4.0
0.116	O				2.8
Average		5.5	3.3	2.0	2.6
Standard Deviation		1.5	2.0	0.1	1.0

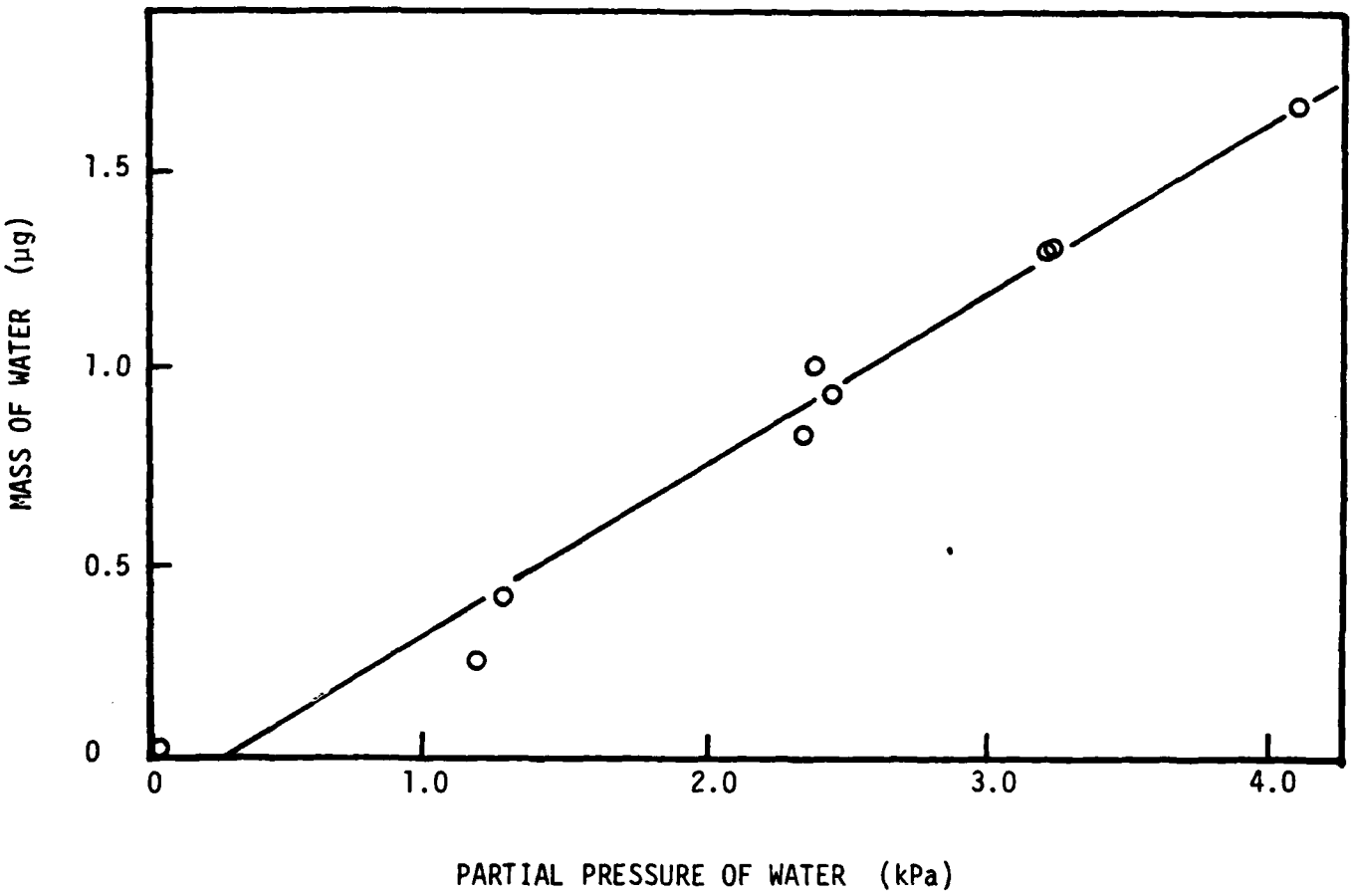

Fig. 11. Water uptake by O PUR at 30.2°C.

Table 4

Absorption Isotherm Data

for Water in O PUR

Crystal #	Paint Mass (μg)	Slope $\left(\frac{ng\text{-}H_2O}{Pa}\right)$	Standard Deviation $\left(\frac{ng\text{-}H_2O}{Pa}\right)$	Straight Line Correlation Coefficient	Average Temp. (°C)
22	8.05	0.224	0.025	0.965	30.2
21	8.83	0.158	0.014	0.966	30.7
24	46.32	0.458	0.043	0.975	30.4
33	52.56	0.414	0.026	0.984	30.8
7	81.16	0.595	0.024	0.989	30.5
22	8.05	0.131	0.025	0.907	35.4
21	8.83	0.251	0.052	0.924	35.8
24	46.32	0.244	0.035	0.962	35.9
33	52.56	0.277*	0.018*	0.996*	35.3
7	81.16	0.464	0.034	0.982	35.2
22	8.05	0.090	0.011	0.969	40.8
21	8.83	0.183	0.028	0.938	41.1
24	46.32	0.201	0.022	0.972	40.7
7	81.16	0.389	0.018	0.994	40.3

*Straight line based on only four experiments due to crystal failure.

Table 5

Solubility and Diffusivity of Water

in Paints at 30°C

Paint	Crystal	Paint Mass (μg)	Paint Thickness (μm)	Water Solubility $\left(\frac{\text{x } 10^3 \text{ ng-H}_2\text{O}}{(\mu\text{g-Paint})(\text{Pa})}\right)$	Water Diffusivity x 10^{10} (cm^2/s)
N PUR	71	30.4	0.98	5.56	1.1
N PUR	70	72.6	2.3	6.58	3.5
N PUR	69	73.5	3.2	5.66	7.8
N PUR	67	127.0	4.1	5.43	8.1
N PUR	68	141.0	4.5	7.98	8.2
VR 2	44	16.3	0.53	17.9	0.54
VR 2	46	21.6	0.70	23.5	0.88
VR 2	45	103.0	3.3	19.7	11.0
VR 2	43	134.0	4.4	22.7	11.0
VR 2	47	135.0	4.4	16.7	8.3
VR 3	37	73.9	2.1	1.47	6.4
VR 3	36	151.0	4.3	1.36	43.0
VR 3	35	189.0	5.6	1.96	41.0
VR 4	50	11.6	0.42	8.94	0.25
VR 4	51	13.6	0.42	8.09	0.48
VR 4	52	15.4	0.48	7.82	0.18
VR 4	49	99.9	3.1	5.35	7.7
VR 4	48	107.0	3.3	5.92	7.0
O PUR	22	8.05	0.25	24.5	
O PUR	22	8.05	0.25	25.7	
O PUR	21	8.83	0.50	17.0	
O PUR	21	8.83	0.50	17.4	
O PUR	24	46.3	1.4	8.55	
O PUR	24	46.3	1.4	5.01	
O PUR	33	52.6	1.6	6.63	
O PUR	33	52.6	1.6	6.75	
O PUR	7	81.2	2.4	6.38	
O PUR	7	81.2	2.4	6.51	

If the absorption of water in O PUR obeys Henrys law, a plot of the slopes from Table 4 versus mass of paint should yield a straight line which passes through the origin. Figure 12 shows such a plot for O PUR. The data are well represented by straight lines, but they do not pass through the origin. Statistical evaluation of the linear correlation coefficients indicates that the probability that these data are uncorrelated is less than 10%.

If the slopes listed in Table 4 are divided by the corresponding mass of the paint, the result will represent an average Henrys law "constant" for the paint. Table 6 shows that Henrys law constants calculated in this manner are not constant but increase as the thickness of the coating decreases. This result means that water is more soluble in thinner coatings and raises the possibility that more than one phase is present in these O PUR specimens.

A more detailed interpretation of the data shown in Fig. 12 will now be considered. It is assumed that the absorption isotherms for a single phase should obey Henrys law and be represented by straight lines. The fact that the isotherm lines in Fig. 12 do not pass through the origin indicates that the painted crystal is absorbing water, in the limit, at zero coating thickness. Experiments have been performed with uncoated crystals, and a small frequency decrease was observed, but it was much less than that required to explain the large intercepts shown in Fig. 12. It is likely that the lines in Fig. 12 eventually curve down toward the origin as the mass of paint is decreased below 8 μg, but the mass at which this takes place cannot be assessed from these data. Accordingly, the results may be interpreted as a surface adsorption of water. These data do not allow one to determine at which interface the adsorption is occurring, but an analysis of the non-steady state results indicates that the surface adsorption is probably at the paint-metal interface (3).

It should not be inferred from the preceding discussion that a true interfacial adsorption is present at the paint-metal interface. The 30°C intercept in Fig. 5 represents about 2.3 μg of water per square centimeter of painted area. This quantity of pure water would occupy a space approximately 0.02 μm thick. Therefore it is expected that the water-rich phase is between about 0.02 and 0.25 μm in thickness and does not represent an interfacial monolayer.

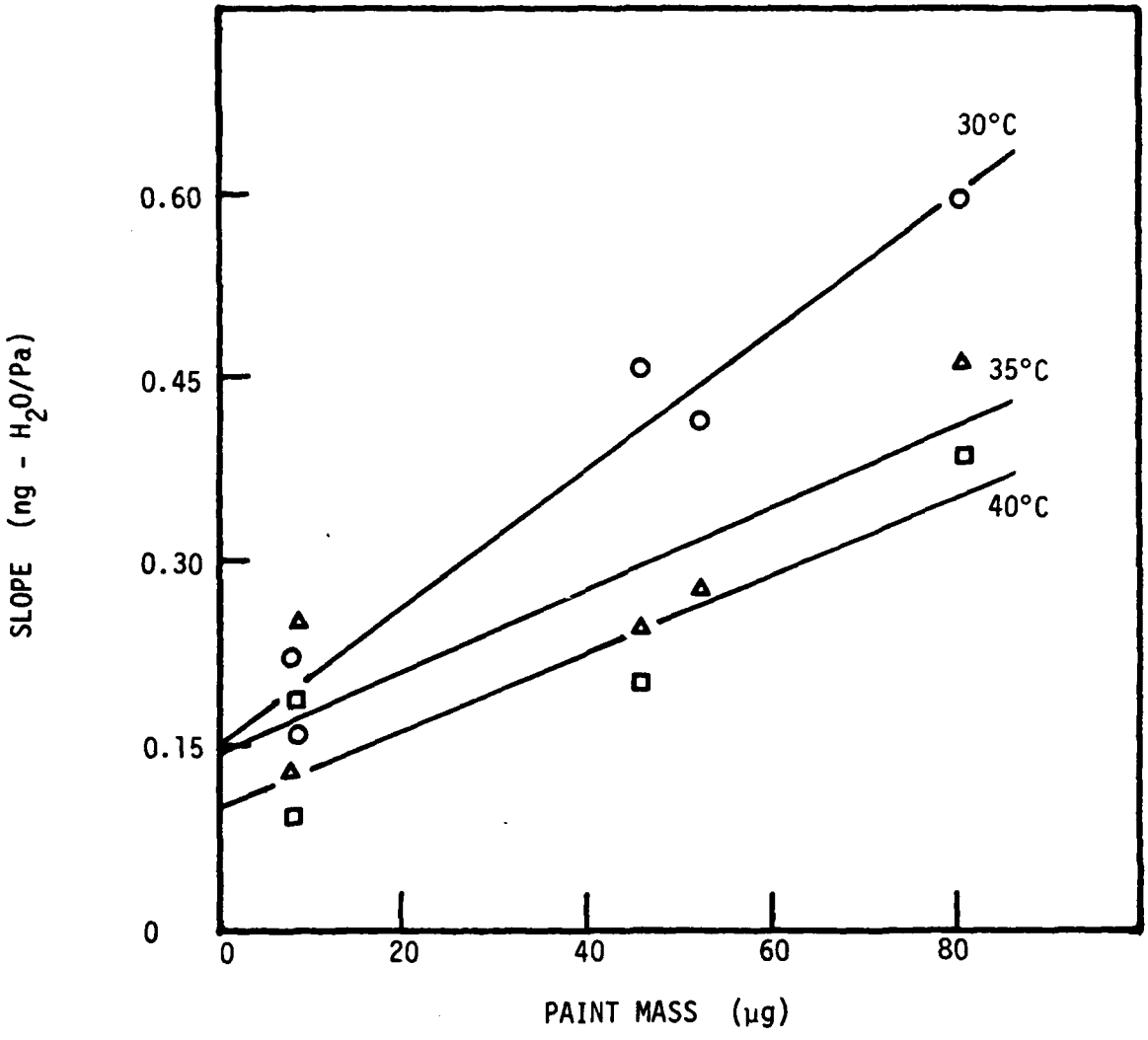

Fig. 12. Slope of absorption isotherms versus mass of O PUR at three different temperatures. Symbols are experimental points. Lines are least squares fit of the data at a single temperature.

Table 6

Average Henrys Law Constants vs Thickness for O PUR

Crystal	Paint Mass (μg)	Thickness (μm)	10^3 x Henrys Law "Constant" $\left(\frac{\text{ng-}H_2O}{(\mu\text{g-paint})(\text{Pa})}\right)$		
			30°C	35°C	40°C
7	81.16	2.4	7.33	5.72	4.79
33	52.56	1.6	7.88	5.27	--
24	46.32	1.4	9.88	5.27	4.34
21	8.83	0.50	17.8	28.4	20.7
22	8.05	0.25	27.8	16.2	11.2

The two-phase model of water absorption can be quantitatively represented as:

$$\frac{M_w}{P_w} = \frac{M_p}{H_{wp}} + \frac{A}{H_s} \qquad (2)$$

where M_w = mass of water in the paint

M_p = mass of paint

P_w = partial pressure of water

A = area of the paint-metal interface

H_{wp} = Henrys law constant for the bulk paint phase

H_s = Henrys law constant for the interfacial phase.

Values of H_{wp} and A/H_s obtained in this work are shown in Table 7.

The absorption isotherm data can in principle be used to obtain both the enthalpy and entropy of condensation for water in paints. The enthalpy of condensation has been determined at approximately 35°C from the data in Table 4. The value obtained was $\Delta\bar{h} = -41.$ kJ/mole, which corresponds to an enthalpy of mixing for paint and liquid water of $\Delta h_{mix} = 3.$ kJ/mole. The uncertainty associated with these numbers is high because of experimental errors and the fact that data were available at only three temperatures. Despite the uncertainty the enthalpy values are in the range of expectation, and the heat of condensation was used to determine the solubility of water in O PUR at 25°C when P_w = 3.17 kPa. The calculated solubility was 0.022 g-H_2O/g-paint. This value compares well with an average solubility of 0.018 g-H_2O/g-paint obtained by weighing paint specimens in a humid atmosphere.

The steady-state results indicate that the average solubility of water in O PUR is a function of coating thickness. Time transient experiments have also been performed with the crystal oscillator apparatus, and the results show that the apparent diffusivity of water in O PUR also depends on coating thickness. The diffusivity results are summarized in Figs. 13-17. It is readily apparent that the diffusivity depends on temperature, partial pressure of water, and coating thickness. The temperature dependence is expected and Arrhenius plots are approximately linear for the thicker specimens. The dependence on the water pressure is not unexpected and may be related to the plasticizing effect of water. The dependence of the diffusivity on coating thickness was unexpected however. Figures 18-20 indicate how the

Table 7

Two-Phase Model Henrys Law Constants
for Water in O PUR

Temp. (°C)	H_{wp} $\left(\frac{(M\ Pa)(g\text{-paint})}{(g\text{-water})}\right)$	A/H_s $\left(\frac{(G\ Pa)}{(g\text{-water})}\right)$
30	0.179	6.68
35	0.299	7.08
40	0.304	10.30

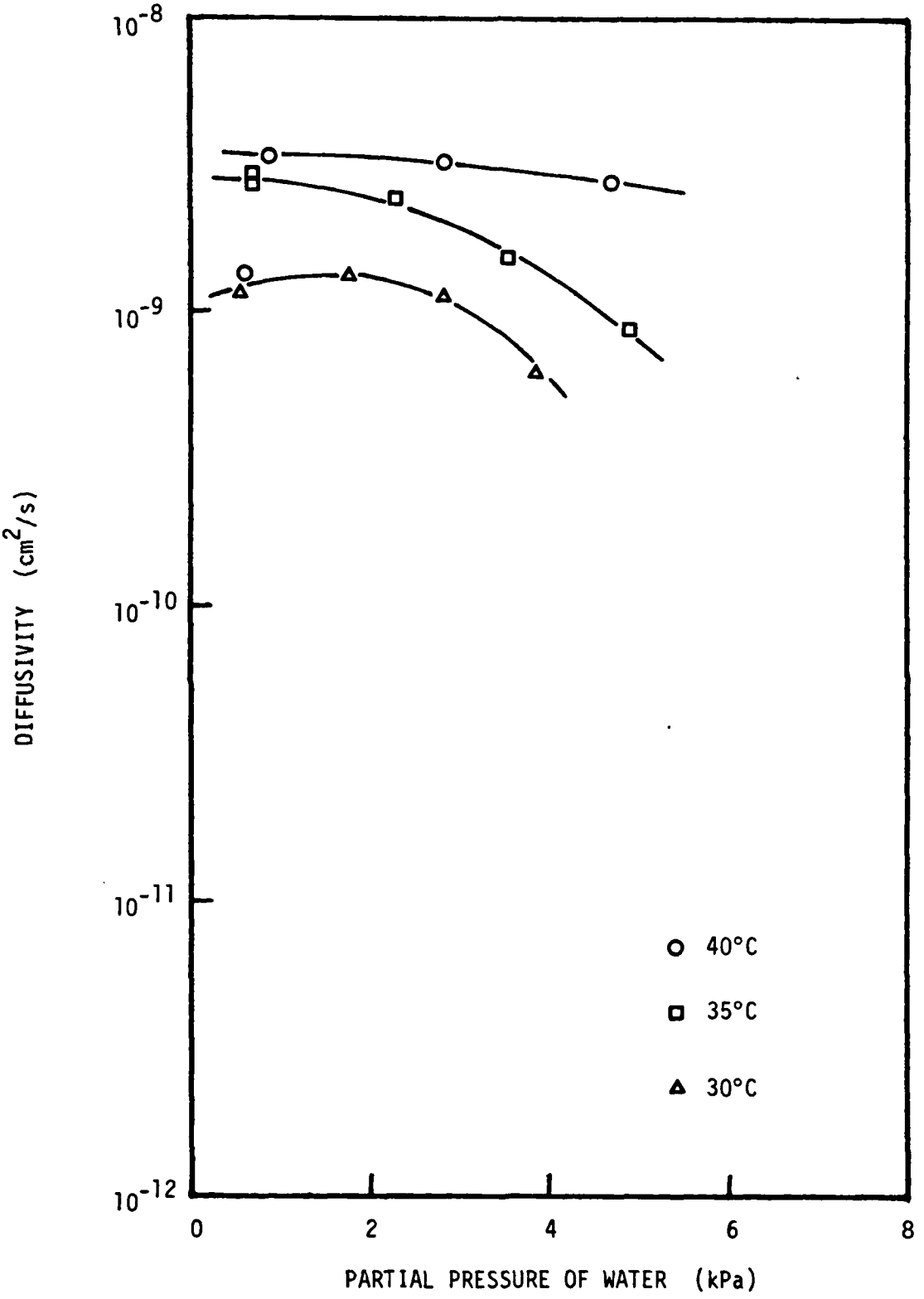

Fig. 13. Water diffusivity in O PUR as a function of water pressure and temperature. Crystal number 7. Coating thickness 2.4 μm.

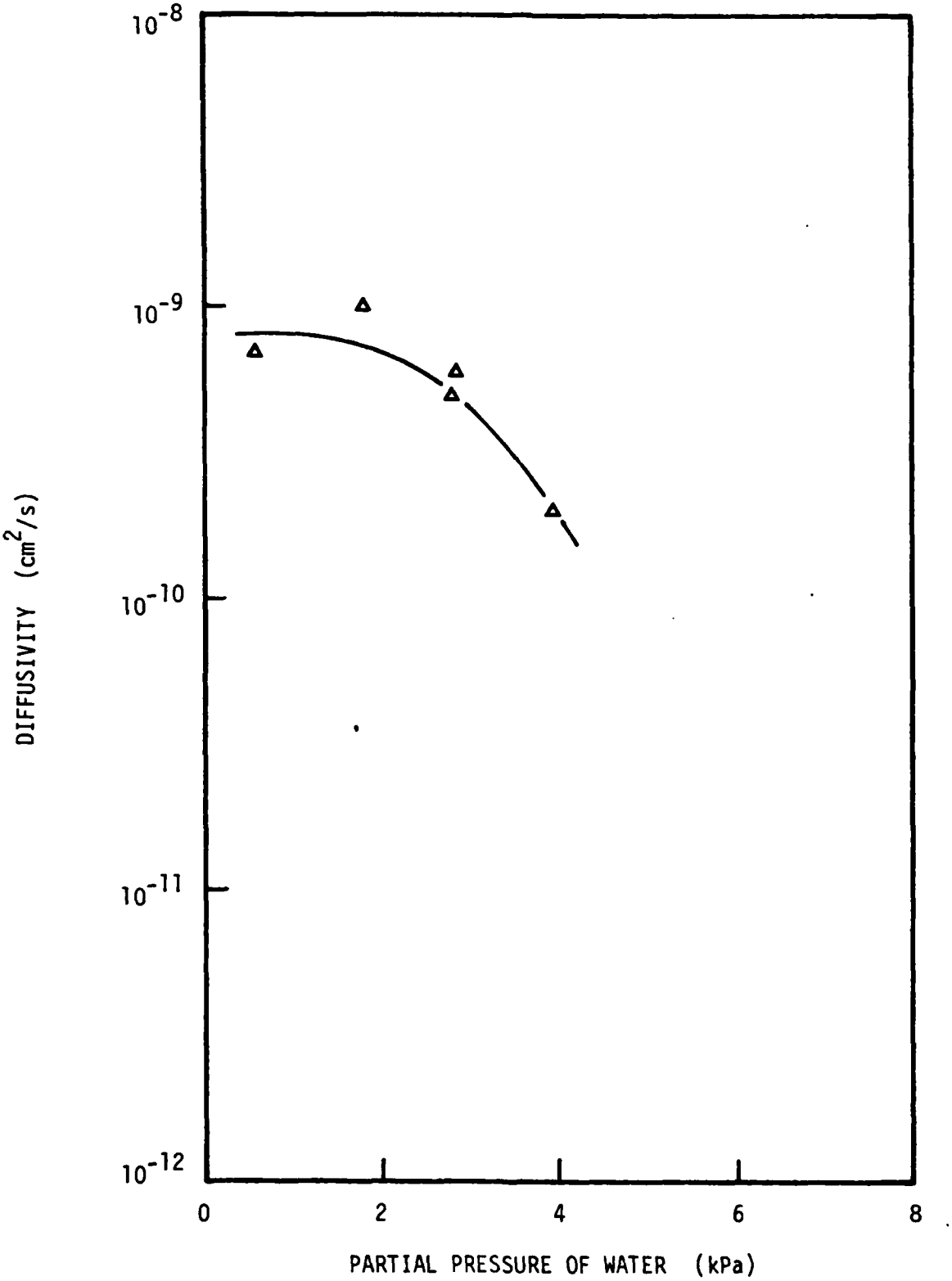

Fig. 14. Water diffusivity in O-PUR as a function of water pressure at 30°C. Crystal #33. Coating thickness = 1.6 μm.

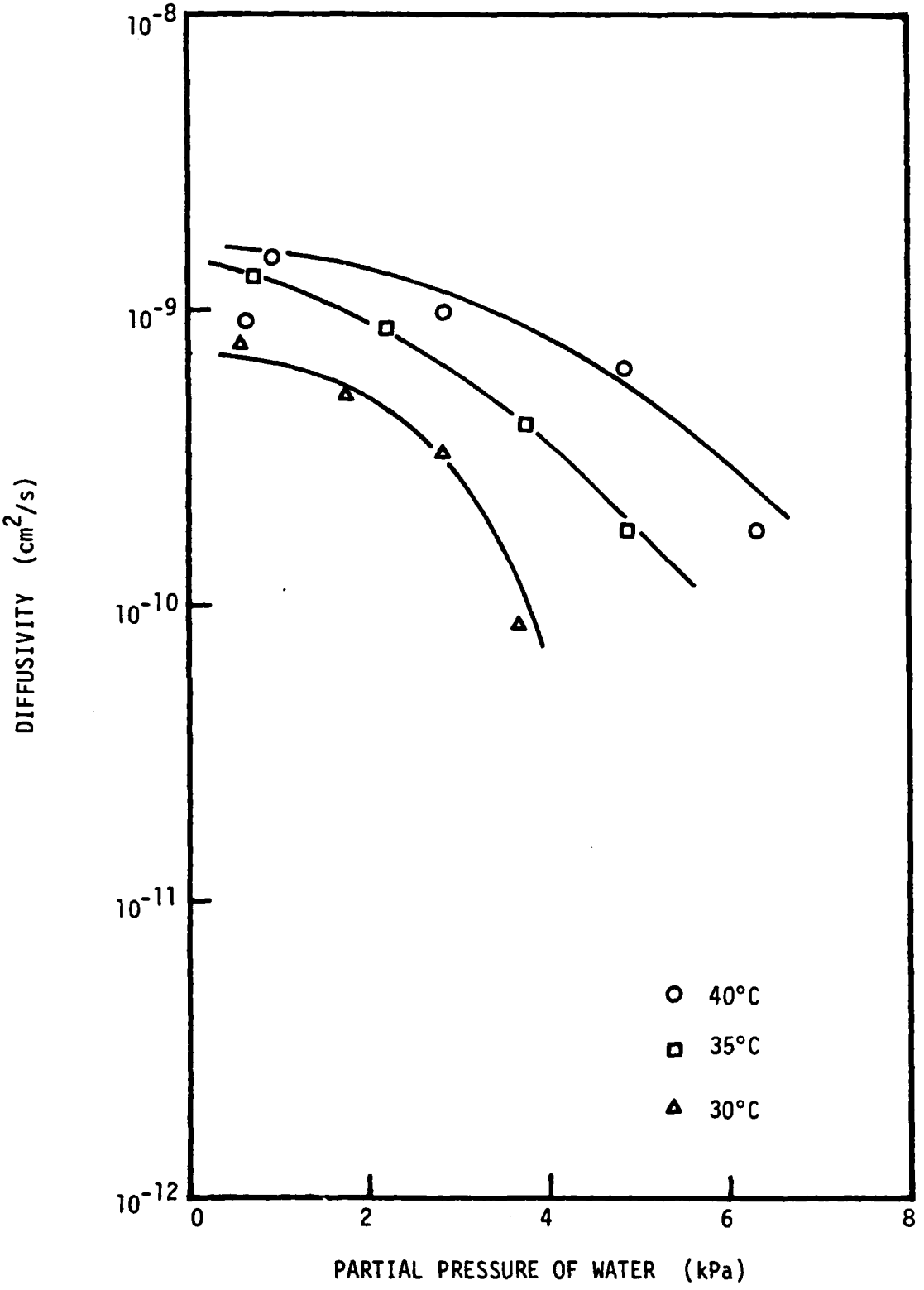

Fig. 15. Water diffusivity in O-PUR as a function of water pressure at 30°C. Crystal #24. Coating thickness = 1.4 μm.

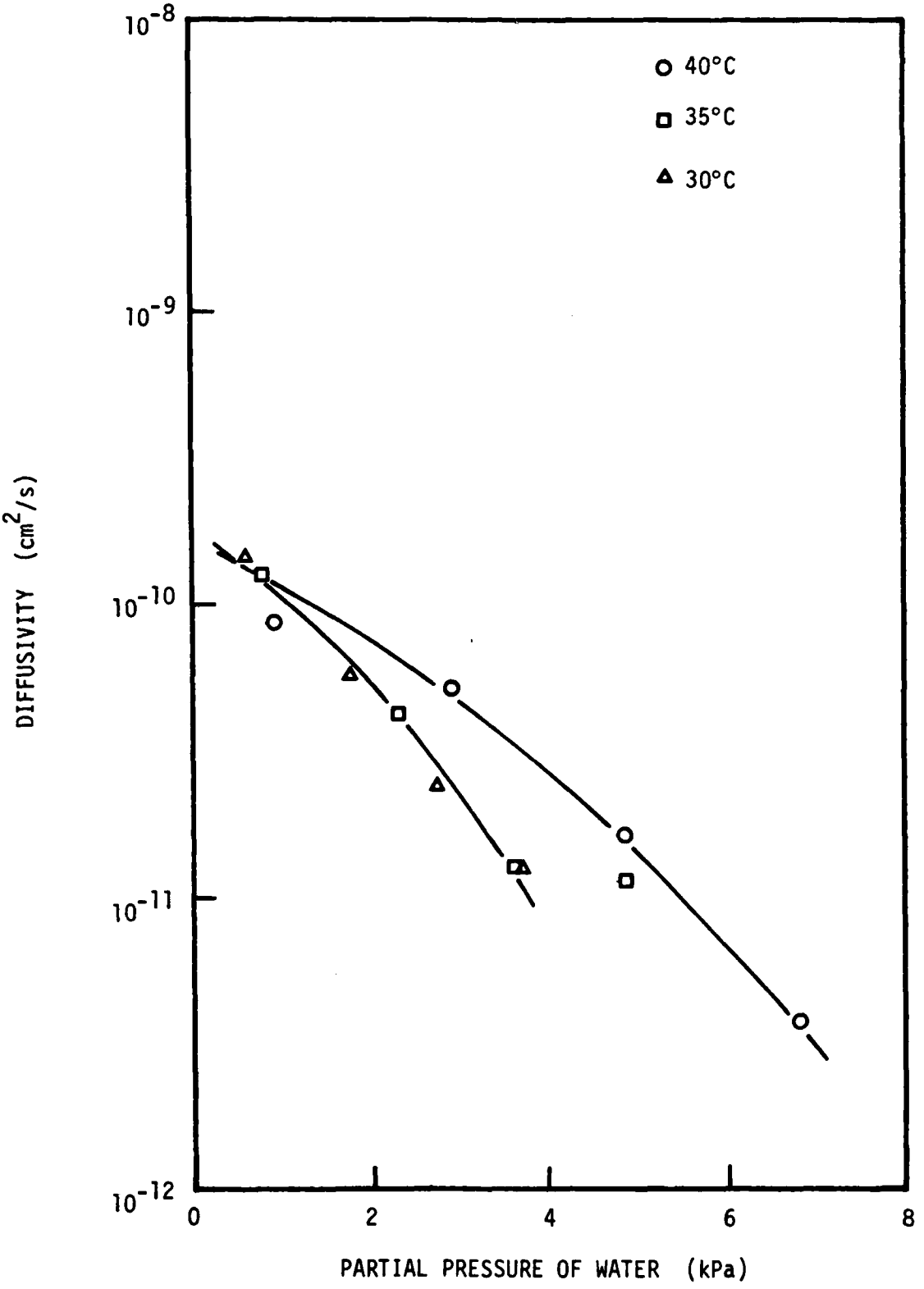

Fig. 16. Water diffusivity in O-PUR as a function of water pressure at 30°C. Crystal #21. Coating thickness = 0.50 μm.

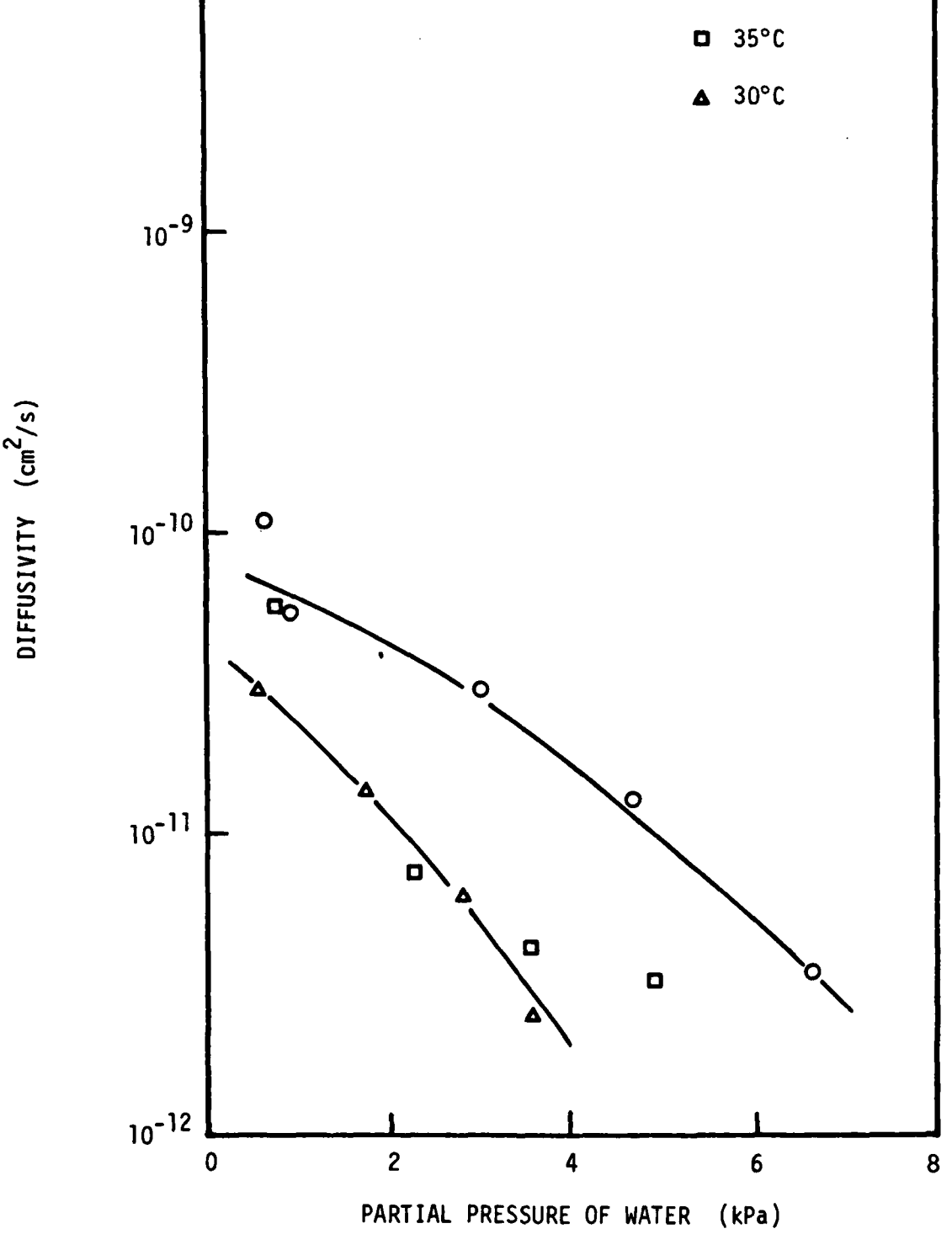

Fig. 17. Water diffusivity in O-PUR as a function of water pressure at 30°C. Crystal #22. Coating thickness = 0.25 μm.

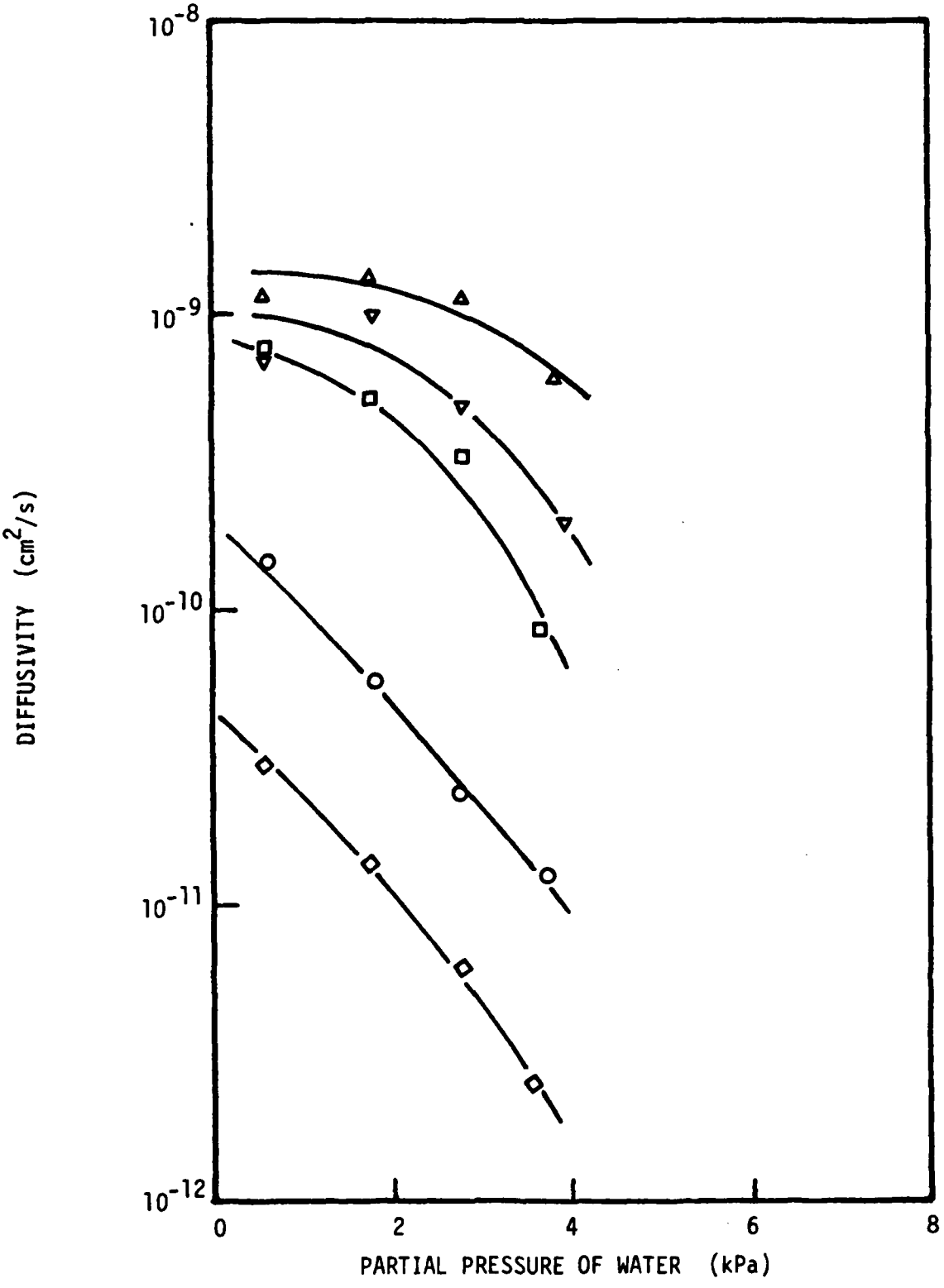

Fig. 18. Water diffusivity in O-PUR at 30°C as a function of water pressure and coating thickness.

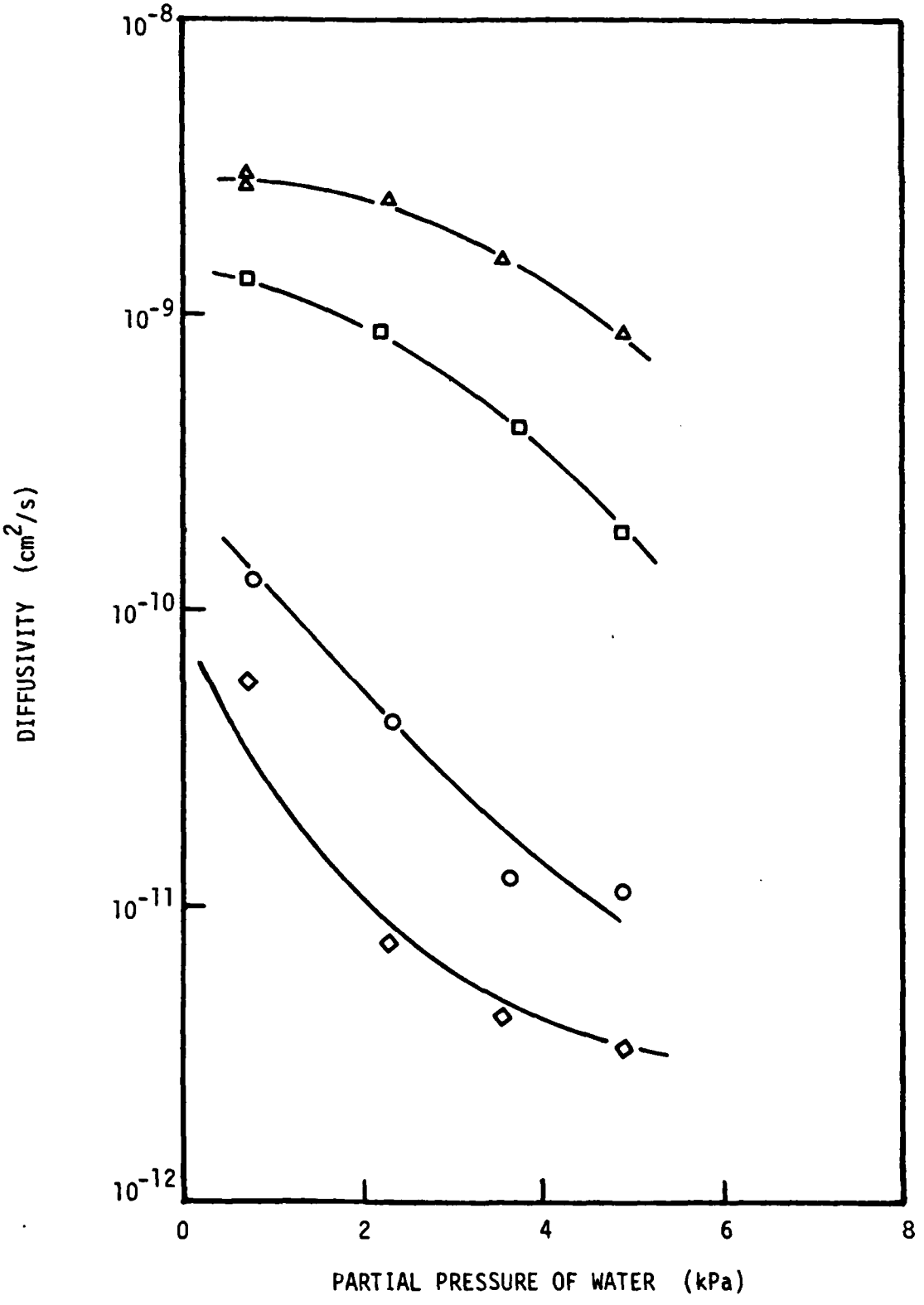

Fig. 19. Water diffusivity in O-PUR at 35°C as a function of water pressure and coating thickness.

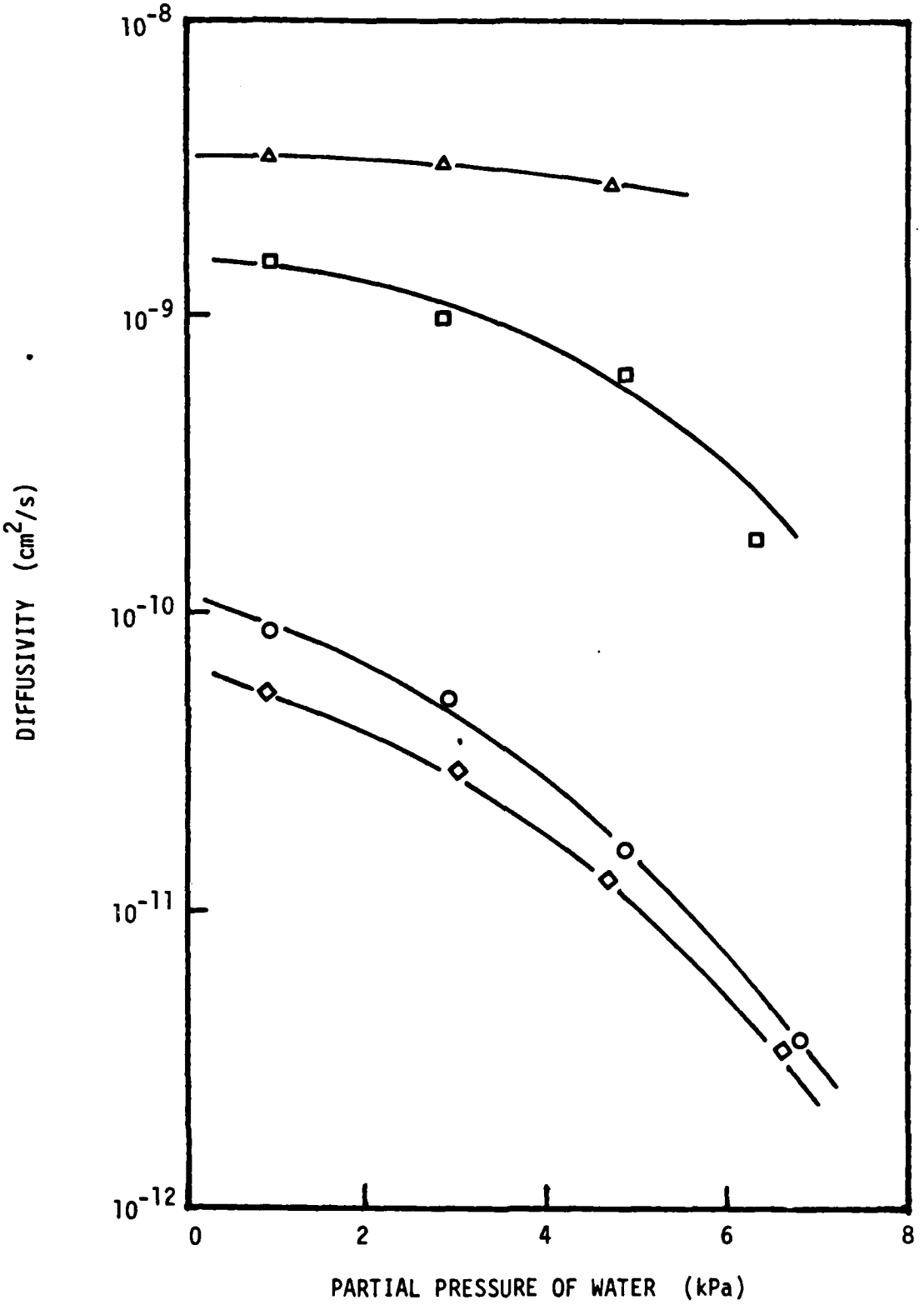

Fig. 20. Water diffusivity in O-PUR at 40°C as a function of water pressure and coating thickness.

calculated diffusivities vary with coating thickness. A trend is clearly present at all three temperatures. Figure 21 explicitly shows the relationship between diffusivity and thickness.

The diffusivities of water in O PUR were also determined from the results of Hittorf experiments. The coating thickness varied from 35 μm to 128 μm, but the diffusivity remained constant in the Hittorf experiments. The results shown in Fig. 21 indicate that the transport properties of this paint depend on coating thickness when the specimen is less than about 10 μm thick. It should be cautioned however, that two types of apparatus were used to obtain this data. The thin specimens were painted onto gold, while the thicker samples were unattached to any substrate. If a water-rich phase is present at the gold-paint interface, it could produce the apparent dependence on thickness. It is unfortunate that paint specimens of the same thickness cannot be used in both Hittorf and crystal oscillator experiments.

Figure 22 is a comparison of water sorption and desorption experiments conducted at 29.6 ± 0.4°C. It is clear from the figure that the diffusivity depends on the vapor pressure of water, and therefore, on the concentration of water in the paint. Crank (6) has discussed this type of behavior. When sorption is more rapid than desorption the diffusivity is increasing as the water concentration increases. When sorption is slower than desorption the diffusivity decreases with increasing water concentration. Figure 22 therefore indicates that the diffusivity passes through a maximum value as the water concentration increases from zero to its maximum value. This conclusion is supported by previous experimental results (3) and by the results shown in Figs. 13 and 14 for the experiments conducted at 30°C.

It is clear from these results that the transport of water through paints is a complex phenomena. The diffusivity is a complex function of water concentration and temperature. This behavior may be related to plasticizing effects and reduction of the glass transition temperature, but more work will be required to confirm this hypothesis. The diffusivity may also depend on the coating thickness if the coating is relatively thin. The equilibrium sorption of water also appears to depend on coating thickness. These results have been interpreted in terms of a water-rich phase located at the paint-metal interface. In general such a phase would be expected to be affected by the nature of both the coating and the metal; however, the water-rich phase appears

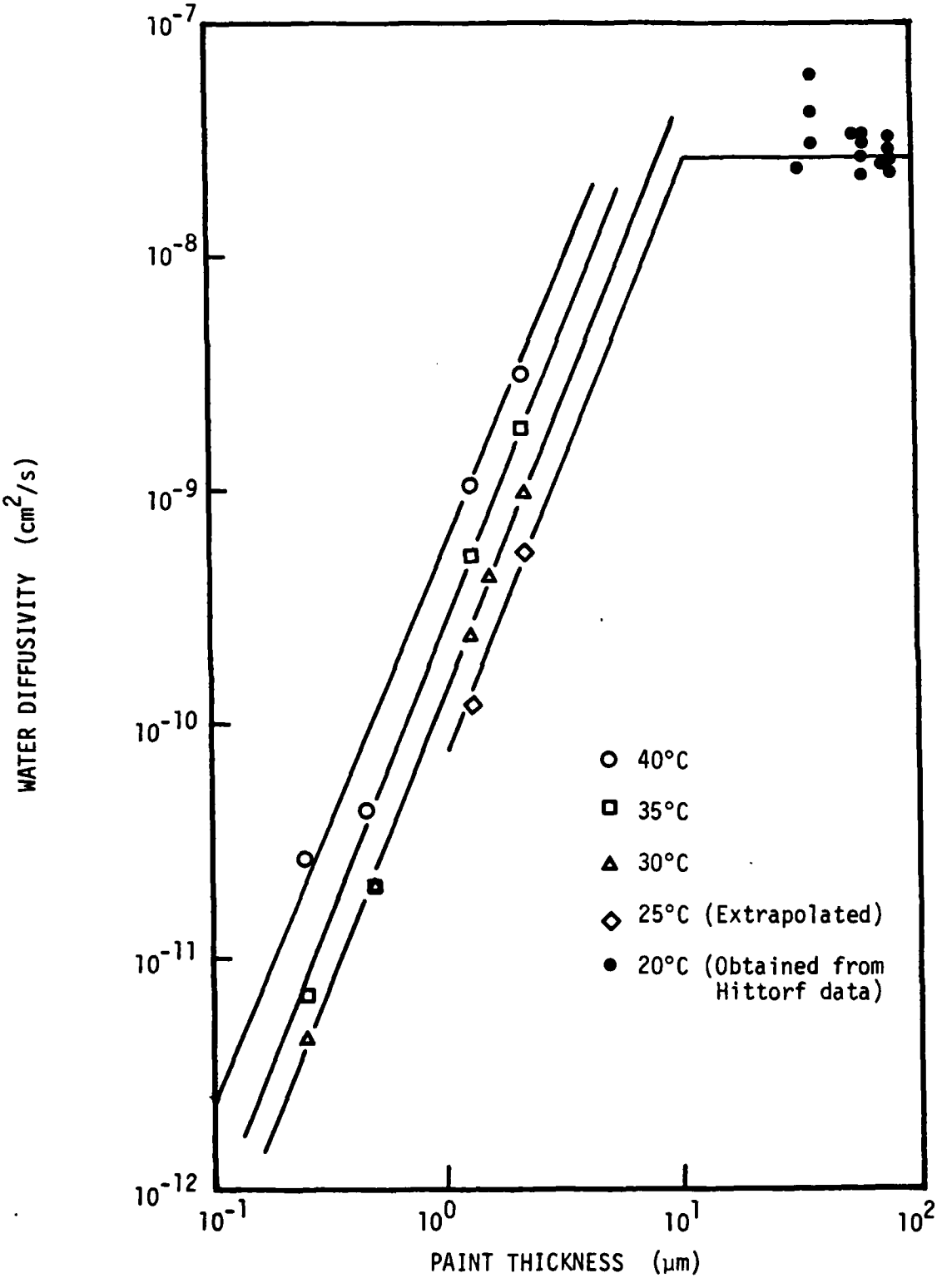

Fig. 21. Apparent diffusivity of water in O-PUR as a function of coating thickness and temperature.

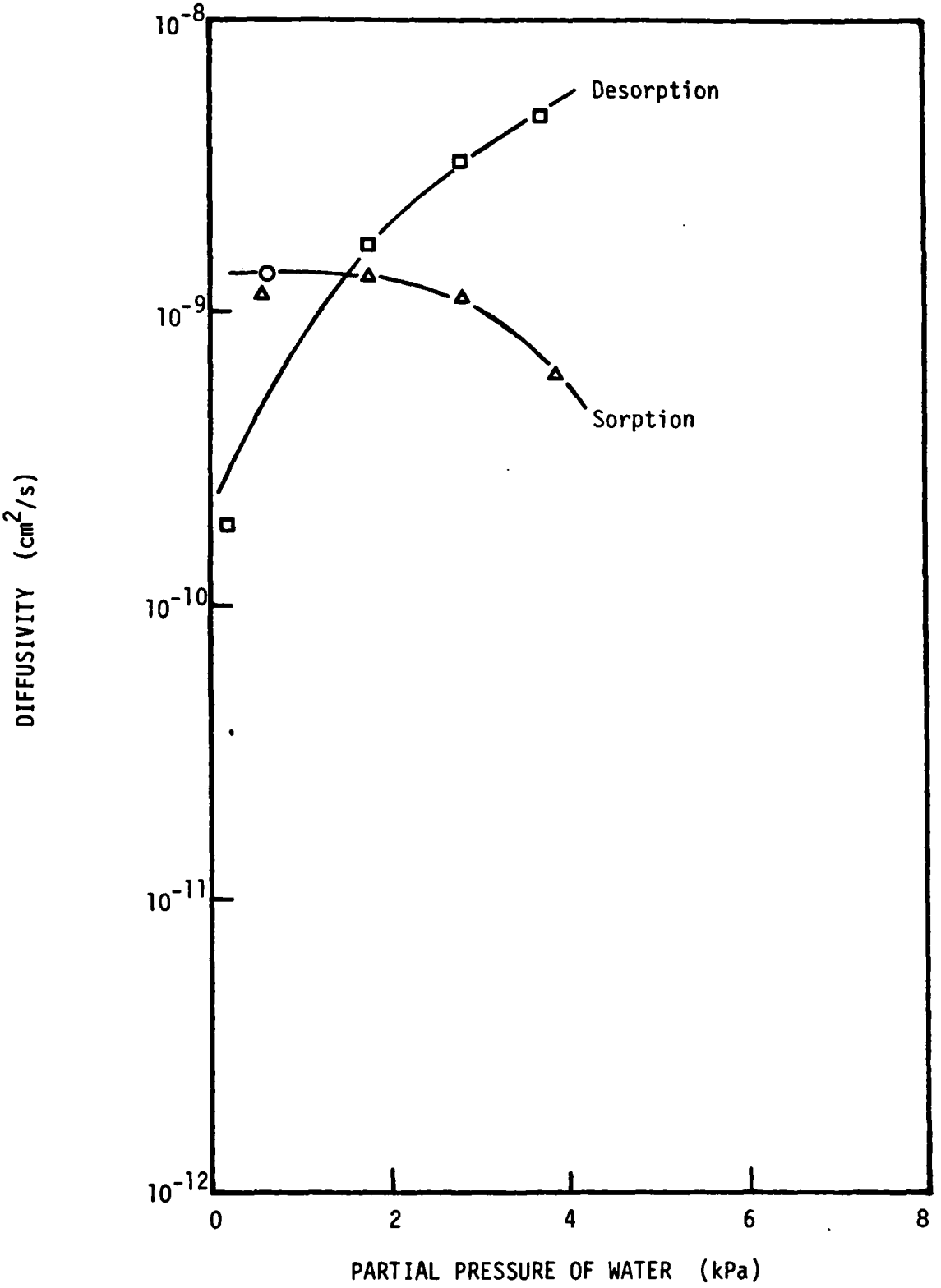

Fig. 22. Diffusivity of water on sorption and desorption in a single specimen of O-PUR.

to be much thicker than an atomic monolayer and the influence of specific paint-metal interactions could therefore be reduced.

Sodium and Chloride Solubility in Paint

A radiotracer technique was used to determine the solubility of sodium-22 and chloride-36 in a variety of paints. It was assumed that both radioactive and nonradioactive atoms of the same species were chemically equivalent, and preferential absorption was therefore absent. This assumption allowed calculation of the total sodium (for example) content of each specimen, but provided no information as to the relative concentrations of the various species containing sodium atoms. The results of the solubility experiments are given in Table 8.

Mathematical Models

The objective of the mathematical model is to quantitatively describe the transport of ions and water through paint films. A series of experiments has been performed to obtain data with which to test the model. Two models have been evaluated using these experimental data. Transport parameters independent of concentration changes and position have been assumed. The models and how they represent the data will now be considered.

Figure 5 shows a representative example of how the electrical conductivity of O PUR varies with the concentration of NaCl in the bathing solution. The experimental data are represented by the symbols. These data clearly show curvature with the sensitivity of the conductivity to changes in NaCl concentration decreasing as the concentration decreases. This fact can be taken as evidence that some change is taking place in the mechanism of ionic conduction as the salt concentration decreases. This conclusion is also supported by the data illustrated in Fig. 23. Figure 23 shows how the potential across the membrane depends on the salt concentration in the solutions adjacent to the membrane. The potential was determined with two identical silver-silver chloride electrodes. These data also show curvature, again indicating that some change is taking place in the relative mass transport rates within the paint film.

It is known that paint films exhibit the characteristics of ion exchange membranes (5), and the concentration dependence of the conductivity of ion exchange membranes is similar to that illustrated in Fig. 5. Therefore, the

Table 8

Solubility of Sodium and Chlorine Atoms in Paints Immersed in 0.1 N NaCl at 25°C

Paint	Sample	Atom Concentration (mole/g-paint) Sodium	Chloride
O PUR	A	2.2×10^{-8}	
O PUR	1	3.1×10^{-8}	
O PUR	3		1.1×10^{-7}
O PUR	4		1.6×10^{-7}
N PUR	A	1.3×10^{-8}	
N PUR	4	1.7×10^{-8}	
N PUR	5		2.1×10^{-8}
N PUR	6		2.5×10^{-8}
VR-2	A	1.8×10^{-6}	
VR-2	7	4.6×10^{-7}	
VR-2	8		2.6×10^{-6}
VR-2	9		2.9×10^{-6}
VR-3	A	1.5×10^{-6}	
VR-3	10	1.1×10^{-7}	
VR-3	11		1.1×10^{-7}
VR-3	12		1.8×10^{-8}
VR-4	A	1.0×10^{-7}	
VR-4	13	1.5×10^{-8}	
VR-4	14		1.6×10^{-8}
VR-4	15		3.9×10^{-8}

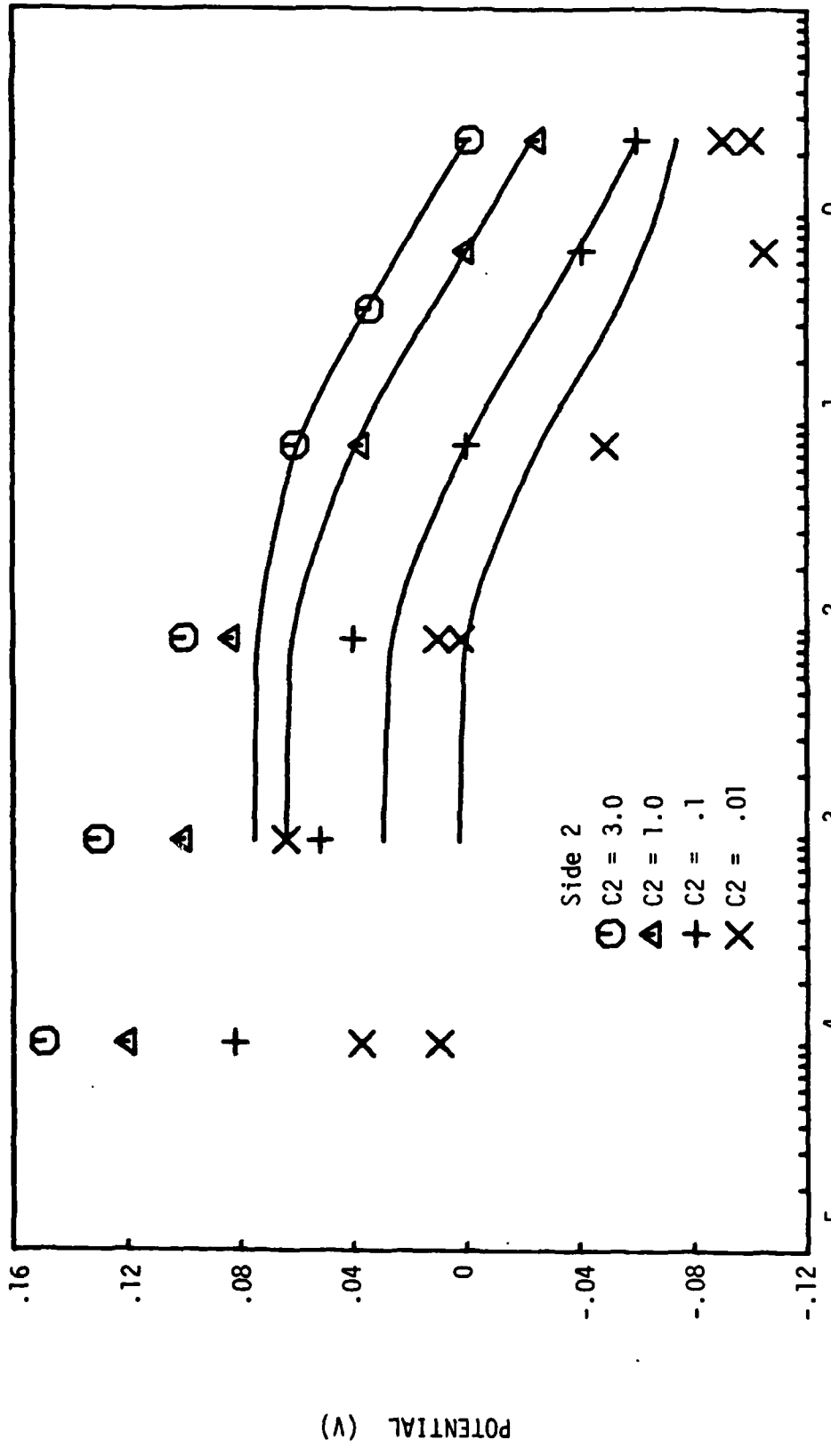

Fig. 23. Membrane potential across O-PUR. Symbols are experimental data. Curves are IE model.

first mathematical model treated paint as an ion exchange membrane. In order to include the frictional interactions exhibited by conventional ion exchange membranes, a general set of transport equations was used. These equations are similar to the Stefan-Maxwell equations and require knowledge of $\frac{1}{2}n(n-1)$ phenomenological coefficients (n = the number of mobile species transported in the paint).

A series of Hittorf experiments was initiated to obtain enough experimental data to test the ion-exchange model of paint films. A series of solubility experiments was also performed to determine the equilibrium distribution of sodium and chloride between the paint and aqueous phases. Some of the data were used to obtain the required phenomenological coefficients. Then the model was employed to predict how the conductivity and membrane potential varied with the concentration of salt in the bathing solutions. The solid curves in Figs. 23 and 24 show the model results. The model-predicted conductivity is quite close to the experimental results over the entire range of salt concentration, but the membrane potential is only modeled accurately at relatively high salt concentrations. At salt concentrations below about 10^{-2} N, Donnan exclusion prevents sodium ions from entering the paint. In this region of concentration the conductivity is relatively constant and the transference number of sodium is near zero as is the slope of each membrane-potential line. Thus this model is not capable of accurately predicting the experimental data over the entire range of salt concentration.

A second anomaly of the IE model is the fact that the transport of water is independent of the current density. In conventional ion-exchange membranes water transport is linked to the motion of the counter ions. By analogy a similar mechanism was expected for paints, provided the IE model was correct. Figure 25 shows how the radioactive activity of tritium varied with time in one Hittorf experiment in which the voltage was changed four times. The current varied by a factor of about fifteen over the course of the experiment. As Fig. 25 shows the tritium activity did not vary appreciably from the theoretical value based on Fixian diffusion through the paint. Similar behavior was observed in every other Hittorf experiment. These results clearly indicate that the coupling between water and current was negligible.

Ion-ion coupling could not be determined with the radiotracer technique employed here because sodium and chloride could not be determined simultaneously

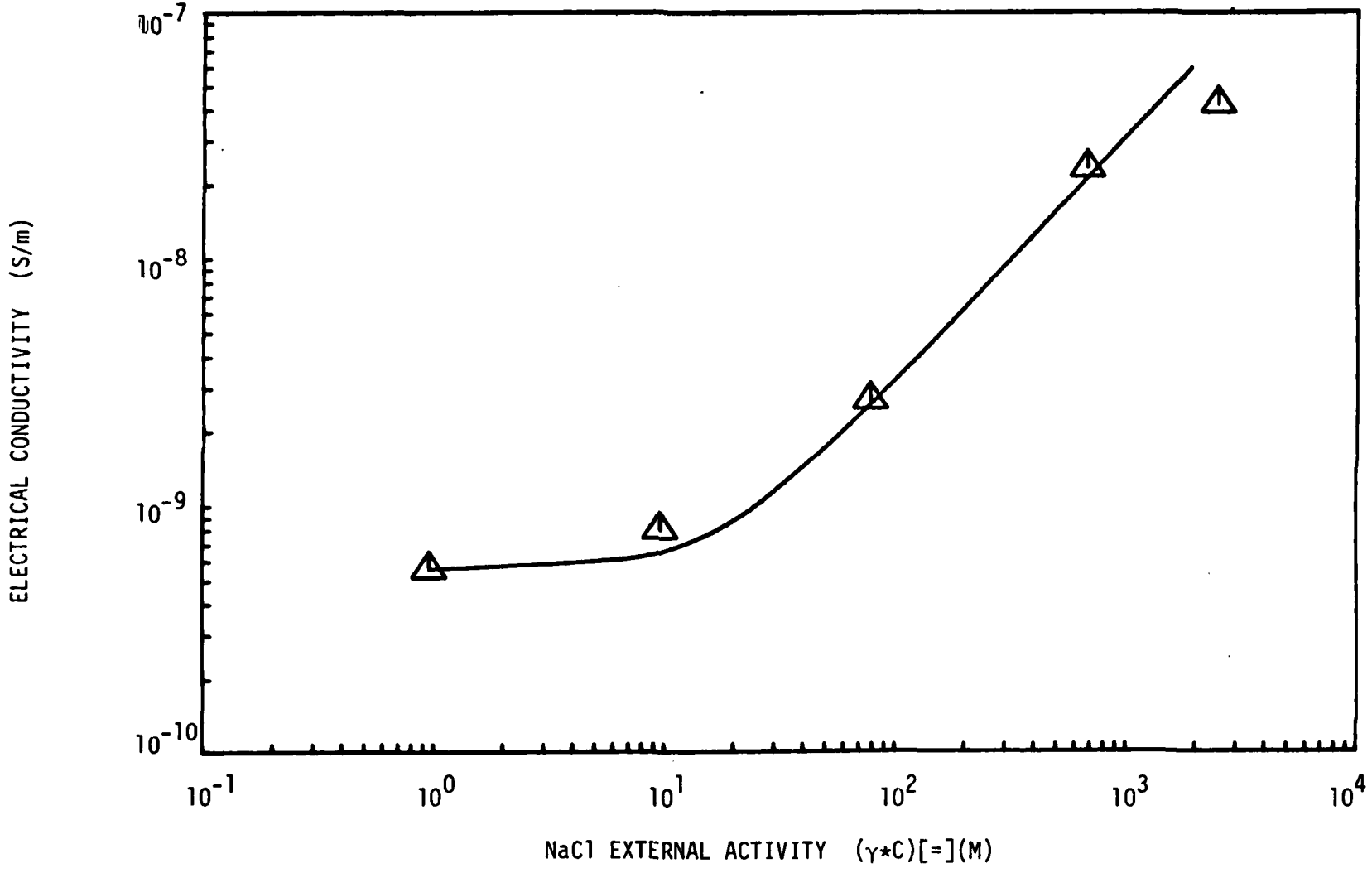

Fig. 24. Electrical conductivity of O-PUR in NaCl solution. Symbols are representative data. Curve is IE model.

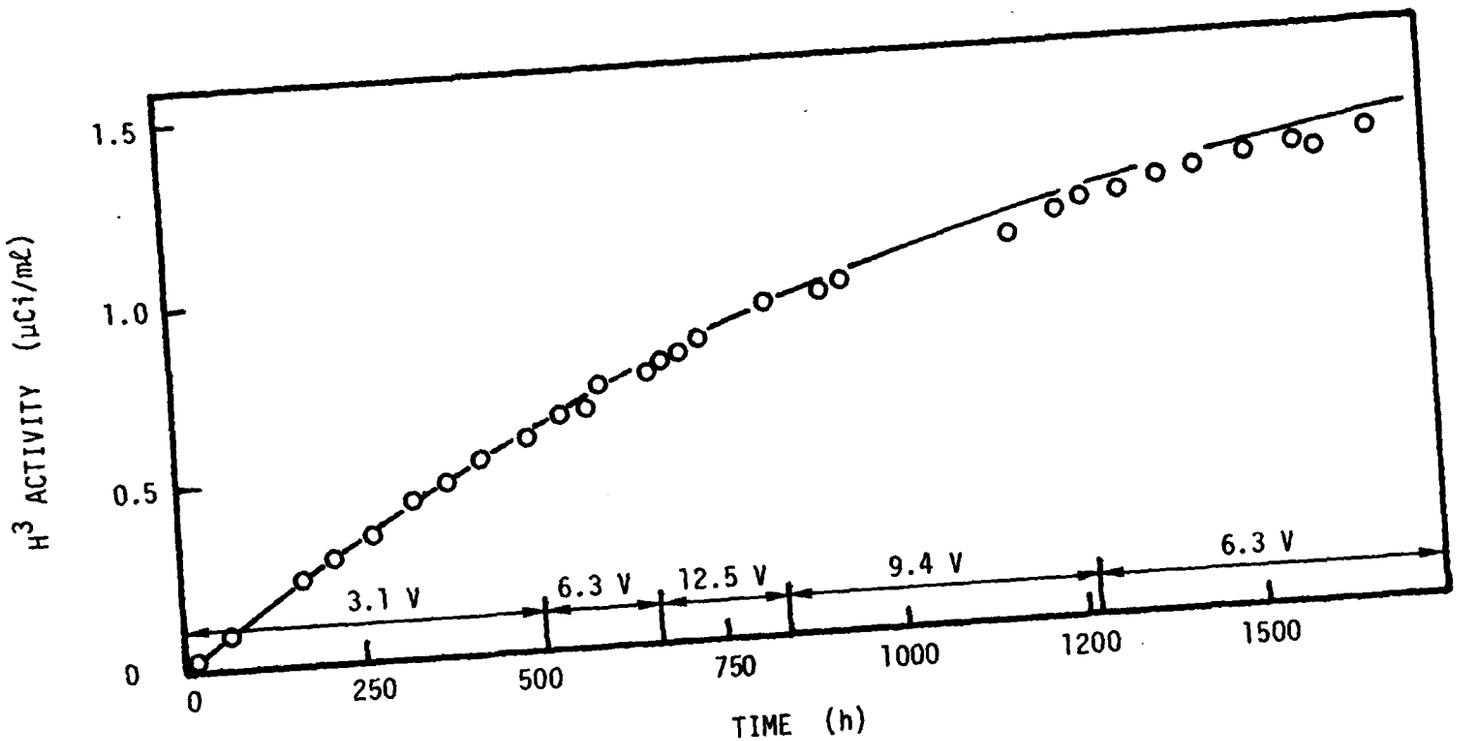

Fig. 25. Tritium activity in the top cell of a Hittorf experiment with O-PUR. Points are experimental data. Solid line is a theoretical fit of the data based on Ficksian diffusion with a constant diffusivity $D = 3.6 \times 10^{-8}$ cm^2/s.

in one experiment. However, in conventional ion-exchange membranes ion-ion coupling is generally less significant than the water-counterion coupling. Therefore, it has been concluded that coupled flows are below the limits of our experimental technique to detect in these paints. In the IE model this conclusion means that the cross phenomenological coefficients are zero.

There is another problem with the ion-exchange model of paints which came to light during the course of the Hittorf experiments. The transference numbers of both sodium and chloride, as determined by the radiotracer method, were found to sum to less than one. This means that some ion other than sodium and chloride is being transported through the paint. The present ion-exchange model is incapable of explaining this type of behavior when the paint is immersed in a solution containing only sodium chloride and water. A two-phase ion exchange membrane composed of an anion conducting phase and a cation conducting phase could explain the required behavior, but this two-phase model was not considered in this work.

Both the membrane-potential and transference number results can be interpreted as indicating that a mobile ion other than sodium or chloride is present inside the paint films. What other ions could be present? Several answers are possible. There are of course hydrogen and hydroxyl ions present in the solution. There are also small concentrations of various ionic impurities, and there may be ions resulting from breakdown of the paint. Another possibility is that the paint acts like a mixed ion exchanger with two or more types of fixed charge and preferentially absorbs some impurity ion. Any of these explanations could be occurring in paints.

The conductivity of paints immersed in dilute aqueous sodium chloride are of the same order of magnitude as the conductivity of hydrocarbon fluids. Even if the conductivity versus concentration curve is interpreted according to the IE model the pores in the membrane must be smaller than 30 to 50 Å in diameter. It is therefore unlikely that the conduction mechanism in paints involves ions passing through a few large pores or defects. This conclusion is further supported by other experimental evidence. The transference numbers of ions are not the same in the paint and in the aqueous electrolyte. Therefore some sort of strong specific interaction must be taking place between the ions and the paint. This type of interaction is only present in pores whose radius is

smaller than the Debye length. The pores must be no larger than a few tens of angstroms in diameter. Based on this picture of paints a conceptual model is proposed: the paint will be considered to be like a thin liquid hydrocarbon membrane.

One of the first matters which must be considered when dealing with the electrochemical properties of hydrocarbons is ion association (11). Even compounds exhibiting complete dissociation in aqueous solution become weak electrolytes in hydrocarbon solvents. The dielectric constant of O PUR is about 3. It is therefore expected that ion association will take place in paints.

Gemant (12) has studied ions in hydrocarbons and concluded that ionic activity coefficients may be assumed to be one. This suggests that dilute solution transport theory is applicable in hydrocarbons. In the Hittorf experiments conducted in this laboratory, no evidence of mobile species interaction was found, i.e., the phenomenological cross coefficients were negligible. It was therefore decided to use dilute solution transport equations in a new "ion association" (IA) mathematical model.

The experimental data require that an ion other than sodium or chloride be present in the paint. The concentration of this "secondary" ion must not depend directly on the concentration of sodium chloride in the bathing solution if the conductivity and membrane-potential data are to exhibit the observed curvature. Water is the most prevalent compound which meets these requirements. Therefore, the paint was considered to contain four mobile ionic species: Na^+, H^+, Cl^-, OH^-. The four ions can associate in the paint to form four additional compounds: NaCl, NaOH, HCl, and H_2O. The transport of these eight species is described by the IA model.

The mathematical model consists of four equilibrium equations, four differential equations, and the electroneutrality condition, which must be solved simultaneously. The equilibrium equations are of the form:

$$K = \frac{C_A C_C}{C_{AC}} \tag{3}$$

where C_A = anion concentration
C_C = cation concentration
C_{AC} = associated-complex concentration
K = equilibrium constant.

There are in general eight species conservation equation of the form:

$$\frac{\partial C_i}{\partial t} = D_i \nabla^2 C_i + D_i \nabla(z_i C_i \nabla\psi) + R_i \qquad (4)$$

where, from left to right, the terms represent accumulation, diffusion, migration, and generation, respectively. There are only four independent generation terms corresponding to the four ion association reactions. Elimination of the four generation terms from the eight conservation equations yields four independent differential equations of the form:

$$\frac{\partial}{\partial t}(C_i - C_j - C_k) = D_i \nabla^2 C_i - D_j \nabla^2 C_j - D_k \nabla^2 C_k + D_i \nabla(z_i C_i \nabla\psi) \qquad (5)$$

The four equations 3 plus the four equations 1 and the electroneutrality condition constitute the equations of the IA model.

In order to solve the equations, the boundary conditions must be specified. Thermodynamic equilibrium was assumed at each paint-solution interface, and the composition of both aqueous solutions was specified. Three independent distribution coefficients were specified for each paint-solution interface. The distribution coefficients together with electroneutrality and the four equilibrium conditions allowed the composition inside the paint to be calculated from the known composition of the adjacent aqueous bath. The final boundary condition was obtained by specifying either the current density or the membrane potential.

In order to use the model to predict mass transport through paint, values must be specified for eight diffusivities (D_i), four equilibrium constants (K_i), and three distribution coefficients (S_i). As a baseline case the hydrogen and hydroxyl ion diffusivities were assumed to be 10^{-7} cm^2/s, the sodium and chloride diffusivities were set at 10^{-8} cm^2/s, and the diffusivities of the remaining four compounds were set equal to 10^{-9} cm^2/s. The dissociation constants were calculated from Fuoss' theory of ion association.

$$K = \frac{1}{K_a} = \frac{4\pi N a^3 e^b}{3000}$$

a = radius of the association pair

N = Avogadro's number

$b = |z_+ z_-| e_e^2 / \epsilon kTa$

z_+ = cation relative charge

z_- = anion relative charge

e_e = charge on an electron

ϵ = dielectric constant of the solvent

k = Boltzmann constant

T = absolute temperature

Published values of the atomic and ionic radii were used (13), and the dielectric constant was set equal to three, the experimental value of 0 PUR.

The distribution coefficient for water was based on the results of the equilibrium water sorption experiments.

$$S_w = \frac{\bar{C}_w}{C_w} = 0.025 \tag{4}$$

where the bar is used to designate the concentration inside the paint. There were two other solubility parameters. One represented the solubility of associated sodium chloride in the paint.

$$S_{NaCl} = \frac{\bar{C}_{NaCl}}{A_{NaCl}} = 10^{-5} \tag{5}$$

where A_{NaCl} = the activity of sodium chloride in the aqueous solution. The other solubility parameter represented a ratio of concentrations:

$$S_R = \frac{(\bar{C}_{HCl}/A_{HCl})}{(\bar{C}_{NaOH}/A_{NaOH})} = 10^{-2} \tag{6}$$

The values of both S_{NaCl} and S_R were estimated from the experimentally determined solubilities of chloride-36 and sodium-22.

The equations were solved by an iterative technique on a digital computer. The results showed that the conductivity was about five orders of magnitude smaller than that illustrated in Fig. 5. The low conductivities appeared to result from low ion concentrations in the paint which were a consequence of the large ion association constants.

In an attempt to increase the modeled conductivity, the value of the dielectric constant was allowed to increase, and the four equilibrium constants (K_i) were recalculated accordingly. The conductivity versus concentration curve was found to be in the region of the experimental results when the dielectric constant was about seven. With the dielectric constant equal to seven the model also predicted that the sum of the sodium and chloride transference numbers would be less than one. The transference numbers varied with the salt concentration in the bathing solution, as shown in Table 9. This model also agrees qualitatively with the membrane-potential data as illustrated in Fig. 25.

Table 9

Comparison of Experimental Transference Numbers in O PUR with Values Calculated Using the IA Model

NaCl Concentration (N)	t_+		t_-	
	Calc.	Obs.	Calc.	Obs.
10^{-3}	0.50		0.27	
10^{-2}	0.50	.02	0.40	
10^{-1}	0.50	.41	0.46	0.31
1.0	0.50		0.49	0.41

The results of the model calculations show that the IE model is unable to explain in either a qualitative or quantitative manner all of the experimental results. This model can describe the conductivity data quantitatively and is in qualitative agreement with the membrane-potential data, but it cannot even qualitatively explain why the sodium and chloride transference numbers do not sum to unity. The IA model is also unable to explain the data unless the dielectric constant is raised to seven. The experimental dielectric constant is only three. The effective dielectric constant might be greater than the experimental value if polar compounds were attracted to polar regions in the paint. The polar regions could be formed when the paint was wet and as the cross linking reaction proceeds the separate regions of paint become rigid. When the paint is immersed in aqueous electrolyte, the water and salts favor the polar regions further increasing the dielectric constant there.

If we accept that a local dielectric constant of seven is reasonble, the IA model can successfully explain the experimental results in a qualitative way. Only limited attempts have been made to establish quantitative agreement with the data, and the ultimate agreement would certainly be better than that illustrated in Fig. 25. Nevertheless it appears that only qualitative agreement with the data could ever be obtained. The calculations show that the sodium transference number is nearly constant when the salt concentration changes from 10^{-3} N to 1.0 N (Table 6). The chloride and hydroxide ions transport the bulk of the remaining current, and the transference numbers of both these ions vary significantly in this concentration range. This behavior results from the relative values of the equilibrium constants used in the model and can ultimately be traced back to the ionic radii of the four associated species in the paint. The radii are independent of the type of solvent (paint) or any other parameter in the model. The equilibrium constants do depend on the dielectric constant of the paint, but each equilibrium constant is affected in approximately the same manner. Therefore, it is unlikely that the sodium transference number can be made more concentration dependent than the transference number of chloride unless additional features are incorporated into the IA model.

It is clear from the results of these calculations that the IA model must be modified in some way. The primary shortcoming of the model appears to be neglect of specific interaction within the paint. The exact nature of this interaction is difficult to assess. The ion exchange model is dominated by specific interaction, but it is still unable to explain the observed behavior. We have used accepted concepts of ion association to argue that sodium chloride should be present as a neutral complex in paints. It is possible therefore that the ion exchange model should also be modified to account for weak acid or weak base phenomena.

It is also possible that the Fuoss theory is not applicable to paints. The Fuoss theory specifically neglects ion-solvent interactions. Furthermore Gemant (12) indicates that the addition of a small quantity of a phenolic compound to a hydrocarbon oil containing aliphatic acid-ammonium complexes dramatically increases the conductivity. Gemant attributes the increase to solvation effects of the phenolic compound. The Fuoss theory does not consider this type of behavior.

It is known that many polymers contain local regions with properties different from the bulk. Nafion and polymethacrylic acid are known to form polar clusters for example. It is to be expected that paints will exhibit similar behavior although probably to a lesser extent. When water enters the paint it will accumulate preferentially in the regions of high dielectric constant. This is a form of specific interaction not accounted for in the model or Fuoss' theory which assumes a solvent of uniform dielectric constant. If the water is also involved in other interactions, hydrogen bonding for example, the model will be even more inadequate.

CONCLUSIONS

A study was conducted to determine the mass transport properties of paints. Diffusion and migration fluxes of sodium and chloride ions and water were experimentally determined and quantitatively modeled. Eight unpigmented paints including two polyurethanes, three vinyl resins and three epoxies were examined. All the paints meet current Navy Military Specifications. This work is the most systematic and complete study of the transport properties of paints reported to date. The following conclusions are based on this study.

1. Transference numbers, permeability coefficients, diffusivities, and solubilities of sodium ions, chloride ions, and water have been determined experimentally, and the results are tabulated in the text. These transport properties are the basis of the mathematical models discussed in the text and can be used in future analyses to help determine the mechanism of corrosion under paints.

2. A number of interesting anomalies in the transport properties of paints were found in this study. The transport of sodium and chloride ions was determined for paints immersed in aqueous sodium chloride solution. Migration of sodium and chloride ions cannot account for all the current flowing through the paint. This result was observed in four of the five paints which could be tested. Clearly, some unknown ion is carrying some of the current. Repeated attempts were made to determine if hydrogen or hydroxyl ions carry current, but these attempts were unsuccessful. The water solubility and diffusivity were measured and found to vary with paint thickness. This observation was interpreted as evidence of a two-phase paint film.

3. Two quantitative models were evaluated by comparison with the extensive data obtained from one of the polyurethane paints. The first model, derived prior to the present contract, treated the paint as a homogeneous ion-exchange membrane and employed general phenomenological transport equations. This model could not explain the observation that sodium and chloride carry less than all the current. Analysis of the experimental data showed that the phenomenological cross terms were negligible, and a new model was formulated which employed dilute solution equations instead of the more complex phenomenological equations. This second model, formulated during this contract, included the effects of ionic association between anions and cations in paints with low dielectric constants. This model could account for the transport of ions other than sodium and chloride but only when a dielectric constant more than twice the bulk value measured for the paint was used. This result suggests inhomogeniety in the paint film. A good framework for quantitative analysis of mass transport in paints has been developed, but further conceptual work is necessary before complete agreement between model and experiment can be achieved. When agreement has been reached, a relationship may be found between the transport

properties, chemical composition, structure, and service performance of paints.

4. An extensive review and analysis of filiform corrosion was completed during this contract, and a reprint of the published paper is given in the appendix.

REFERENCES

1. Annual Progress Report No. 1, Contract No. N00014-79-C-0021, Naval Ocean Research and Development Activity, Bay St. Louis, MS, 1979.

2. Annual Progress Report No. 2, Contract No. N00014-79-C-0021, Naval Ocean Research and Development Activity, Bay St. Louis, MS, 1980.

3. Final Report, Contract No. N00014-79-C-0021, Naval Ocean Research and Development Activity, Bay St. Louis, MS 1981.

4. J. Crank and G. S. Park, Eds., Diffusion in Polymers, Academic Press, N.Y., 1968.

5. J.E.O. Mayne, Anti-Corros., p 3, Oct. 1973.

6. R. T. Ruggeri and T. R. Beck, "A Model for Mass Transport in Paint Films," Corrosion Control by Coatings, H. Leidheiser, Ed., Science Press, Princeton, N.J., 1979, p 455.

7. J. S. Newman, Electrochemical Systems, Prentice-Hall, Englewood Cliffs, N.J., 1973.

8. C. S. Lu and O. Lewis, J. Appl. Phys., 43, 4385 (1972).

9. J. Crank, The Mathematics of Diffusion, 2nd ed., Clarendon Press, Oxford, 1975.

10. P. N. Pintauro, Mass Transfer of Electrolytes in Membranes, PhD Dissertation, Univ. of Calif., Los Angeles, 1980.

11. R. A. Robinson and R. H. Stokes, Electrolyte Solutions, 2nd ed., Butterworths, London, 1959.

12. A. Gemant, Ions in Hydrocarbons, Interscience Pub., N.Y., 1962.

13. B. E. Conway, Ionic Hydration in Chemistry and Biophysics, Elsevier Scientific Pub. Co., N.Y., 1981.

APPENDIX A

Crystal Oscillator Experiments

Quartz crystals have been used to construct highly stable oscillators for many years. The crystal is a low-loss piezoelectric resonator which controls the oscillator's frequency. The fundamental frequency of a crystal is affected by temperature and several other environmental factors; however, the physical properties of the crystal have the greatest effect on the frequency.

The mass of the crystal is one property which has a great influence on frequency. This fact is the basis of several unusual uses of crystal oscillators, including sorption detectors (A1,A2). Highly sensitive sorption detectors have been constructed by coating a quartz crystal with a thin layer of absorbant (paint). The frequency of this "composite" crystal changes as its mass varies. By knowing the relationship between frequency change and mass change, microbalance weighing can be performed. Sensitivities on the order of 10^{-12} g have been estimated (A1).

The piezoelectric oscillation of a quartz crystal has been analyzed as an acoustic resonator (A3). In this one-dimensional theory, a wave disturbance is introduced at one surface of the crystal. The wave travels through the quartz with a constant velocity and attenuation until it reaches the opposite edge of the crystal. At the edge, the wave is completely reflected. This model is mathematically equivalent to an ideal transmission line with distributed loss, and a complete mathematical description is available.

When a quartz crystal is coated with another substance, a composite is formed. The acoustic resonator theory has been used to describe these composite resonators, but the analysis is more complicated than for the simple resonator. The complexity results from partial reflection of the traveling wave at the boundary between the quartz and the coating substance. Despite the complexity, Miller and Bolef (A3, A4) obtained an exact solution of the composite resonator. The theory showed that the only major effect of attaching the coating to the crystal was to shift the resonant frequency of the composite resonator (f) relative to the frequency of the simple quartz crystal (f_q).

Miller and Bolef's acoustic resonator theory is based on several approximations and assumptions. The assumptions appear to be appropriate, although they have apparently not been individually checked. However, the applicability of the entire theory to metal-coated crystals was proposed by Miller and Bolef (A4), and Lu and Lewis (A5) checked this application using three metals: copper, silver, and lead. The theory is in good agreement with experimental data for frequency shifts up to 15% of the "unloaded-crystal" frequency (f_q).

The acoustic resonance theory is based on the following assumptions (In the composite resonator the assumptions apply to the crystal and the coating separately.):

1. The system is one dimensional.
2. End faces are flat and parallel.
3. The wave travels with a constant velocity.
4. The attenuation per unit distance is constant.
5. The density of the medium is constant.
6. The crystal is oscillating at steady state (cw).
7. The coating is uniform over the entire "active" area.

   This theory does not treat the effects of crystal mounting or surface nonuniformities.

Lu and Lewis (A5) present three relations between the mass change of the composite crystal and the observed frequency shift. The most accurate equation, "exact solution," is based on Miller and Bolef's result (A3, Eq.9) with no losses in either the quartz or the coating. The exact equation is:

$$\tan\left[Z\pi \frac{f}{f_q} \frac{m_f}{m_q}\right] = Z \tan\left[\pi \frac{f_q - f}{f_q}\right] \quad \text{(A1)}$$

where Z = the ratio of the shear-mode acoustic impedance of quartz to that of the coating

f = the frequency of the composite resonator

f_q = the frequency of the uncoated quartz crystal

m_f = the mass of the coating (film)

m_q = the mass of the uncoated quartz crystal

In this instance the composite-resonator frequency (f) depends on the acoustic impedance ratio (Z) as well as the mass of the applied coating (m_f).

The second equation presented by Lu and Lewis is the "period approximation." When Z = 1, or when $(m_f/m_q) \ll 1$, Eq. A1 simplifies to

$$\frac{m_f}{m_q} = \frac{f_q - f}{f} \quad \text{(A2)}$$

The period approximation is adequate ($1<Z<2.29$) for frequency deviations less that about 5% (A5).

Also, when m_f/m_q is small, f has nearly the same value as f_q. Under these conditions Eq.A1 simplifies to the "frequency approximation,"

$$\frac{m_f}{m_q} = \frac{f_q - f}{f_q} \quad \text{(A3)}$$

The frequency approximation is limited to a deviation of about 2% (A5)[1]. Once a particular quartz crystal has been selected, m_q and f_q are fixed. Then, f depends only on the mass of the applied coating. Eqs. A2 and A3 show this statement is true for both approximate models, but Eq. A2 is nonlinear.

---

[1] The total frequency change produced by the coating and absorption of water was less than 2% in all current experiments.

The theory of sorption and desorption in thin sheets has been thoroughly discussed by Crank (A6). The basic equation describing the process is:

$$\frac{\partial c}{\partial t} = - \frac{\partial N}{\partial x} \tag{A4}$$

where c = the diffusant concentration (mol/m^3)

N = the diffusant flux ($mol/m^2 \cdot s$)

t = the time (s)

x = the linear dimension (m)

If the flux obeys Fick's first law,

$$N = - D \frac{\partial c}{\partial x} \tag{A5}$$

where D = the diffusivity (m^2/s)

Eq. A5 can be substituted into Eq. A4 to yield:

$$\frac{\partial c}{\partial t} = \frac{\partial}{\partial x} \left[D \frac{\partial c}{\partial x} \right] \tag{A6}$$

This is the basic equation of diffusion in a thin sheet and is equivalent to Fick's second law if the diffusivity is constant:

$$\frac{\partial c}{\partial t} = D \frac{\partial^2 c}{\partial x^2} \tag{A7}$$

In general the concentration depends on time, position, and the diffusivity, as well as the boundary conditions of a particular problem. Solutions of Eqs. A6 and A7 have been given for a variety of boundary conditions and diffusivities (A6, A7). Most of the published solutions require knowledge of the functional form of the diffusivity, but Crank and Park (A8) and Crank (A6) discuss practical ways of using the theory to evaluate the diffusivity from sorption and desorption isotherms.

One set of boundary conditions for which an analytical solution of Eq.A7 is available is:

$$\frac{\partial c}{\partial x} = 0 \quad @\ x = 0,\ t>0 \tag{A8}$$

$$c = 0 \quad @\ 0 \leq x \leq \ell,\ t = 0$$

$$c = c_1 \quad @\ x = \ell,\ t>0$$

These boundary conditions represent a step change in surface concentration, at $x = \ell$, at time zero. For these conditions, the diffusivity is easily determined by plotting the dimensionless uptake of sorbate (R_w) versus the square root of time.

$$R_w = M_t/M_\infty \tag{A9}$$

where M_t = the total amount of sorbate present at time t

M_∞ = the total amount sorbed at long times (equilibrium).

$$M_t = \int_0^\ell c(x,t)dx \tag{A10}$$

This theory is equally applicable to desorption provided M_t and M_∞ represent quantities of diffusant lost.

At t = 0

$$\frac{dR_w}{d\sqrt{t}} = \frac{4}{\ell}\sqrt{\frac{D}{\pi}} \tag{A11}$$

The slope, $dR_w/d\sqrt{t}$, is nearly constant for $R_w<0.5$ (A8, p16).

It is also easy to calculate the diffusivity at long time, provided an accurate value of M_∞ is known. At long times

$$\frac{d}{dt}\left[\ln\left(1-\frac{M_t}{M_\infty}\right)\right] = \frac{-D\pi^2}{\ell} \tag{A12}$$

If both Eqs.A11 and A12 are applied to a single sorpiton experiment, a single value of the diffusivity should be obtained. If this is not found, the diffusivity is not a constant.

Appendix B

Formulation of Known-Composition Paints

Two consultants with long-time experience in polymers and paints, Dr. H. A. Newey and Mr. C. J. Busso, provided formulations of known compositions of vinyl, epoxy, and polyurethane paint systems meeting appropriate military specifications. During preparation of the initial proposal (1), it was determined by contacts with paint formulators and raw materials suppliers that the paint industry is extremely competitive and that the only way to obtain known-composition paints was through consultants. Appropriate Military Specification numbers for paints used by the Navy were obtained from NSRDC at Annapolis (2).

The paint systems procured (3, 4) are given in the following subsections. The code name given each paint for internal use at ETC is given in parentheses by each paint.

System I, Epoxy Resin Coating that Meets MIL-P-24441 (E Epoxy)

This coating consists of an epoxy resin, Shell EPON 815, and a polyamide curing agent. The epoxy resin is a mixture of the diglycidyl ether of bisphenyl A (90% by weight) and butyl glycidyl ether (10% by weight). The curing agent is a more-complex amine mixture, mainly Versamid 280B75 plus Genamid 2000 and MEK solvent (formulas given). In curing the amine, hydrogens add to the epoxide groups in the epoxy resin by the reaction:

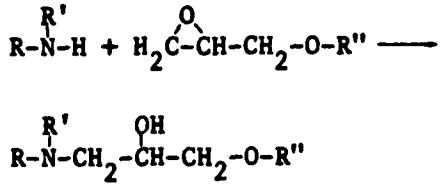

The epoxy group reacts with both amine hydrogen on the terminal primary amine groups. The polyfunctional amines, Versamid 280 and Genamid 2000, react by this simple addition reaction with EPON 815 to give a cross-linked thermoset film.

System II, MIL-P-15328D, Formula 117 (VR2)

The structure of Bakelite Vinyl Butyral Resin XYHL can be best described by telling how it is made. Vinyl acetate is polymerized to a linear polymer and then saponified to remove most of the acetate groups leaving hydroxyl groups. Part of these hydroxyl groups is reacted with butyraldehyde, which forms an acetal with adjacent hydroxyl groups. The final product may be represented by the following structure:

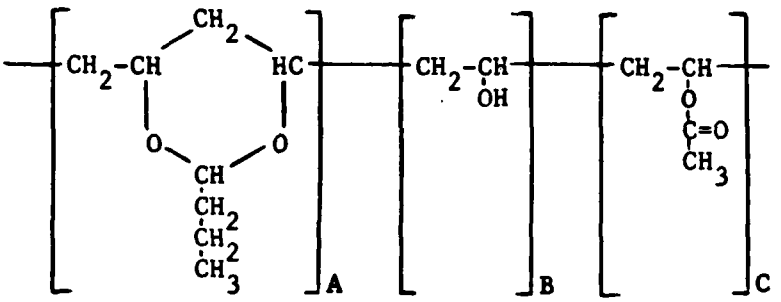

Units of A, B, and C are randomly distributed along the molecular chain. In Bakeline XYHL there is approximately 80% by weight A, 19.5% by weight B, and 0.5% by weight C. The molecular weight is about 30,000.

System III, MIL-P-15929C, Formula 119 (VR3)

Bakelite vinyl resin VAGH is a copolymer of vinyl chloride and vinyl acetate where a fraction of the acetate groups have been saponified to hydroxyl groups. It can thus be described as a copolymer of vinyl chloride, vinyl acetate, and vinyl alcohol, and can be represented by the formula:

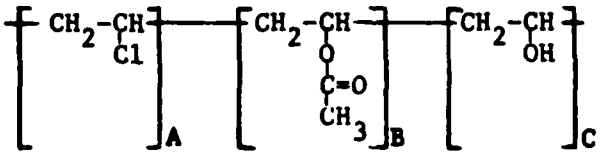

These units are randomly distributed along the molecular chain. Bakelite VAGH is 91% by weight A, 3% by weight B, and 6% by weight C. The average molecular weight is 23,100 and it has a glass transition temperature of 79°C.

Tricresyl phosphate is a plasticizer for the resin. It has the structure:

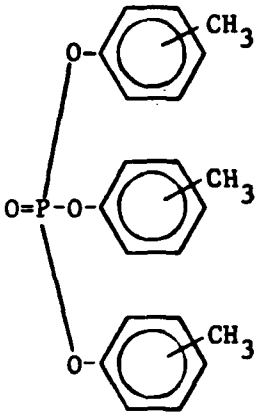

It does not react chemically but only dissolves in the vinyl resin.

System IV, MIL-P-15931, Formula 121 (VR4)

Bakelite Vinyl Resin VYHH is a random linear copolymer of vinyl chloride (86% by weight) and vinyl acetate (14% by weight). Again, tricresyl phosphate is the plasticizer. The rosin in the formula is largely abietic acid with other related compounds. Abietic acid has the following structure:

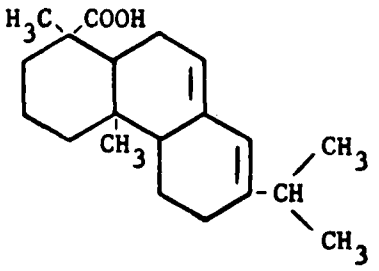

The rosin contributes to the hardness of the coating and helps adhesion. The coating dries by the evaporation of the solvent and no chemical reaction takes place between the components.

System V, EPONOL Resin Coating (A Epoxy)

EPONOL 55 is a thermoplastic resin related to epoxy resin. The structure of the repeating unit is generally represented by the formula:

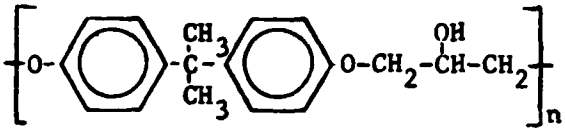

where n is about 25. There is some branching of the chain and the end groups are probably phenol or alcohol groups. While the chemical structure is similar to the epoxy resins, the molecular weight is high enough that good films are formed merely by evaporation of the solvent without the need of a curing agent.

System VI, Ketimine-Epoxy Coating (K Epoxy)

To explain the chemical composition of this coating we must first explain what a ketimine curing agent is, and how it works. The ketimine H-2 is formed from ethylenediamine and methyl isobutyl ketone by the splitting out of water as follows:

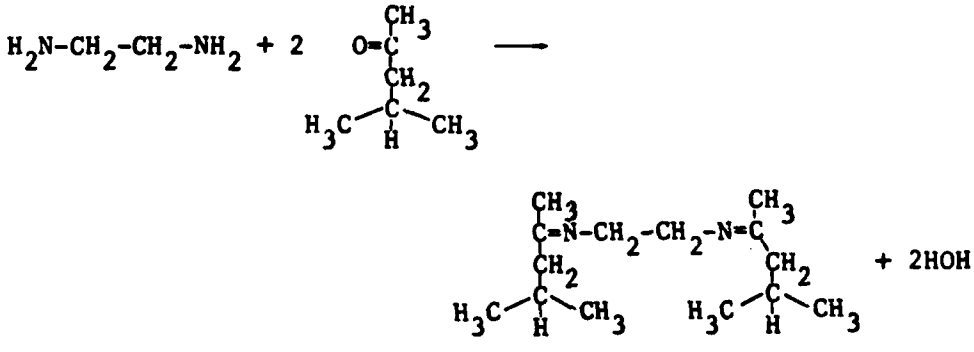

Ketimine H-2

When applied in a coating, this ketimine readily reacts with the moisture of the air which breaks it back to ethylenediamine and methyl isobutyl ketone. (The reverse of the above equation.) The methyl isobutyl ketone evaporates from the coating and the ethylenediamine is the real curing agent. Ethylenediamine cures epoxy resins by a simple, clean-cut addition

of the amine hydrogen to the epoxide groups. This reaction is shown in the following equation using a monoepoxide for illustrative purposes:

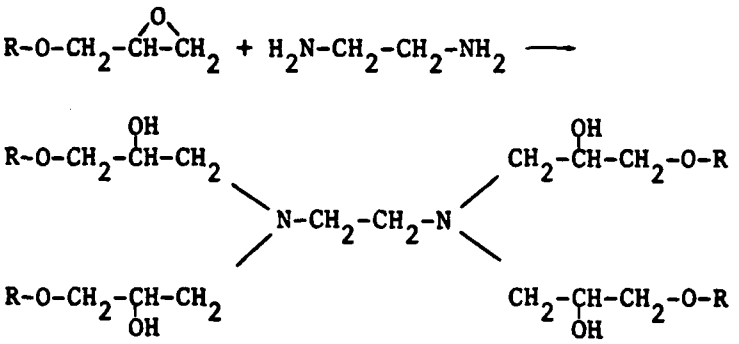

Since in the actual coating the epoxy resin is close to difunctional and the ethylenediamine is tetrafunctional, the addition reaction gives a cross-linked system with well-defined structure.

The epoxy resin in this coating consists of two parts. It is mainly the diglycidyl ether of bisphenol A.

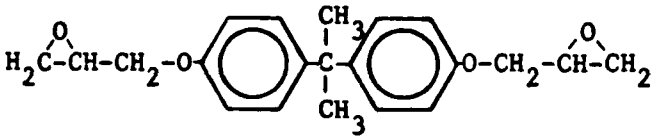

To lower the viscosity and cut down the cross-link density, this diglycidyl ether of bisphenol A is diluted with a minor amount (about 10%) of a monofunctional epoxy compound, butyl glycidyl ether.

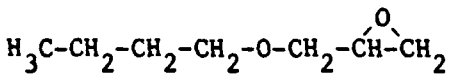

The phenol in the formula is merely present as a catalyst to speed up the reaction between amine hydrogens and epoxy groups.

System VII, MIL-C-81773B A/S (N PUR)

This is a two part coating. Part I is a solution of polyester resin having free hydroxyl groups. A typical product of this type would be

prepared by reacting a glycol, phthalic anhydride and a triol to yield the following resin structure:

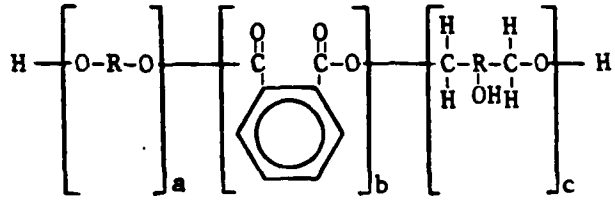

Component II is a solution of Desmodur N. This is a biuret derived from hexamethylene diisocyanate:

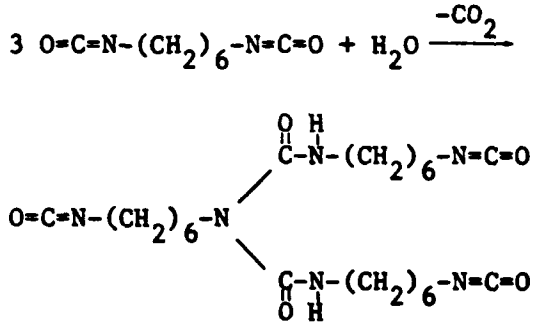

Desmodur N is sold by Mobay Chemical as a 75% solids solution in 1/1 by volume ethylglycol acetate/xylene solvent; designation of the solution is Desmodur N-75.

Cross-linking these systems results from the isocyanate-hydroxyl reaction to produce a urethane linkage:

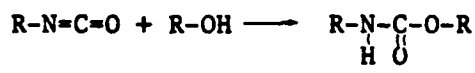

Stoichiometry for this system is 1:1, Component I:Component II, by volume. Films of these coatings should be fully cured after eight hours at 77°F.

All of the components for the seven paints were procured and free films of all were made by spraying on decal paper and stripping in water. To date only unpigmented films have been made.

In addition to these systems, some testing was done on two airplane paint systems studied on another contract. These were both commercially

important, modern, two-part polymer systems, without pigments, obtained from the Boeing Commercial Airplane Company, Kent, Washington. One was a polyurethane, Desoto, Inc., Chemical Coatings Div., Berkeley, California, meeting Boeing material specification BMS-10-60D-TYII and Mil C-83286. The code name given to this system was System VIII or O PUR. The other paint was an epoxy, Koppers Co., Andrew Brown Div., Kent, Washington and was given the code name System IX or O epoxy. No information was obtainable on the exact formulations of these systems.

A clear methacrylate paint in a spray can was used in some of the adhesion tests described in Section 3.5 to check with literature data obtained with the hesiometer on methacrylate systems.

REFERENCES (Appendix B)

1. Electrochemical Technology Corp., proposal 7803, "Determination of the Effect of Composition, Structure, and Electrochemical Mass Transport Properties on Adhesion and Corrosion Inhibition of Paint Films," April 1978.

2. T. R. Beck, Telephone call to H. Preiser, NASRD, Annapolis, MD, February 23, 1978.

3. Letter, Newey & Busso Associates, to Electrochemical Technology Corp., December 11, 1978.

4. Ibid, January 29, 1979.

Table B1

Paint Formulations

Paint	Component	Weight %	Paint	Component	Weight %
VR 2 (Part A)	XYHL vinyl resin	10.3	VR 2 (Part B)	Phosphoric acid (85%)	18.5
	n-butyl alcohol	23.1		H_2O	16.7
	Isopropyl alcohol	64.1		Isopropyl alcohol	64.8
	H_2O	2.5			
VR 2	Part A	78.4	VR 2 Solvent	Isopropyl alcohol	80.0
	Part B	21.6		n-butyl alcohol	20.0
VR 3	VAGH vinyl resin	22.2	VR 3 Solvent	Methyl isobutyl ketone	51.8
	Tricresyl phosphate	2.3		Toluene	48.2
	Methyl isobutyl ketone	39.1			
	Toluene	36.4			
VR 4	VYHH vinyl resin	12.3	VR 4 Solvent	Methyl isobutyl ketone	60.4
	Gum rosin	12.2		Xylenes	39.6
	Tricresyl phosphate	4.7			
	Methyl isobutyl ketone	42.7			
	Xylenes	28.0			
E Epoxy (Part A)	Genamide 2000	3.3	E Epoxy (Part B)	Epon 815	73.2
	Versamid 280-B-75	54.0		Super Hi-flash Naphtha	26.8
	Butyl alcohol	42.3			
A Epoxy	Eponol 55-B-40	22.2	K Epoxy	Epon 815	73.5
	Acetone	20.1		Phenol	2.2
	Toluene	33.3		Ethanol	2.2
	Methyl ethyl ketone	6.6		Epon curing agent H-2	22.1
	Methyl isobutyl corbinol	8.9			
	Cellosolve acetate	8.9			
Solvent for N PUR and O PUR	Methyl ethyl ketone	27.0			
	n-butyl acetate	9.9			
	2-ethoxyethyl acetate	43.7			
	Toluene	11.6			
	Xylene	7.8			

Table B2

Sources for Paint Resins

Paint	Resin	Source
E Epoxy	Versamid 280-B-75 (Azamide 680-B-75)	AZS Corp., A.Z. Products Co. PO Box 67, Easton Park, FL 33840
	Genamide 2000	General Mills Chemicals, Inc. Repackaged by E.V. Roberts & Assoc., Div. Evra, Inc., 8500 Steller Dr., Culver City, CA 90230
	Shell Epon Resin 815	E. V. Roberts & Assoc.
VR 2	XYHL Blend 43861	Union Carbide Corp. 270 Park Ave., New York, NY 10017
VR 3	VAGH Blend 4479	Union Carbide Corp.
VR 4	VYHH Blend B-7591	Union Carbide Corp.
	WW Gum Rosin	FRP Co., PO Box 349, Baxley, GA 31513
A Epoxy	Shell Eponol Resin 55-B-40	Shell Chemical Co., Div. Shell Oil Co., Houston, TX
K Epoxy	Shell Epon Resin 815	E. V. Roberts & Assoc.
	Shell Epon Curing Agent H-2	E. V. Roberts & Assoc.
N PUR	Part A and Part B	Deft Chemical Coatings Irvine, CA 92714
O PUR	Part A and Part B	Desoto, Inc., Chemical Coatings Div., Berkeley, CA

APPENDIX C

An Analysis of Mass Transfer in Filiform Corrosion*

ROBERT T. RUGGERI and THEODORE R. BECK*

Abstract

Filiform corrosion occurs on painted metals and cannot be prevented by conventional corrosion inhibitors. In order to better understand the corrosion phenomena, the literature was reviewed and the characteristics exhibited by filiform corrosion on different metals were cataloged. Calculations were performed to select corrosion mechanisms that were compatible with these characteristics. The preferred mechanism, compatible with all the primary characteristics, is that oxygen and water reach the corrosion site by diffusing through the porous filiform tail. Experiments were conducted which confirmed this mechanism. The mass transfer occurring inside the active corrosion cell, and unresolved questions concerning the speed and width of filiform growth are also discussed.

Introduction

Filamentary corrosion has been known for at least 60 years,[1,2] but the particular manifestation called filiform corrosion was first accurately described by Sharman[3] in 1944. Filiform corrosion (FC) is an active corrosion cell which moves across a metal surface underneath coatings and leaves an inert tail filled with corrosion products. Filiform corrosion has been observed under many different types of coatings. Van Loo, *et al.*,[4] have reported this type of corrosion on iron under several kinds of paint and under metal coatings such as tinplate, silverplate, and goldplate. Filiform corrosion on nickel plated iron has been described by Hargreaves.[5]

Filiform corrosion occurs on steel, aluminum, and magnesium. It can be retarded but not stopped by adding inhibiting pigments to paints or by using inhibitive primers.[4,6,7] Filiform tracks have a distinct worm-like appearance and have thus been of considerable concern to the food packaging industry. Early investigators established a link between filiform corrosion and relative humidity (RH). On iron, the tracks cease growing at relative humidities below about 60%.[4] Reduced humidity is still the only practical way of eliminating this type of corrosion. There are many instances where controlling the humidity is not practical, however, and a continued interest in filiform corrosion can be traced through the literature to the present.

Despite the interest in filiform corrosion, little is understood about the actual corrosion mechanism. Several mechanisms have been discussed in the literature, but even some recent proposals fail to explain certain important features of filiform corrosion. The mechanism which best explains the major characteristics of filiform was proposed by Kaesche.[8] He concluded that oxygen diffused through the tail, and the oxygen concentration at the base of the active corrosion cell was near that in the ambient atmosphere. It is the intent of the present paper to summarize the quantitative data from the literature on filiform corrosion, present a current explanation of this phenomenon, and clearly identify those aspects of the filiform mechanism which are still unexplained. Quantitative analysis of proposed mechanisms are compared with calculations based on data from the literature, and new experimental data are presented which support Kaesche's reaction mechanism.

When Sharman[3] first described filiform corrosion, he discussed the "growth of hair-like corrosion tracks known as 'underfilm corrosion.'" Sharman produced tracks for laboratory study by cutting through lacquer coatings on steel plates. He initiated filiform growth by exposing these scratched plates to acetic acid vapor for 24 hours. Thereafter, the plates were exposed only to a humid air atmosphere. Filiform tracks began growing at the scratch and proceeded outward. These tracks represent one type of filamentary corrosion that begins at a defect in the coating where the metal substrate is exposed to air. Other forms of filamentary corrosion are sometimes described as filiform, for example, filamentary corrosion on bare steel,[5,9] and a type of underfilm corrosion formed by a chain of interconnected blisters.[5,9,10] The blisters periodically rupture beneath the coating, and tracks so produced resemble filiform corrosion. These interconnected blisters generally occur under unblemished coatings without breaks or flaws and have been observed in this laboratory on submerged specimens of painted aluminum.

In the present paper, filiform corrosion is defined in the more restricted sense to mean the type of corrosion described by Sharman. Thus, filiform corrosion occurs on coated specimens of iron (or steel), aluminum, and magnesium[4,11] which are exposed to a humid air environment. It originates at a break in the coating where some soluble ionic species is present. The filiform track is composed of two parts: the head and the tail. Corrosion takes place in the head which is filled with a liquid solution. The tail is filled with dry corrosion products and is usually considered to be inactive. A distinct interface between the dry tail and the active head does not exist, but for the purposes of this discussion the head will be considered to be that region within which the primary electrochemical reactions take place. The back of the head is nearest the tail, and the front is on the opposite side of the corrosion cell at the leading edge of the track. Figure 1 shows typical filiform corro-

*Submitted for publication August, 1982; revised December, 1982.

*Electrochemical Technology Corp., Seattle, Washington.

0010-9312/83/000153/$3.00/0

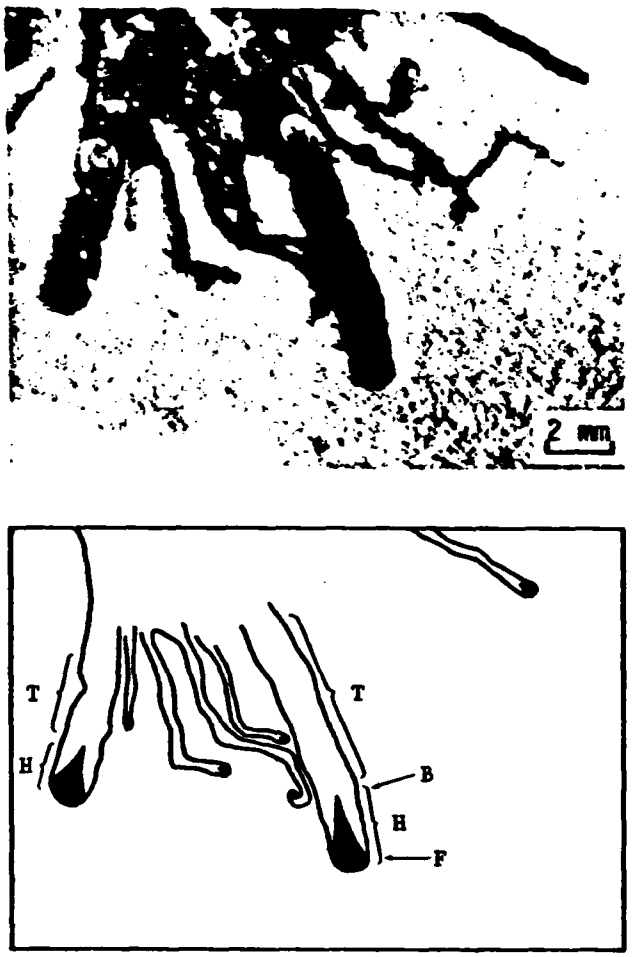

FIGURE 1 — Typical filiform corrosion tracks on steel under a polyurethane coating: H = head, T = tail, B = back of head, and F = front of head.

sion tracks with the characteristic v-shaped color interface which occurs only on iron.

Characteristics of Filiform Corrosion

Summary of Filiform Corrosion Data from the Literature

Many studies of filiform corrosion have been conducted since Sharman presented his work in 1944. Qualitative and semiquantitative observations constitute much of this work. The quantitative data as well as the most precise qualitative observations are listed in Table 1.

The information in Table 1 suggests that filiform corrosion progresses by essentially the same mechanism on iron, aluminum, and magnesium. It is interesting, therefore, that many authors describing this phenomenon have concentrated on the differences exhibited on the different metals, or under different types of coatings, and have failed to successfully explain the basic mechanism relating all filiform corrosion. It is generally accepted that filiform corrosion is a type of differential aeration cell. The cell exhibits a definite front-to-back asymmetry and proceeds in one direction for extended periods of time, but how is this asymmetric corrosion cell formed and maintained? We know that in air, oxygen s the limiting reactant[12] but what limits oxygen transport and how does oxygen reach the head? Many authors discuss the limits of relative humidity within which filiform takes place, but no convincing explanation of the limits has been provided. These and other questions are best answered by studying the general features common to all filiform corrosion systems.

A study of the literature (Table 1) reveals that filiform corrosion exhibits many common characteristics regardless of the type of metal is acts upon. The primary characteristics are listed in Table 2. The model presented in this paper, based on Kaesche's[8] mechanism, is consistent with all seven of the characteristics listed in Table 2.

Thermodynamics and Chemistry

By definition, the electrochemical reactions are confined to the head of a filiform track. Potential and pH measurements clearly indicate that the front of the head is the most anodic site, and the primary cathodic site is at the back of the head. An incidental cathodic area has been observed in a region surrounding the head (6), but experimental data presented later in this paper show that this area is not the primary cathodic site. Table 3 summarizes the pertinent electrochemical reactions which can occur on iron, aluminum, or magnesium. Figure 2 gives Pourbaix[13] diagrams for these metals. Estimates of the potential and pH at different positions inside the head have also been included in Figure 2. The values of pH are from Table 1, and potentials are discussed in the following paragraphs.

On iron, pH variations indicate that metal is oxidized to the ferrous state at the tip of the head, and oxygen is reduced near the junction of the head and tail. If a chloride salt was used to initiate corrosion, ferrous ions go into solution and form ferrous chloride electrolyte. The separation of anode and cathode within the head produces a potential gradient in the electrolyte which causes chloride anions to migrate toward the front of the head. Cations migrate toward the rear where a high pH exists due to the cathodic reaction, 2 (Table 3). Near the back of the head, the oxygen concentration in solution is high enough to oxidize ferrous ions to the ferric state by the homogeneous reaction 3. The boundary between the region containing primarily ferrous iron and the ferric iron region is visible as the characteristic v-shaped interface. In front of the interface the head contents appear blue, blue-green, or gray in color, and behind the interface a rust colored deposit is visible. On the Pourbaix diagram, the pH at the front of the head is between one and four (Table 1), and the potential in the solution is expected to be slightly positive, with respect to the standard dissolution potential for iron, −0.44 V. The potential drop in solution is expected to be small because a concentrated ferrous-salt solution exists in the head.[14] At the back of the head, the pH is about 12.[14] Ferric hydroxide corrosion products fill the tail; therefore, conditions in the tail must be represented in Figure 2A by a point above line 16. As the ferrous ions migrate toward the rear of the head, the pH rises and a ferrous hydroxide gel forms. Gels have also been reported in filiform tracks on both aluminum[6,7] and magnesium.[6,11]

The reaction sequence for corrosion of aluminum is shown in Table 3B. The primary difference between aluminum and iron is that only one oxidation state of aluminum, Al^{+3}, is stable in aqueous solution.[15,16] Slabaugh, *et al.*,[7] have indicated that the potential at the tip of the head is about −0.96 V, versus a calomel reference electrode (−0.73 V_{SHE}). Slabaugh, *et al.*, also determined the potential difference in solution between the front and the back of the head to be 0.09 V, with a polarity such that anions migrate toward the front. An erratic pH greater than about 3.5 was observed in the tail,[6] and the Pourbaix diagram (Figure 2B) indicates the white solid contained in the tail is aluminum hydroxide.

The chemistry of filiform corrosion on magnesium is assumed to be similar to that on aluminum. The recorded observations and Pourbaix diagram support this conclusion, but quantitative data are lacking. On magnesium, the head is acidic, and hydroxide products fill the tail.[6,11] Hoch[6] found a pH of 2 to 3 in the head (Table 1), and a pH of 3 to 4 in the tail. Figure 2C shows that no hydroxide will precipitate at this low pH. Holler[11] observed a pH greater than 10 in the tail. The potential for corrosion is considered to be −1.71 V_{SHE}, consistent with the potential observed during pitting of magnesium.[17]

TABLE 1 — Summary of Data from the Literature and Present Work on Filiform Corrosion[1]

No.	Observation	Coating	Metal	Initiating Electrolyte	Relative Humidity (%)	Temp. (°C)	Reference
1.	**Growth Characteristics**						
	A. Collisions						
	FC head is deflected away from and will not cross FC tails, or breaks in the coating	lacquer	steel	acetic acid	—	—	Sharman (1944)[3]
		various	cold-rolled steel	acetic acid	86	24	Van Loo (1953)[4]
		urea-alkyd	cold-rolled steel	—	85	room	Slabaugh (1954)[14]
		copol varnish	steel	NaCl	60-94	—	Singhania (1971)[32]
		—	steel	—	80	23	van der Berg (1977)[10]
		poly-urethane	steel	NaCl	90	23	Present work
		4-types	Al	HCl	85	40	Slabaugh (1972)[7]
	FC heads cross FC tails	—	Al	—	—	—	Hoch (1971)[6]
	B. Head damage						
	Damage to the head caused FC to form 2 or 3 tracks	copol varnish	steel	NaCl	60-90	—	Singhania (1971)[32]
	C. Tail damage						
	Damage to the tail does not disrupt FC	copol varnish	steel	NaCl	60-90	—	Singhania (1971)[32]
		poly-urethane	steel	NaCl	90	23	Present work
2.	**Velocity Characteristics**						
	A. Speed (mm/day)						
	0.85	lacquer	steel	acetic acid	—	—	Sharman (1944)[3]
	0.04-0.08	boiled linseed oil	carbon steel	NaCl	—	—	Hargreaves (1952)[5]
	0.5[2]	varnish	cold-rolled steel	acetic acid	86	24	Van Loo (1953)[4]
	0.29-0.43	urea-alkyd	cold-rolled steel	—	85	room	Slabaugh (1954)[14]
	0.28	varnish	steel	—	—	—	Preston (1956)[9]
	0.33-0.53	varnish	steel	NaCl	85	25	Kaesche (1959)[8]
	0.5	alkyd	steel	—	80	—	Kennedy (1966)[24]
	0.01-0.26	nitro-synthetic	steel	NaCl or $FeCl_2$	80	23	van der Berg (1977)[10]
	0.19-0.86	acrylic	steel	NaCl or $FeCl_2$	80	23	van der Berg (1977)[10]
	0.26-0.43	alkyd urea	steel	NaCl or $FeCl_2$	80	23	van der Berg (1977)[10]
	0.01-0.46	epoxy-urea	steel	NaCl or $FeCl_2$	80	23	van der Berg (1977)[10]
	0.03-0.13	epoxy & Cl rubber	mild steel	8-types	80	27	Schofield (1981)[29,(3)]

No.	Observation	Coating	Metal	Initiating Electrolyte	Relative Humidity (%)	Temp. (°C)	Reference
	0.16-0.50	poly-urethane	steel	NaCl	90	23	Present work
	0.1 (average)[4]	22-types	iron	HCl	75	25	Holler (1963)[11]
	0.1 (average)[4]	22-types	Al	HCl	75	25	Holler (1963)[11]
	0.1 (average)[4]	22-types	Mg	HCl	75	25	Holler (1963)[11]
	B. Speed vs thickness						
	Growth more vigorous under thick coatings	—	iron	—	—	—	Slabaugh (1954)[14]
	Growth is independent of coating thickness	copol varnish	steel	NaCl	60-90	—	Singhania (1971)[32]
	C. Speed vs width						
	Speed independent of width	—	steel	—	80	23	van der Berg (1977)[10]
	D. Speed vs. humidity						
	Speed increased with relative humidity	copol varnish	steel	NaCl	60-94	—	Singhania (1971)[32]
	0.025-0.030 (mm/day) 0.030-0.038 (mm/day)	copol varnish	steel	NaCl	70 85	—	Singhania (1971)[32]
	Speed decreased as RH increases	various	steel	NaCl	70-94	25	Preston (1956)[9]
3.	**Physical Dimensions**						
	A. Width (mm)						
	0.1-0.5	lacquer	steel	acetic acid	—	—	Sharman (1944)[3]
	0.05-0.1	boiled linseed oil	carbon steel	—	—	room	Hargreaves (1952)[5]
	0.15[2]	varnish	cold-rolled steel	acetic acid	86	24	Van Loo (1953)[4]
	0.5	urea-alkyd	cold-rolled steel	—	85	room	Slabaugh (1954)[14]
	0.1-0.2	nitro-cellulose lacquer	steel	NaCl or $(NH_4)_2SO_4$	58-100	25	Preston (1956)[9]
	0.1-0.3	varnish	steel	NaCl	65-85	25	Kaesche (1959)[8]
	0.1-0.5	alkyd	steel	—	80	—	Kennedy (1966)[24]
	~0.25	—	steel	NaCl or $FeCl_2$	80	23	van der Berg (1977)[10]
	0.8[2]	—	iron	—	—	—	Koehler (1977)[21(3)]
	0.04-0.32	epoxy & Cl rubber	mild steel	8-types	80	27	Schofield (1981)[29(3)]
	0.1-3	poly-urethane	mild steel	NaCl	90	23	Present work
	0.36[2]	—	Al	—	—	—	Hoch (1971)[6]
	0.5-3	4-types	Al	HCl	85	40	Slabaugh (1972)[7]
	B. Width vs. humidity						
	Track width increases with increasing relative humidity	various	cold-rolled steel	acetic acid	86	24	Van Loo (1953)[4]
		copol varnish	steel	NaCl	60-90	—	Singhania (1971)[32]
		4-types	Al	HCl	85	40	Slabaugh (1972)[7]

AD-A138 487 DETERMINATION OF THE EFFECT OF COMPOSITION STRUCTURE AND ELECTROCHEMICAL . (U) ELECTROCEEMICAL TECHNOLOGY CORP SEATTLE WA T R BECK ET AL. DEC 83 ETC-81-50 2/2

UNCLASSIFIED N00014-82-C-0052 F/G 11/3 NL

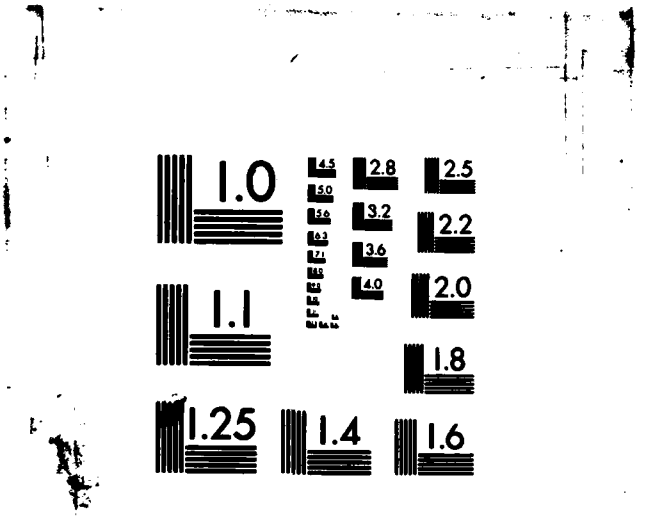

MICROCOPY RESOLUTION TEST CHART
NATIONAL BUREAU OF STANDARDS-1963-A

No.	Observation	Coating	Metal	Initiating Electrolyte	Relative Humidity (%)	Temp. (°C)	Reference
C.	Width vs. thickness						
	Width increases with coating thickness	various	cold-rolled steel	acetic acid	86	24	Van Loo (1953)[4]
		varnish	steel	NaCl	85	25	Kaesche (1959)[8]
D.	Height of tail (μm)						
	30[2]	varnish	steel	—	—	25	Kaesche (1959)[8]
	1.5-40[5]	various	steel	NaCl or $FeCl_2$	80	23	van der Berg (1977)[10]
	17-25[2]	—	iron	KCl	90	38	Koehler[22(3)]
E.	Depth of corrosion into the metal (μm)						
	10[2]	varnish	steel	—	—	25	Kaesche (1959)[8]
	5.1-7.6	—	—	—	—	—	Slabaugh (1962)[30]
	5	—	—	—	—	—	Kennedy (1966)[24]
	1.	epoxy & Cl rubber	mild steel	8-types	80	27	Schofield (1981)[29(3)]
	up to 15[2]	—	Al	—	—	—	Hoch (1971)[6]
4.	Chemical Composition						
A.	Head solution						
	38-50% nonvolatile components	urea-alkyd	cold-rolled steel	—	85	room	Slabaugh (1954)[14]
	no Fe^{+3}	urea-alkyd	cold-rolled steel	—	85	room	Slabaugh (1954)[14]
	Fe^{+2}	urea-alkyd	cold-rolled steel	—	85	room	Slabaugh (1954)[14]
	$FeCl_2$, $FeCl_3$, β-FeOOH	—	steel	$FeCl_2$	80	23	van der Berg (1977)[10]
	Cl^-, but no K^+	—	iron	KCl	—	—	Koehler (1977)[21(3)]
	Sulfur	—	iron	sulfate, cation unknown	—	—	Koehler (1977)[21(3)]
	H_2 (g)	poly-urethane	Al	HCl	75	room	Hoch (1971)[6]
	Cl^-	various	Al	HCl	85	40	Slabaugh (1972)[7]
	H_2 (g)	various	Al	HCl	85	40	Slabaugh (1972)[7]
	gas bubbles	various	Mg	HCl	75	25	Holler (1963)[11]
	H_2 (g)	—	Mg	—	—	—	Hoch (1971)[6]
B.	Head pH						
	12 (at the rear)	urea-alkyd	cold-rolled steel	—	85	room	Slabaugh (1954)[14]
	1 (at the front)	—	1010 steel	—	—	—	Hoch (1971)[6]
	3-4	—	1010 steel	—	—	—	Hoch (1971)[6]
	1-2	—	steel	Cl^-	80	23	van der Berg (1977)[10]
	1.0	poly-urethane	Al	HCl	75	room	Hoch (1971)[6]
	1.5-2	various	Al	HCl	85	40	Slabaugh (1972)[7]
	acid (litmus paper)	various	Mg	HCl	75	25	Holler (1963)[11]
	2-3	—	Mg	—	—	—	Hoch (1971)[6]

No.	Observation	Coating	Metal	Initiating Electrolyte	Relative Humidity (%)	Temp. (°C)	Reference
C.	Tail						
	γ-FeOOH, α-FeOOH	—	steel	NaCl	80	23	van der Berg (1977)[10]
	no Cl^- or K^+	—	iron	KCl	—	—	Koehler (1977)[21(3)]
	hydrated alumina	various	Al	HCl	85	40	Slabaugh (1972)[7]
D.	Tail pH						
	3.5 ≤ pH < alkaline	poly-urethane	Al	HCl	75	room	Hoch (1971)[6]
	pH > 10	various	Mg	HCl	75	25	Holler (1963)[11]
	3 < pH < 4	—	Mg	—	—	—	Hoch (1971)[6]
5.	**Coating Characteristics**						
A.	Coating permeability						
	No FC under pigmented paints	lacquer	steel	acetic acid	—	—	Sharman (1944)[3]
	No FC under paints above CPVC[6]	various	cold-rolled steel	acetic acid	86	24	Van Loo (1953)[4]
B.	Plated metal coatings	Ni	steel	—	—	—	Hargreaves (1952)[5]
		Cr	steel	—	—	—	Van Loo (1953)[4]
		Sn	steel	—	—	—	Van Loo (1953)[4]
		Ag	steel	—	—	—	Van Loo (1953)[4]
		Au	steel	—	—	—	Van Loo (1953)[4]
6.	**External Atmosphere**						
A.	Humidity limits						
		various	cold-rolled steel	acetic acid	65-95	24	Van Loo (1953)[4]
		lacquer	mild steel	NaCl	58-97.5	25	Preston (1956)[9]
		lacquer	mild steel	$(NH_4)_2SO_4$	80-100	25	Preston (1956)[9]
		—	—	—	60-95	—	Slabaugh (1962)[30]
		—	iron	—	60	—	Hoch (1971)[6]
		epoxy or Cl rubber	mild steel	4-types of $SO_4^=$	80	27	Schofield (1981)[29(3)]
		4-types	Al	HCl	30-95	40	Slabaugh (1972)[7]
		various	Mg	HCl	<85	25	Holler (1963)[11]
B.	Gas atmosphere						
	O_2 required	18-types	steel	—	86	20	Slabaugh (1966)[12]
	CO_2 inhibits FC	18-types	steel	—	86	20	Slabaugh (1966)[12]
	Growth in O_2	4-types	Al	HCl	85	40	Slabaugh (1972)[7]
	Growth in CO_2	4-types	Al	HCl	85	40	Slabaugh (1972)[7]
	No growth in N_2	4-types	Al	HCl	85	40	Slabaugh (1972)[7]
	No growth in He	4-types	Al	HCl	85	40	Slabaugh (1972)[7]

(1)Dash (—) in data column means data not reported by author.
(2)Estimated from photograph.
(3)This work does not strictly conform to the present definition of filiform corrosion because coating was unbroken.
(4)Calculated from authors' average filiform length.
(5)Calculated by dividing average width by tabulated values of the base/height ratio.
(6)CPVC is critical pigment volume concentration, *i.e.*, that concentration of pigment at which sufficient binder is present to just fill completely the voids left between the pigment particles.

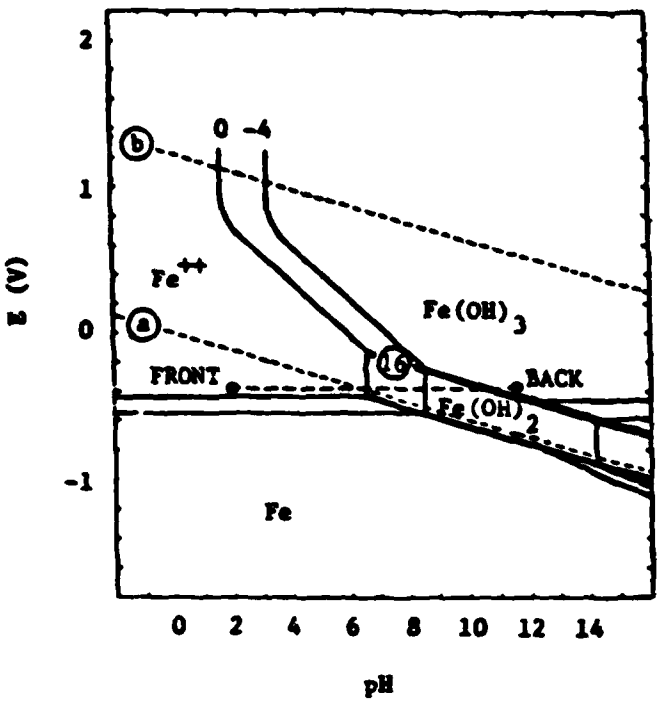

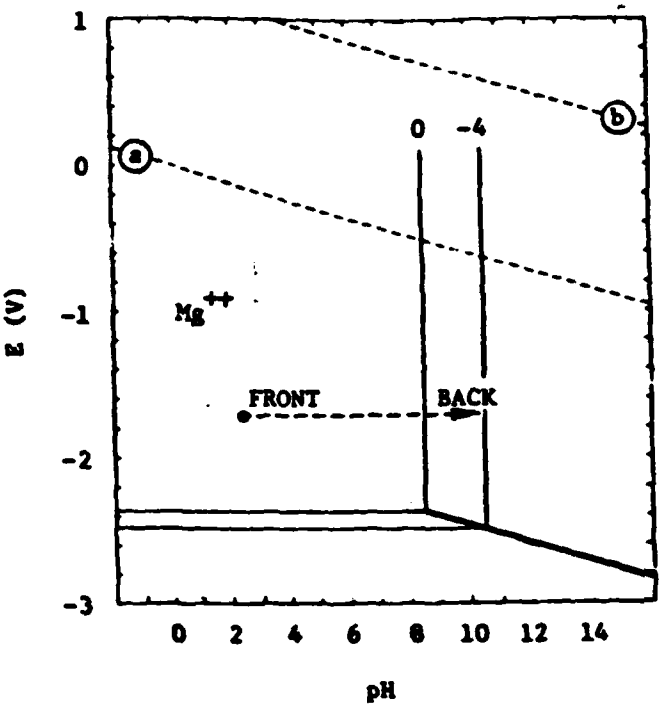

FIGURE 2 — Pourbaix diagram for iron, aluminum, and magnesium showing estimated electrochemical conditions at different locations in FC cells: line a represents the hydrogen reaction, 10, and line b is the oxygen reaction, 2.

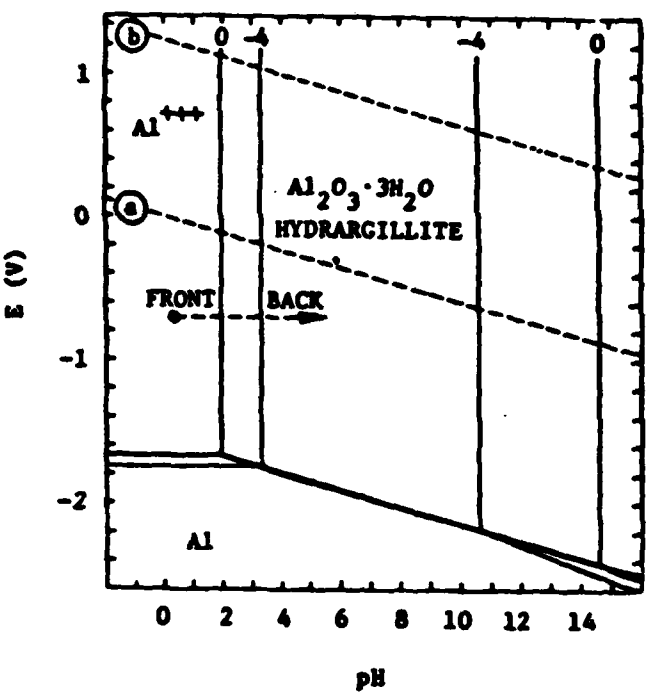

The Pourbaix diagrams of all three metals show that the dissolution potentials are below that required to produce hydrogen gas (line a). Gas has not been observed on iron, but is evolved on both aluminum and magnesium. The gas is presumed to be hydrogen, but it is likely that hydrogen production is a secondary cathodic reaction, as in the pitting of aluminum[18] and magnesium.[19]

Mechanism

The thermodynamic driving force and reactions which produce an oxygen-driven corrosion cell are well established, but the kinetic and transport mechanisms of filiform corrosion are not yet fully understood. A model is described here which considers how the reaction takes place, how the reactants (oxygen and water) reach the head, and how the external conditions and geometry combine to produce a stable corrosion cell. Calculations utilizing available data provide the basis for evaluating proposed mechanisms, and suggest that Kaesche's model[8] of oxygen diffusion through a porous tail is the most satisfactory.

TABLE 2 — Primary Characteristics of Filiform Corrosion

1. The filament motion is directionally stable; the tracks are relatively straight for long distances.
2. Tracks generally do not cross each other or breaks in the surface coating.
3. The size and speed of the cells are insensitive to the physical properties of the coating.
4. Oxygen is required for filiform corrosion to propagate.[1]
5. Water is required, but filiform occurs only within a limited range of relative humidity.
6. The front edge of the head contains a solution of low pH and appears to be the most anodically active area.
7. Anions of the "inoculating" salt are conserved in the head; cations are not conserved.

[1]Demonstrated for filiform corrosion on iron and aluminum, but no reported experiments for magnesium.

The quantitative evaluation of filiform mechanisms required knowledge of the geometry of the corrosion cell. A representative track on iron was observed under a microscope, and measurements were made of the head and tail. The height of the tail above its surroundings (h) was 29 μm, and the width (w) was 1.52 mm. The average depth of corrosion into the iron substrate, and a typical velocity, were obtained from the literature (Table 1).

$$\text{depth}\,(d) = 10\,\mu\text{m} \tag{1}$$

$$\text{velocity}\,(v) = 2 \times 10^{-3}\,\mu\text{m/s} \tag{2}$$

The iron and oxygen consumed by corrosion can be calculated from the volume of iron removed by assuming Fe_2O_3 is the ultimate corrosion product.

$$N_{Fe} = 4.2 \times 10^{-12}\,\frac{\text{mol-Fe}}{\text{s}} \tag{3}$$

$$N_O = 3.1 \times 10^{-12}\,\frac{\text{mol-O}_2}{\text{s}} \tag{4}$$

We now wish to investigate how this quantity of oxygen could diffuse to the cathodic reaction site. Two possibilities present themselves immediately: diffusion through the coating, or diffusion through the filiform tail. The occurrence of filiform corrosion under metal films (5B, Table 1) would seem to preclude any general mechanism involving diffusion through the coating, but such a mechanism has been proposed in the literature to explain corrosion under organic coatings.

Consider first the diffusion of oxygen through the coating according to Fick's law:

$$J = D\,\frac{\Delta C}{\tau} \tag{5}$$

$$N = AJ \tag{6}$$

where J = molar flux, mol/mm^2·s; D = diffusivity, mm^2/s; ΔC = concentration difference across the coating, mol/mm^3; τ = coating thickness, mm; N = molar transport, mol/s; and A = area of diffusion, mm^2. Assume the area for diffusion to be that of the head (~ 2.3 mm^2). Brandrup and Immergut[20] list the diffusivities of oxygen through several polymers. The diffusivities vary about two orders of magnitude:

$$10^{-6} < D_p(O_2) < 10^{-4}\,\text{mm}^2\text{/s} \tag{7}$$

Assume also that the oxygen concentration is zero on the solution side of the coating. Then the concentration difference is obtained by multiplying the oxygen concentration in air (8.6×10^{-3} mol/L) by the dimensionless solubility of oxygen in polymers, approximately 7×10^{-2}.[20] For a paint thickness of 50 μm, the rate of oxygen diffusion through the polymer coating is:

$$2.8 \times 10^{-14} < N(O_2) < 2.8 \times 10^{-12}\,\frac{\text{mol-O}_2}{\text{s}} \tag{8}$$

Thus, a filiform head could expose an area marginally sufficient to transport the required oxygen.

This calculation shows that the maximum oxygen flux through a typical polymer may be sufficient to support filiform corrosion, but two objections can be raised to this mechanism. The first has already been mentioned: filiform corrosion occurs underneath metal-plate coatings. The second is that if oxygen passes through the coating in a direction normal to the metal surface, a symmetric cell should develop without separation of anodic and cathodic reaction sites. The directionality of filiform growth precludes a symmetric corrosion cell.

A mechanism which does explain the directional characteristic of filiform corrosion has been proposed by Kaesche;[8] oxygen and water diffuse from the break in the coating to the head through the porous filiform tail. A rationale for this mechanism can be found by considering the model filiform track on iron. The volume occupied by ferric hydroxide [$Fe(OH)_3$] is easily calculated and is about 97% of the volume inside the tail. When the corrosion products have dehydrated to Fe_2O_3, they occupy about 55% of the tail volume. A porous tail is therefore expected.

Can oxygen diffuse through a porous tail at a rate sufficient to support the corrosion cell? Oxygen diffuses through air according to Equation (5). At 25 C,

$$D_{air}(O_2) = 21\,\text{mm}^2\text{/s}. \tag{9}$$

The oxygen concentration in the external atmosphere is

$$C_{air}(O_2) = 8.6 \times 10^{-3}\,\text{mol/l}. \tag{10}$$

Then, assuming the concentration of oxygen in the head to be zero, the maximum oxygen flux through a 150 mm tail is:

$$J_{air}(O_2) = 1.2 \times 10^{-9}\,\frac{\text{mol}}{\text{mm}^2\text{·s}} \tag{11}$$

Calculating the area for diffusion in the tail as

$$A = (h + d)w(1 - \epsilon)^{2/3}$$

$$= 3.5 \times 10^{-2}\,\text{mm}^2 \tag{12}$$

where ϵ = the solids fraction in the tail, ≈ 0.55. The total oxygen reaching the head is, according to Equation (6),

$$N(O_2) = 4.2 \times 10^{-11}\,\frac{\text{mol-O}_2}{\text{s}} \tag{13}$$

This rate of diffusion is roughly ten times that required to support corrosion and more than ten times the maximum value calculated for diffusion through a polymer coating. Therefore, for tails shorter than about 150 mm, diffusion through the tail is preferred.

A large cathodic area has been observed surrounding the anodic filiform head,[6,14] and it has been suggested that this cathode drives the corrosion reaction. Three factors argue against this hypothesis. First, the cathodic area is symmetrical around the head. This symmetry is inconsistent with the separation of anodic and cathodic reaction zones and the fact that filiform corrosion cells exhibit asymmetry and directionality. Second, no cathodic detachment of coatings in the area around the head has been observed in this laboratory or reported in the literature. Koehler[21] conducted a series of experiments in which he produced both cathodic detachment and filiform corrosion. He does not mention observing cathodic detachment around filiform heads. Neither do duplicates of Koehler's original photographs,[22] which have been studied in this laboratory, show any indication of cathodic detachment in the areas surrounding filiform heads.

Mass transfer limitations constitute the third reason why the area around the head cannot be the primary cathode. The radius of the large cathode is about 10 times that of the head.[6] Consider a hypothetical cathode surrounding the head which drives the reaction. An ionic current must flow from the anode to the cathode through the coating, and the high resistance of the coating places limits on the size of this hypothetical primary cathode. This statement can be verified by considering the following relationship:

$$i = -K\,\frac{d\phi}{dr} \tag{14}$$

where i = the current density, A/mm^2; K = the conductivity, 1/Ω•mm; and dφ/dr = the potential gradient, V/mm. The conductivity of wet paint is about 10^{-11} Ω^{-1} mm^{-1}.[23] The corrosion rate can be converted to a total corrosion current, and Equation (14) can be integrated to obtain:

$$\ln\left(\frac{r_c}{r_h}\right) = 2K\pi\tau\frac{\Delta\phi}{I} \qquad (15)$$

where r_h = radius of the filiform head, mm; r_c = the radius of the active cathode, mm; I = the total corrosion current; 0.8 × 10^{-6} A; and τ = the cross sectional thickness of the diffusion path (coating thickness), mm. The potential difference around the filiform head has been measured by Slabaugh and Grotheer[14] to be 0.2 mV, but the maximum possible voltage is about 0.84 V, on iron. Assuming the maximum, thermodynamic, potential and applying typical values for the other parameters in Equation (15), one finds

$$\frac{r_c}{r_h} = 1.000 \qquad (16)$$

Therefore, the coating resistance is too high for a large area surrounding the head to be the primary cathodic site.

It could be argued that the diffusion of ions from the large cathodic area toward the head takes place by surface migration at the paint-metal interface, instead of migration through the resistant coating. If water concentrates near the paint-metal interface, the surface conductivity might be orders of magnitude higher than that of a wet paint film. One might then ask what thickness of an aqueous solution would be required for surface diffusion to be a viable mechanism. Rearranging Equation (15) yields:

$$\tau = \frac{I}{2\pi K\Delta\phi}\ln\left(\frac{r_c}{r_h}\right) \qquad (17)$$

$$= \frac{0.8 \times 10^{-6}\ A}{(2)(\pi)(10^{-2}\ \Omega^{-1}mm^{-1})(0.84\ V)}\ln 10$$

$$= 3.5 \times 10^{-5}\ mm. \qquad (18)$$

An aqueous layer this thick could only occur if the coating were detached from the metal. If the measured potential, 2 × 10^{-4} V, is used in Equation (17), one obtains a thickness of 0.15 mm. Clearly, surface migration can only be important if the coating has been disbonded from the metal, and disbonding has not been reported.

Although these order of magnitude calculations do not constitute proof, they provide strong evidence that the primary reactants, oxygen and water, diffuse to the filiform head through a porous tail. As a result, the primary anodic and cathodic reaction sites separate, and a stable, asymmetric, corrosion cell is formed.

Experimental Apparatus and Procedure

Kaesche's mechanism of filiform corrosion is compatible with published observations, but it is at odds with most models proposed by other authors. The most popular concept is that the coating is semipermeable and controls the diffusion of oxygen and water into the filiform head. The semipermeable membrane model has been refuted here by calculations and symmetry arguments, but experimental verification of Kaesche's mechanism was sought. A series of experiments was conceived to test for the existence of a porous tail. The test consisted of observing the speed of selected filiform tracks before and after their tails were sealed to prevent oxygen and water from reaching the head.

Filiform corrosion was initiated on painted steel test panels. The 76 x 127 mm panels were prepared for painting by abrading with a wire brush, then sanding with 600 grit emery paper. The sanded panels were rinsed in both methanol and hexane and then dried in laboratory air. When the panels were dry, a commercial polyurethane paint was applied by spraying. The coating thickness was not recorded for each panel, but random samples were in the range of 25 to 50 μm. The paint was allowed to dry from one to seven days before the experiments were conducted. In order to initiate filiform corrosion, a defect in the paint was inoculated with NaCl solution. A hole was made through the paint with a punch. Then, approximately 10 μL of 1.0 N NaCl solution was placed on the metal at the bottom of the hole. After inoculation, the test panels were placed in a glass chamber and maintained at 90% relative humidity by equilibration with a 2.73 M solution of NaOH. The temperature was controlled by the room thermostat. It was recorded by a thermocouple placed inside the chamber as 21 ± 3 C. Neither the gaseous atmosphere inside the chamber nor the NaOH solution were stirred in these experiments. Condensation was not visible on either the test panels or the chamber walls. Under these conditions, filiform tracks grew freely, and the positions of representative filaments were periodically recorded and photographed.

All physical dimensions of filiform tracks were obtained from photographic records. A ruler was placed in each photograph, and reference positions were marked on the test panels. The positions of filiform heads as well as the track dimensions were obtained by scaling projected images. Filiform speeds reported in Table 1 represent average values obtained by dividing the distance traveled between successive photographs by the elapsed time.

After filiform corrosion had been initiated, selected tails were sealed with epoxy. First, a cut was made across the width of the tail with a scalpel, and the paint film was then peeled back on the side of the cut farthest from the head. Then, epoxy was applied to the open portion of the tail in such a manner that air could not enter. The growth rate of the sealed filiform track was compared to that of two control groups. The first control group was used to test the effects of placing the epoxy on top of an uncut filiform tail which, therefore, remained open to a source of oxygen. Tracks in the second control group were also open to the air. The tails were cut back in the same manner as the sealed group, but the tails were left open, not sealed.

Experimental Results

Typical filiform tracks are shown in Figure 3. The tracks which had been sealed with epoxy (a and b, Figures 3A, 3B) immediately ceased to grow and remained stationary until reactivated when the tail was opened to a source of oxygen. Reactivation occurred in one of two ways: by a cut made into the deactivated track with a scalpel, or by collision of a mobile filiform with the deactivated track at a location between the deactivated head and the epoxy seal. Track b in Figure 3 was reactivated by cutting the tail open with a scalpel. When a stationary track was reactivated, it resumed growing with a speed equal to that observed before the tail was sealed. Filiform tracks in both control groups grew at the same rate as unaltered tracks. These experiments clearly demonstrate the role of the porous tail as the primary diffusion pathway.

During the course of these experiments, several features of filiform growth were observed which have not previously been reported. When a filiform track had ceased growing because the tail was sealed with epoxy, the head retained the characteristic v-shaped boundary between the ferrous and ferric zones. In one case, the boundary lasted 85 days, and in another instance 105 days. In all cases, these experiments were terminated before the boundary changed in any visible way. The oxygen permeability of organic polymers varies greatly,[20] but an order of magnitude calculation verifies that this observation is compatible with tabulated permeability data and again stresses the point that diffusion through the coating is an incidental and minor source of reactant species.

FIGURE 3 — Filiform tracks on steel: Coating = polyurethane, Temp. = 21 C, and RH = 90%.

Another observation concerns the shape of the gray, ferrous region in the head. The shape of this region can change dramatically with time as a track travels across the metal. The data in Table 4 show considerable variation of the length, width, and area of the gray region with time. In extreme cases, islands of gray were left behind in the filiform tail as the head moved forward. These isolated islands were ultimately converted to rust-colored areas, but the ferrous color sometimes persisted for weeks. The mechanism by which the islands are formed and maintained for extended periods is not clearly understood. One explanation is that oxygen transport has slowed down because of changes in physical properties inside the islands. Another possibility is that the transport properties have not changed, but pitting of the substrate occurs within the island. The dramatic shape changes of the ferrous region seem to be more common in larger filiform tracks (w > 1 mm).

TABLE 3 — Reaction Sequences in Filiform Heads

A. Iron

$$Fe \rightarrow Fe^{++} + 2e^- \quad (1)$$

$$\frac{1}{2}O_2 + H_2O + 2e^- \rightarrow 2OH^- \quad (2a)$$

$$Fe^{++} + \frac{1}{4}O_2 + \frac{1}{2}H_2O \rightarrow Fe^{3+} + OH^- \quad (3)$$

$$Fe^{3+} + 3OH^- \rightarrow Fe(OH)_3 \quad (4)$$

$$Fe(OH)_3 \rightarrow \frac{1}{2}Fe_2O_3 + \frac{3}{2}H_2O \quad (5)$$

$$Fe + \frac{3}{4}O_2 \rightarrow \frac{1}{2}Fe_2O_3 \quad (6)$$

B. Aluminum

$$Al \rightarrow Al^{3+} + 3e^- \quad (7)$$

$$\frac{3}{4}O_2 + \frac{3}{2}H_2O + 3e^- \rightarrow 3OH^- \quad (2b)$$

$$Al^{3+} + 3OH^- \rightarrow Al(OH)_3 \quad (8)$$

$$Al + \frac{3}{4}O_2 + \frac{3}{2}H_2O \rightarrow Al(OH)_3 \quad (9)$$

$$H^+ + e^- \rightarrow \frac{1}{2}H_2 \quad (10b)$$

C. Magnesium

$$Mg \rightarrow Mg^{++} + 2e^- \quad (11)$$

$$\frac{1}{2}O_2 + H_2O + 2e^- \rightarrow 2OH^- \quad (2c)$$

$$Mg^{++} + 2OH^- \rightarrow Mg(OH)_2 \quad (12)$$

$$Mg + \frac{1}{2}O_2 + H_2O \rightarrow Mg(OH)_2 \quad (13)$$

$$H^+ + e^- \rightarrow \frac{1}{2}H_2 \quad (10c)$$

It is not known if large filaments produce ferrous islands more frequently than smaller ones, or if the islands are just difficult to observe in smaller tracks.

The data in Table 3 were obtained in an experiment lasting 85 days. In this experiment, the filiform tracks maintained a constant speed of 2.1×10^{-3} μm/s, indicating that the dimensions of the gray zone are unrelated to the rate of filiform propagation.

An attempt was made to correlate filiform speed with tail length. The speeds of various filiform tracks with lengths up to 37 mm were recorded. The speed was independent of tail length.

It was also observed that traveling filiform tracks grew well beneath the thick epoxy drops used to seal filament tails. The thickness of the epoxy was not measured in each case, but was estimated to average about 3 mm. On several occasions, tracks growing toward an epoxy drop continued to grow beneath the epoxy without changing direction. In one instance, the speed was observed to approximately double, from

3.1 x 10^{-3} μm/s to 5.7 x 10^{-3} μm/s, when the head passed beneath the epoxy. The width simultaneously decreased from 0.29 to 0.22 mm.

Other observations were made to compare filiform tracks growing on polished iron with those growing on iron which had been abraded with 600 grit emery paper. Substrate panels were prepared in the usual manner. Then, half of each panel was mechanically polished to a mirror finish with a 1/2 μm diamond paste. When filiform tracks grew across the boundary between the polished and abraded halves of a test panel, no changes in speed, width, or direction were observed. Wherever tracks traveling on a polished half-panel encountered a filiform tail, they were reflected without actually touching the tail. The tracks were between 0.13 and 0.28 mm wide, and the distance of closest approach was between 0.11 and 0.20 mm. On abraded half-panels, colliding filiform tracks were observed to touch the tail before being deflected. Apparently tracks traveling on the polished iron had encountered a source of oxygen before touching the visible ferric hydroxide in the tail.

Discussion

One of the most striking characteristics of filiform corrosion is the relative insensitivity of the phenomenon to the type of coating covering the substrate metal. Several authors have suggested that paint coatings must be semipermeable membranes, or that filiform corrosion is controlled by diffusion through the paint, but these proposals are contrary to the vast majority of reported observations. Slabaugh[7] studied filiform growth on two types of aluminum, with two wash primers, and at least four types of paint. At the end of his report he states, "We conclude that the composition of the coating itself, that is, the primer and finish coats, have very little to do with filiform and that this type of corrosion is a phenomenon associated primarily with the coating-metal interface." Kennedy[24] studied the permeability of coatings to water and carbon dioxide. His data show no correlation between the coating's permeability and its filiform performance on iron. Van Loo, *et al.*,[4] observed filiform corrosion on iron under at least ten organic coatings as well as tinplate, silverplate, and goldplate. Holler[11] observed filiform corrosion on iron, aluminum, and magnesium under 22 different organic coatings and found that "while certain resins did perform better on one of the substrates, a general improvement for all substrates was not noted." These results certainly do not support the conclusion that any single characteristic of the coating controls filiform corrosion. Chan[25] showed that in normal air, oxygen is the limiting reactant, but the permeability of oxygen through gold or tin coatings must be exceedingly low. It is therefore clear that, as a first approximation, any proposed mechanism for filiform corrosion must be independent of coating permeability.

Several mechanisms have been previously proposed, but Kaesche[8] is the only one who recognized the importance of the porous tail as a mass transfer pathway. From his observations, Kaesche concluded that oxygen was present at the back of the viscous region of the head at essentially ambient concentration, but he presented no mathematical or experimental verification of this view. Kaesche's proposal is supported by our calculations and experimental results, as well as the observations that the speed of filiform growth is independent of tail length.

It has been intuitively understood for some time that filiform corrosion represents a form of differential aeration cell, but a more detailed mechanism has not been discussed. Figure 4 illustrates the diffusional process within a filiform head. The wet portion of the head is divided into two regions: a primary anodic region near the front edge, and a primary cathodic region near the back. Farther back, the tail is filled with ferric hydroxide, which eventually dehydrates to form ferric oxide. Oxygen and water diffuse to the head through the porous tail. Inside the head, chloride ions are stationary relative to a coordinate system moving with the filiform head. Metal cations and hydrogen ions migrate from the front

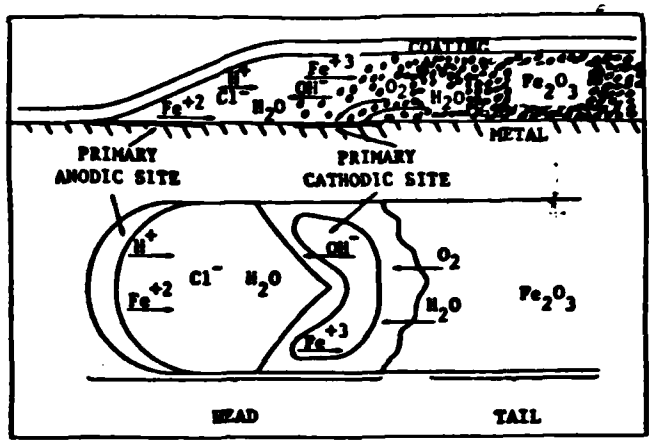

FIGURE 4 — The present model of filiform corrosion showing the primary reaction zones and mass transfer within the filiform head.

TABLE 4 — Observations of the Dark Gray (Ferrous) Region of a Filiform Head

Time (days)	Length (*l*) (mm)	Width (w) (mm)	*l*/w	Area (mm^2)
0	4.7	1.6	2.9	3.3
7	1.3	1.1	1.2	0.82
15	1.0	1.0	1.0	0.56
35	1.2	1.2	1.0	0.61
50	1.9	1.0	1.9	0.76
78	2.5	0.8	3.1	1.2
85	2.2	0.9	2.4	0.77

toward the back of the head. Water is nearly stationary because of its high mole fraction, but some forward diffusion takes place as a result of the hydrolysis reaction with the metal cations. In the rear, behind the cathodic site, water diffuses forward at a faster rate and reacts at the cathode. The hydroxyl ions migrate forward from the cathodic site, but a position is reached, probably near the v-shaped interface, where they are nearly depleted by reactions with hydrogen, ferrous, and ferric ions. This mechanism explains the diffusional transport within the head, but prediction of the exact geometry and details will require a quantitative mathematical model of the corrosion cell.

The model of oxygen and water diffusing through a porous tail is compatible with all of the primary characteristics of filiform corrosion listed in Table 2. It explains why filiform corrosion is relatively independent of coating type; the type of coating does not affect the diffusion of the limiting reactant, oxygen, through the porous tail. It explains how directionality is established and maintained in the filiform head: by separation of the anodic and cathodic reaction sites. The primary anodic site is near the front of the head, and the pH is lowest there because of hydrolysis of the metal cations. A growing head will generally not cross a filiform tail or a break in the coating, because when the head encounters this type of obstruction the front of the head is exposed to a new source of oxygen. This causes changes in the positions of the primary anodic and cathodic sites and therefore changes the direction of travel. This model also explains the observation of Van Loo, *et al.*,[4] that filiform tracks do not develop if a paint coating is loaded with pigment above the critical pigment volume concentration (CPVC). In this case, the paint becomes very permeable to oxygen and water, and the separation of anode and cathode cannot take place. General, nonfiliform types of corrosion do occur under coatings with pigment concentrations greater than the CPVC.[4]

The model also explains the similarities of filiform corrosion on the three metals, aluminum, magnesium, and iron. Van Loo, *et al.*,[4] proposed that an unstable and a stable form of the metal corrosion product is required for filiform corrosion. The present model suggests that this is not true, but that a volume contraction of the corrosion products, or some other mechanism for forming a porous tail, is required.

For filiform corrosion on iron, the existence of a porous tail has been justified theoretically and demonstrated by experiment. The evidence for a porous tail is not as strong for filiform corrosion on aluminum or magnesium. The stable form of iron oxide at 25 C is Fe_2O_3, not the hydroxide $Fe(OH)_3$.[13] The most stable form of aluminum is hydrargillite ($Al_2O_3 \cdot 3H_2O$), and for magnesium, $Mg(OH)_2$.[13] Thus, hydrated corrosion products are formed by both aluminum and magnesium, and a porous tail is more difficult to explain. It appears that the viscosity of these two metal hydroxides reaches a high value while appreciable water is still present. These "wet" hydroxides must possess solid-like rheological properties and form a porous structure as they dry.

Although water is not the limiting reactant, it plays a key role in the mechanism of filiform corrosion. The activity of water in the corrosion cell is determined primarily by the relative humidity, but local variations in activity are expected within the head as a result of chemical reactions. On iron where the ultimate corrosion product is Fe_2O_3, water is not required by the overall chemical reaction. Therefore, water must be conserved and circulate in the region of the filiform head. In fact, if water were to enter the front of the head by diffusing through a semipermeable coating, it must also diffuse out of the head through the tail. This circulation of water from the atmosphere into the head and out the tail into the atmosphere would clearly violate the second law of thermodynamics, provided the only driving force for water diffusion is its own activity gradient. It is unlikely that water diffuses by other than its own activity gradient when passing through either the coating or the tail. We therefore conclude that, on iron, water is immobile with respect to a coordinate system traveling with the filiform head. When aluminum or magnesium corrode, water is consumed [Table 3, Equations (9) and (13)], and these thermodynamic arguments are not applicable. However, because water is not the limiting reactant, the accumulation of water at any point within the head will be near zero. Thus, it is possible to conclude that water is essentially immobile in filiform corrosion cells on all three metals.

One of the observations listed in Table 2 is that filiform corrosion occurs in a limited range of relative humidity. The lower limit of relative humidity depends on the type of metal substrate and the anion of the initiating salt through an as yet unknown mechanism. Order of magnitude calculations indicate that filiform growth on aluminum could be limited by the rate of water diffusion into the head, but water does not appear to be rate limiting with iron substrates. Also, filiform growth rates change abruptly within a narrow band near the lower RH limit. This type of behavior suggests that the lower RH limit results from some kind of equilibrium constraint rather than from any kinetic effect.

Because water is nearly stationary, the activity of water in the head must be very nearly equal to that in the ambient atmosphere, and the solution concentration in the head is determined by the external relative humidity (RH). Therefore, a lower limit of RH will be reached when a saturated solution can no longer be maintained in the head. The corrosion cell will dry out if the minimum activity of water in the cell fluid is greater than the activity in the atmosphere. The minimum activity of water in the cell fluid depends on the chemical composition of the solution in the head and the temperature. It is well known that filiform tracks grow on iron above about 60% RH. Almost all experiments confirming this threshold have been initiated with chloride containing salts (6A, Table 1). At 25 C, the solubility of $FeCl_2$ is about 5.09 M,[26] and the partial pressure of water over a saturated solution is 13.88 Torr.[27] This vapor pressure represents an RH limit of 58%. Slabaugh, *et al.*,[7] initiated filiform corrosion on aluminum with hydrochloric acid and observed growth down to 30% RH at 40 C. Fricke's[28] data were used to interpolate the relative humidity over a saturated solution of $AlCl_3$. A lower RH limit of 34% was calculated. Although this value is slightly higher than that which Slabaugh observed, the agreement is considered adequate in view of the assumption that the head contained only a saturated solution of the metal cation and the anion of the initiating salt. These calculations are consistent with experimental observations and suggest that the reason filiform corrosion ceases at low relative humidities is dehydration of the active head, but other data tend to weaken this hypothesis.

Several authors have initiated filiform corrosion on iron with sulfate salts, and some of the experiments were performed at relative humidities below that of a saturated $FeSO_4$ solution. The data of Schofield, *et al.*,[29] and Preston and Sanyal[9] suggest that at about 25 C filiform corrosion can be induced on iron with sulfate salts when the RH is above about 80%. It is generally agreed that sulfate induced filiform tracks are shorter and thinner than chloride induced tracks grown under identical conditions. Koehler's photographs[21] show that when sulfate is present, the tracks tend to decrease in width as they progress, and many small tracks emanate from the larger tails.

It should also be pointed out that the "filiform" corrosion produced by Koehler and Schofield, *et al.*, does not strictly conform to the definition used in this paper because the coatings were undamaged. However, it appears likely that cracks in the coatings were unintentionally produced by corrosion blisters at the inoculation site. Koehler's photographs show extensive corrosion and blistering in the inoculated region. Also, Schofield reported observing two distinct speeds of filiform growth, and Preston and Sanyal[9] observed that "filiform" corrosion travels under unblemished coatings much more slowly than it does when the coating is ruptured, exposing the metal to the atmosphere. Preston and Sanyal's results have been verified by work performed in this laboratory. These results suggest that cracks are often formed after an initial induction period, and Sharman-type filiform corrosion can then occur.

Based on this evidence, it has been concluded that near 25 C, filiform corrosion can be induced with a variety of sulfate salts at relative humidities above about 80%. The activity of water over a saturated solution of $FeSO_4$ is about 0.94 at this temperature. It is therefore evident that the solution in the filiform head contains compounds other than $FeSO_4$ and water. These additional compounds could be either electrolytes or soluble species leached from the metal or coating. Slabaugh and Kennedy[30] have suggested that chloride leaches out of some types of vinyl coatings, for example. The head solution could also accumulate surface contaminants, particularly if the contaminants are electrolytes, and the filiform tracks emanate from a blister. When a blister first forms, the contaminating anions will migrate toward local anodic sites. If the blister becomes large enough to crack the coating, admitting oxygen, the local anodic sites which are near the edge of the blister may then form filiform corrosion heads. Another possible explanation of the low RH limit for sulfate induced filiform corrosion is that the head contains some of the initiating salt cations. This statement is not a contradiction of the "conservation of anions" characteristic of filiform corrosion (Table 2) if the cations never achieve a steady-state concentration. This conclusion is supported by the fact that sulfate induced filiforms are short, tapered, and produce many smaller secondary tracks growing out from the original tails. This suggests that sulfate anions as well as cations are lost as the head moves, and eventually so many cations will be lost that the head will dehydrate. Without further analytical work, it is not possible to conclude which explanation is more likely.

It is well documented that near 100% RH, general corrosion continues but filiform ceases.[4,7,9] Often, blistering is observed under these conditions of high RH. This fact indicates that filiform stops not because of a lack of reactants for corro-

sion, but from some disruption of the filiform mechanism. The exact nature of the interference has not been proven, but one explanation is that high RH slows the dehydration of corrosion products which then build up in the tail as a wet gel. When this happens, the diffusion resistance for oxygen increases and eventually the asymmetry of the corrosion cell is destroyed. Blisters and general corrosion then predominate.

Another condition which apparently causes a disruption of the filiform mechanism is the presence of 1 to 5% of carbon dioxide in the gaseous atmosphere.[12,25] The data are limited and no definite explanation can be presented, but one possibility is that the ion concentration in the head fluid is reduced by precipitation of carbonate compounds. Under air atmospheres, the electrolyte in the head contains ferrous cations and the anions of the initiating salt. When carbon dioxide is introduced, carbonic acid is formed in the head solution. The presence of carbonic acid has two effects: it provides bicarbonate ions which form a relatively insoluble precipitate with ferrous ion, and it buffers the pH of the solution in the acid region, thereby uncoupling the pH from the cathodic reaction. The iron bicarbonate therefore precipitates in regions of high concentration of ferrous ion rather than in regions of high pH.

An approximate calculation of the maximum concentration of ferrous ions which can occur when carbon dioxide is present has been performed to test this model. As a first approximation, all ionic activity coefficients were assumed to equal one, and single-electrolyte solubility products were used without correction. The ferrous ion concentrations calculated by this method varied according to the concentration of CO_2 in the atmosphere. At 1% CO_2, the maximum ferrous ion concentration was about 0.16 M, and at 5% CO_2 it was about 0.1 M. These concentrations are considerably lower than the saturation concentrations of ferrous chloride or ferrous sulfate, the salts usually found in a filiform head. Therefore, the presence of CO_2 has decreased the solubility of ferrous ions in the filiform head and has raised the relative humidity limit for filiform growth. Under these conditions, one might reasonably expect blistering and general corrosion to proceed faster than filiform corrosion. Chan[25] observed nonfiliform types of corrosion when CO_2 was present, but he did not classify his observations as to blisters, general corrosion, etc.

One of the primary characteristics of filiform corrosion is conservation of anions in the head (4A, Table 1). The simplest explanation of this requirement is that anions migrate toward the front of the head because of the gradient in electrochemical potential between the anode and the cathode. Therefore, separation of anode and cathode is required in a filiform corrosion cell.

Our present model of filiform corrosion satisfactorily explains many aspects of this phenomenon, but some important questions remain unresolved. In general, these questions center around what determines the speed and width of a filiform corrosion cell. Related questions also arise:

1. What is the mechanism of coating disbonding?
2. Is the fluid in the head under hydrostatic pressure?
3. What factors cause the v-shaped interface to form on iron?
4. Is a v-shaped interface present in cells on aluminum or magnesium?

These questions must be addressed in order to attain a more thorough understanding of the filiform mechanism.

In order to understand what factors control the speed of filiform corrosion, we must understand how the coating is disbonded from the substrate metal. The disbonding mechanisms discussed in the literature can be divided into three basic categories: hydrostatic pressure, mechanical prying, and anodic undermining. Another mechanism might involve chemical attack, *i.e.*, low pH weakening the paint-metal adhesion. None of these individual mechanisms appear satisfactory.

Osmosis has been proposed as one mechanism producing hydrostatic pressure in the filiform head. In order for osmotic pressure to develop, a semipermeable membrane is required. On iron, we may consider the solution in the head to be composed of ferrous chloride and water. Therefore, a semipermeable membrane would have to be impermeable to ferrous chloride. It is difficult to see how ferric hydroxide could form such a membrane when ferric chloride and hydroxychloride compounds are known.[16] In this instance, ferrous chloride appears to be soluble in the semipermeable membrane. A possible resolution of this dilemma is to consider air as the semipermeable membrane. Water can pass, in the form of vapor, while inorganic salts cannot. However, in this case, we expect chloride salts to be present in the solution (ferric hydroxychloride) adjacent to the membrane (air), and loss of chloride from the head would occur because of the low mobility of ions in the nearly dry solution.

Another mechanism which is capable of producing hydrostatic pressure in the head is electroosmosis. In this mechanism, water is pumped into the head by the current (ions), and no semipermeable membrane is required. Very little quantitative data are available on electroosmosis, but this mechanism could explain why filiform corrosion reportedly does not take place on some types of metal.[4] The direction of the electroosmotic flow depends on the sign of the zeta potential and is, therefore, expected to be a function of the type of metal cation and the salt concentration in the head solution.

No single mechanism satisfactorily explains how disbonding takes place. Electroosmosis can produce hydrostatic pressure in the head, but why does the disbonding proceed most rapidly at the front edge? If the coating disbonds only as a result of pressure, why does the head not enlarge radially? A mechanical prying mechanism has also been proposed. In this mechanism, the coating is separated from the metal by the high-specific-volume reaction products. It would appear that the prying forces should be greatest at the edge of the head in the corner where it meets the dry tail. It is therefore difficult to explain why disbonding occurs fastest at the front of the head. In contrast, anodic undermining and chemical attack mechanisms do explain why disbonding takes place primarily near the anode, but they do not explain why the head should advance in stages, periodically moving forward and then remaining motionless for a time.[10] This type of motion is typical of that produced by hydrostatic pressure.[31] This body of evidence suggests that at least two factors contribute to the overall disbonding mechanism.

One of the most obvious characteristics of filiform corrosion on iron is the v-shaped interface between the gray- and rust-colored portions of the head. No satisfactory explanation of the v-shape has yet been presented. The only consensus regarding the interface appears to be that iron is in the ferrous state on the gray side, and ferric iron, formed by reaction with oxygen (reaction 3, Table 3), is on the rust-colored side. Oxygen and water diffuse to the color interface (reaction site) from one side, while ferrous ions come from the opposite side (Figure 4). Oxygen will exhibit its highest activity near the back of the head and become depleted toward the front. The spatial distribution of oxygen can be represented as contours of constant oxygen activity (isooxygen lines). It is observed that the v-shaped interface is distinct and sharp. This suggests that reaction 4 is relatively fast and is probably limited by mass transfer rather than kinetic considerations. Under these conditions, the v-shaped interface represents a line of constant activity for ferrous ions and oxygen, *i.e.*, an isooxygen line. The filiform corrosion tail is porous, and if the porosity is uniform, the isooxygen lines in the tail far from the head are straight and perpendicular to the axis of the tail. Near the v-shaped interface, the isooxygen lines bend forward near the edges of the filiform track. This fact suggests that, in the region of the head, the filiform tail is more permeable to oxygen near the edges. When the gray, ferrous zone attains a large length-to-width ratio (Table 4), this fact is clearly evident. It is also supported by the observation of filiform tracks which deflect off tails without actually touching. Although the v-shaped interface may be the result of increased oxygen

permeability near the outside edges of the tail, the reason for the increased permeability is still unknown.

Conclusions

The literature on filiform corrosion has been reviewed and new data on filiform velocity have been presented. Although several elements of the corrosion mechanism remain unresolved, and a quantitative mathematical model has not yet been presented, the present qualitative model is consistent with all of the major characteristics of filiform corrosion listed in Table 2.

The following conclusions have been based on the results of experiments and calculations, and apply specifically to the mechanism of filiform corrosion on iron.

1. Filiform corrosion is a mobile, oxygen-driven corrosion cell with primary characteristics which are independent of the coating.

2. Oxygen and water diffuse from the break in the coating to the head through the porous tail.

3. Separation of anodic and cathodic reaction sites is required.

4. Filiform tracks grow away from the cathodic reaction site, *i.e.*, oxygen sources, toward the anode, but the mechanism which determines the speed is not yet understood.

5. All of the primary characteristics of filiform corrosion are compatible with the porous-tail model.

Acknowledgments

This work was supported by Air Force Office of Scientific Research Contract No. F49620-76-C-0029 and Office of Naval Research Contract Nos. N00014-79-C-0021 and N00014-82-C-0052. The authors are grateful to Michael LaScala, who performed the filiform corrosion experiments, and to E. Koehler, who provided data and helpful discussion of this work.

References

1. Ackerman, A., Kolloid-Z, Vol. 28, p. 270 (1921).
2. Ackerman, A., Kolloid-Z, Vol. 59, p. 49 (1932).
3. Sharman, C. F., Nature, Vol. 153, p. 621 (1944).
4. Van Loo, M., Laiderman, D. D., and Bruhn, R. R., Corrosion, Vol. 9, pp. 277-283 (1953).
5. Hargreaves, F., J. Iron Steel Inst., pp. 47-49 May (1952).
6. Hoch, G. M., Localized Corrosion, Williamsburg, Virginia, 1971, R. S. Staehle, B. F. Brown, J. Kruger, and A. Agrawal, eds., p. 134, NACE, Houston, Texas (1974).
7. Slabaugh, W. H., Dejager, W., Hoover, S. E., and Hutchinson, L. L., J. Paint Technol., Vol. 44, No. 566, p. 76 (1972).
8. Kaesche, H., Werks. Korros., Vol. 11, p. 668 (1959).
9. Preston, R. St. J. and Sanyal, B., J. Appl. Chem., Vol. 6, pp. 26-44 (1956).
10. van der Berg, W., van Laar, J. A. W., and Suurmond, J., Proc. Int. Conf. Org. Coat. Sci. Technol., Vol. 3, pp. 385-406 (1977).
11. Holler, A. C., Off. Dig., Fed. Soc. Paint Technol., Vol. 35, pp. 1163-1175 (1963).
12. Slabaugh, W. H. and Chan, E. J., J. Paint Technol., Vol. 38, pp. 417-420 (1966).
13. Pourbaix, M., Atlas of Electrochemical Equilibria in Aqueous Solutions, NACE, Houston, Texas (1974).
14. Slabaugh, W. H. and Grotheer, M., Ind. Eng. Chem., Vol. 46, pp. 1014-1016 (1954).
15. Latimer, W. M., The Oxidation States of the Elements and Their Potentials in Aqueous Solutions, Prentice-Hall, Inc., Englewood Cliffs, New Jersey (1952).
16. Baes, C. F., Jr. and Mesmer, R. E., The Hydrolysis of Cations, John Wiley and Sons, New York, New York (1976).
17. Beck, T. R. and Chan, S. G., Corrosion and Corrosion Protection, R. P. Frankenthal and F. Mansfeld, eds., p. 131, The Electrochemical Society, Pennington, New Jersey (1981).
18. James, W. J., Advances in Corrosion Science and Technology, M. G. Fontana and R. W. Staehle, eds., Vol. 4, p. 85, Plenum Press, New York (1974).
19. Uhlig, H. H. and Krutenat, R., J. Electrochem. Soc., Vol. 111, p. 1303 (1964).
20. Polymer Handbook, 2nd ed., J. Brandrup and E. H. Immergut, eds., John Wiley and Sons, New York (1975).
21. Koehler, E. L., Corrosion, Vol. 33, No. 6, p. 209 (1977).
22. Koehler, E. L., private communication, Aug. 30, 1978.
23. Ruggeri, R. T. and Beck, T. R., Final Report, October 30, 1981, Naval Ocean Research and Development Activity, Contract No. N00014-79-C-0021.
24. Kennedy, G. H., Ph.D. Dissertation, Oregon State University, Corvallis, Oregon, 1966.
25. Chan, E. J., M.S. Thesis, Oregon State University, Corvallis, Oregon, 1963.
26. Linke, W. F., Solubilities, 4th ed., American Chemical Society, Washington, D.C. (1965).
27. Kangro, W. and Groeneveld, A., Z. Phys. Chem. Neue Folge, Bd., Vol. 32, pp. 110-126 (1962).
28. Fricke, R., Z. Electrochem., Vol. 33, No. 10, pp. 441-455 (1927).
29. Schofield, M. J., Scantlebury, J. D., Wood, G. C., and Johnson, J. B., Proc. 8th Int. Congr. Met. Corros., Mainz, Fed. Rep. Ger., Vol. 2, pp. 1047-54 (1981).
30. Slabaugh, W. H. and Kennedy, G., Off. Dig., Fed. Soc. Paint Technol., Vol. 34, p. 1139 (1962).
31. Dannenberg, H., J. Appl. Polym. Sci., JAPNA, Vol. 5, p. 125 (1961).
32. Singhania, G. K. and Sanyal, B., Labdev J. Sci. Technol., Vol. 9A, Nos. 3-4, p. 169 (1971).

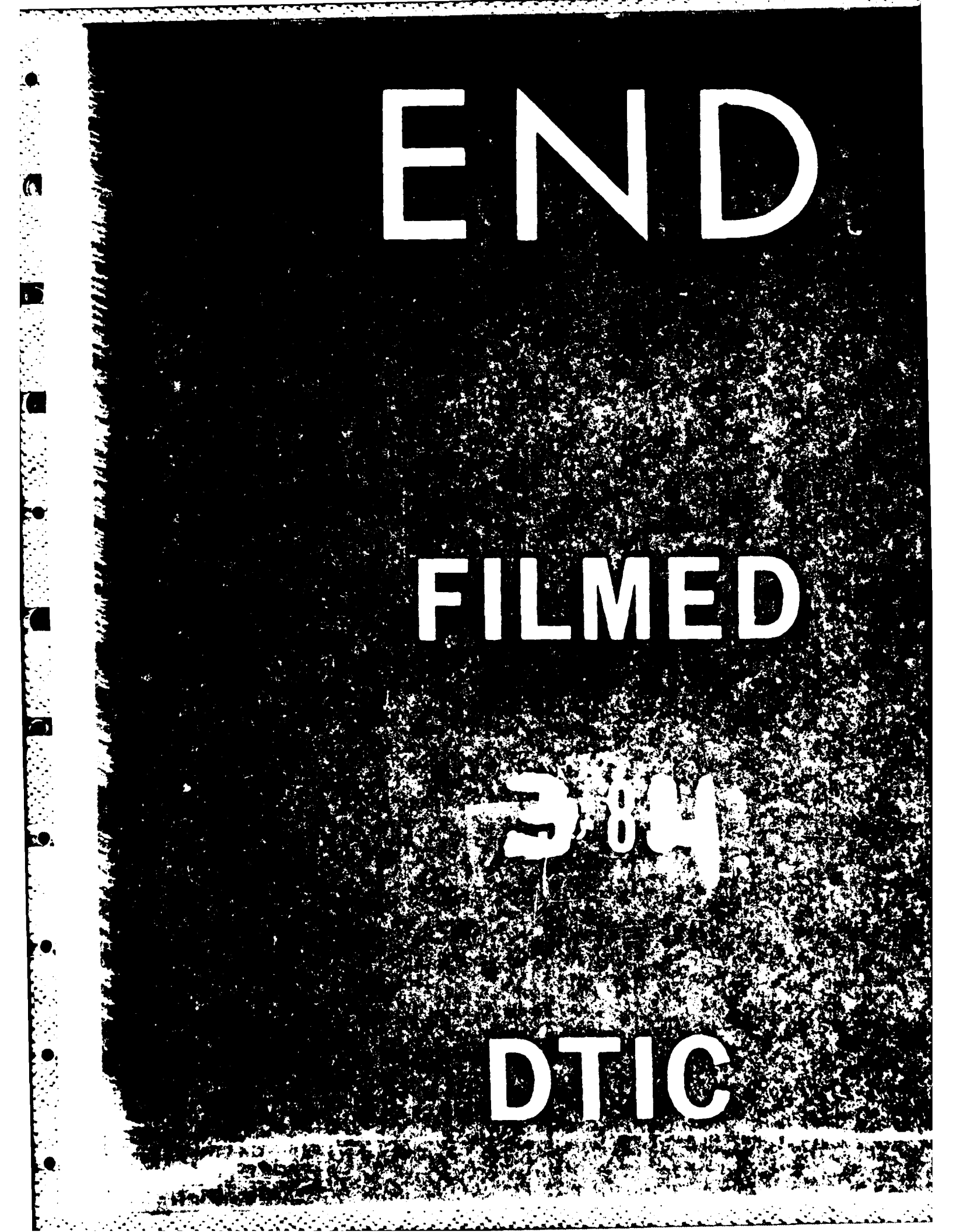
END
FILMED
DTIC